Fall 11-15-2017

Hydrogeochemical Investigation of Recharge Pathways to Intermediate and Regional Groundwater in Cañon de Valle and Technical Area 16, Los Alamos National Laboratory

Brendan W. Brady
University of New Mexico

Brendan Williams Brady

Candidate

Civil Engineering

Department

This thesis is approved, and it is acceptable in quality and form for publication:

Approved by the Thesis Committee:

Kerry Howe, Chairperson

Jose Cerrato Corrales

Brent D. Newman

HYDROGEOCHEMICAL INVESTIGATION OF RECHARGE PATHWAYS TO INTERMEDIATE AND REGIONAL GROUNDWATER IN CAÑON DE VALLE AND TECHNICAL AREA 16, LOS ALAMOS NATIONAL LABORATORY

LA-UR-17-30454

by

BRENDAN WILLIAMS BRADY

BACHELOR OF ARTS, BOWDOIN COLLEGE 1993

BACHELOR OF SCIENCE, UNIVERSITY OF NEW MEXICO, 2013

THESIS

Submitted in Partial Fulfillment of the
Requirements for the Degree of

Master of Science

Master of Science in Civil Engineering

The University of New Mexico
Albuquerque, New Mexico

December, 2017

DEDICATION

This work is dedicated to the memory of William Brady, who never looked back.

Adapt to the world around you. Always learn something new, and learn to accept what the next day brings. Live without bitterness or regret. Set your own self free. And treat the people you keep around like you know they are everything, since they may not be around forever.

Though we never met, I'm inspired by you always. Thanks for everything.

Brendan

ACKNOWLEDGEMENTS

I express my gratitude to Kerry Howe and Jose Cerrato Corrales, for their confidence in this thesis project, their commitment to learning, and the example they set as professionals, engineers, and fine people.

I want to sincerely thank Brent Newman, Tim Goering, and so many others at Los Alamos National Laboratory, for the mentorship and guidance I have received while working there. I truly appreciate the inclusiveness of the Lab community, as well as the opportunity to take part in this work and learn from the experience. I hope to have contributed something meaningful to my group and my organization.

I also wish to thank many of the fine young students and professors at the University of New Mexico, both in Civil Engineering and Earth and Planetary Science, for sharing their time, expertise, thoughtfulness, and friendship over these years.

I have many friends to thank for believing in me, and I thank my family for the patience, faith and love required for all of this. It means everything to me. Thank you, Jasmine and Vincent. Most of all, thank you always Heather, for everything sweet in this life. You are the stars in my sky.

HYDROGEOCHEMICAL INVESTIGATION OF RECHARGE PATHWAYS TO INTERMEDIATE AND REGIONAL GROUNDWATER IN CAÑON DE VALLE AND TECHNICAL AREA 16, LOS ALAMOS NATIONAL LABORATORY

LA-UR-17-30454

BRENDAN WILLIAMS BRADY

BACHELOR OF ARTS, BOWDOIN COLLEGE 1993

BACHELOR OF SCIENCE, UNIVERSITY OF NEW MEXICO, 2013

MASTER OF SCIENCE IN CIVIL ENGINEERING

ABSTRACT

In aquifers consisting of fractured or porous igneous rocks, as well as conglomerate and sandstone products of volcanic formations, silicate minerals actively dissolve and precipitate (Eby, 2004; Eriksson, 1985; Drever, 1982). Dissolution of hydrated volcanic glass is also known to influence the character of groundwater to which it is exposed (White et al., 1980). Hydrochemical evolution, within saturated zones of volcanic formations, is modeled here as a means to resolve the sources feeding a perched groundwater zone. By observation of solute mass balances in groundwater, together with rock chemistry, this study characterizes the chemical weathering processes active along recharge pathways in a mountain front system. Inverse mass balance modeling, which accounts for mass fluxes between solid phases and solution, is used to contrive sets of quantitative reactions that explain chemical variability of water between sampling points. Model results are used, together with chloride mass balance estimation, to evaluate subsurface mixing scenarios generated by further modeling. Final model simulations estimate contributions of mountain block and local recharge to various contaminated

zones.

High explosive compounds, dispersed in a zone of perched intermediate groundwater at Los Alamos National Laboratory, are contaminants of potential concern. Remediation strategies that may be put in place are largely dependent on the complex subsurface hydrology of Technical Area-16, adjacent to a wet canyon on the western margin of the Pajarito plateau. Distribution of recharge water as it crosses the Pajarito fault zone, to the regional aquifer directly, to lateral subsurface pathways, and to springs and alluvium, is not well understood. A network of monitoring wells in various saturated zones has informed extensive sets of water chemistry data. Geological observations and whole rock geochemical data, often gathered during the development of these wells, are used to constrain and evaluate models.

Validated mixing model simulations indicate that mountain block recharge sources dominate both regional and intermediate water in most sample locations. The upper intermediate zone of groundwater inhibits mixing and appears to act as a barrier between local recharge and the regional aquifer, though not uniformly.

Table of Contents

1.0 Introduction

1.1 Research objective

The objective of this research is to estimate relative contributions, by three principal avenues of mountain front recharge (MFR), to a contaminated zone of intermediate groundwater below Cañon de Valle and Technical Area 16, shown in Figure 1. The present distribution of contaminant reveals little about subsurface features or flow, aside from some degree of connectivity between a variably-saturated surface zone, poorly-defined perched intermediate groundwater zones, and the regional aquifer. Vertical distribution of recharge to intermediate groundwater is consequential, as it affects the mobility of dissolved contaminants which originated at the surface. If the bulk of intermediate water enters the zone laterally along deeper flowpaths, much of it could potentially move below the focus of contamination, or lower concentrations by dilution; however, some water appears to percolate downward, causing further movement or dispersion of contaminants. The immediate sources of groundwater to the upper intermediate zone are investigated here, using the background hydrochemistry of low temperature water-rock interactions in silicate-dominated rock formations.

Future remediation and risk assessment work related to high explosive contamination at TA-16 will rely on an understanding of hydraulic and hydrogeologic influences on the upper groundwater zone. This work aims to contribute to that understanding, and inform further modeling, which may include more extensive and varied types of data to better constrain results.

The sources of water to the perched intermediate zone are generalized here as: vertically-infiltrating spring and canyon alluvial water; laterally migrating groundwater stored in

porous, glassy rocks formed by pyroclastic flows and their erosion; and water exposed to fractured and sedimentary dacitic rock formations. These characterizations are tested with a series of inverse geochemical models within each formation, designed to indicate the dominant water-rock interactions. Inverse models are set up and evaluated in the context of data from published literature and Laboratory documents.

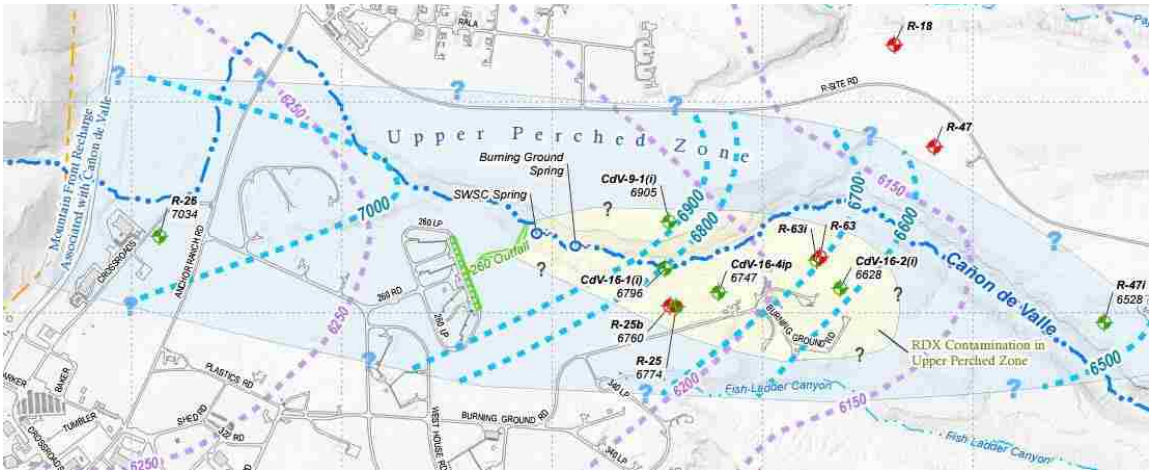

Figure 1. TA-16 and Cañon de Valle, with Pajarito fault zone on left. (LANL EP-2011-0227)

Consistency is sought across results for flowpath simulations in the same rock formation, as well as with Saturation Indices and mineralogical data. Preferred results are used to assess a series of mixing models, which integrate inverse mass balance solutions with mixing of two or more waters. Results of these models, and associated uncertainty, are addressed in the Discussion section. The mixing analysis relating to the upper intermediate water is extended to a secondary inquiry, into a similar source attribution in a lower lens of perched groundwater. With limited data from few sampling points, results pertaining to lower zones are considered highly uncertain, and potentially difficult to evaluate with confidence. However, a comparison can be made to an external calculation based on tritium levels in upper, lower and regional aquifers.

Though the mountain front zone and Pajarito plateau are geologically complex, and distribution of vadose and intermediate zone flow is understood to be heterogeneous, several generalizations are made for the sake of model processing. The design of this project broadly assumes water chemistry at sampling points to be indicative of conditions across wider areas. Aggregated water compositions are used to address analytical uncertainty, as well as temporal variability in the data that may result from seasonal or storm conditions. While transient reducing conditions may exist within these rocks sporadically, oxidizing conditions are assumed to be dominant, and dissolved oxygen available to react. Steady-state flow and chemistry are assumed, across a two-dimensional cross section as shown in Figure 2. This research takes a macroscopic approach by employing abundant data, mostly collected for regulatory purposes, to the problem of relative connectivity between aquifer compartments.

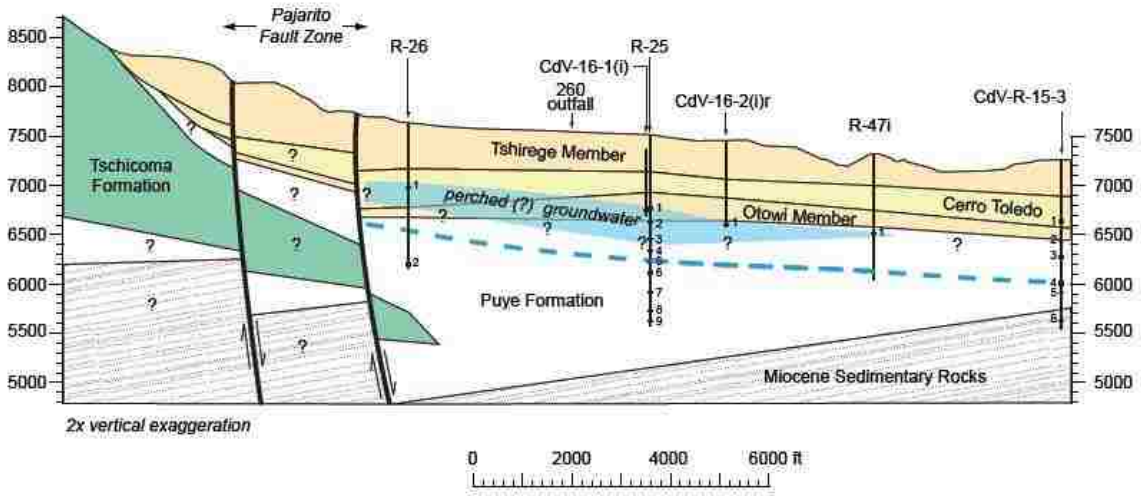

Figure 2. Approximate cross-section of mountain front and Cañon de Valle geology. (David Broxton)

1.2 Background

1.2.1 High explosive contamination

Wastewater containing high explosive (HE) compounds was generated at TA-16 over a period of decades, beginning in the 1950s; it was discharged from the 260 Outfall to shallow settling ponds, which then drained into Cañon de Valle. For at least some of the time, outfall discharge is thought to have matched or exceeded natural groundwater recharge in the Cañon de Valle watershed. By far the predominant form of HE was RDX (hexahydro-1,3,5-trinitro-1,3,5-triazine), which has relatively high solubility and a low value for K_{ow} (partition coefficient). Consequently, dissolved RDX is highly mobile in groundwater. It contaminates perched intermediate groundwater zones and the regional aquifer below TA-16, in addition to surface sediments in the area of the HE outfall, springs that emerge in Cañon de Valle, and the shallow alluvial aquifer in the perennial flowing reach of Cañon de Valle.

Downward movement of RDX to the regional aquifer is possible via saturated pathways from contaminated near-surface areas where hydraulic head is sufficient. In the past, the settling pond and discharge channel from the 260 Outfall acted as a conduit to the subsurface (LANL 2003, 77965). Within the Tshirege Member are surge beds, highly discontinuous structures with greater porosity than surrounding rock. Lateral movement of water through surge beds and cooling joints appears to have enhanced RDX distribution in the vadose zone (Birdsell et al., 2005). The overall amount of groundwater added to the perched intermediate zone as a result of focused wastewater discharge over several decades, versus natural recharge from the losing reach of Cañon de Valle, is not known. The settling pond has been dry at least since 1996. In recent years, work such as

soil removal, grouting of surge beds, and the placement of bentonite caps has restricted infiltration and lateral movement of shallow groundwater in the outfall area to some degree (LANL EP-2011-0227). However, the success of these measures is uncertain. At the present time, surface saturation is limited to the shallow alluvial aquifer in Cañon de Valle, which is fed by Burning Ground Spring and SWSC Spring. Downward flow through the fractured vadose zone to perched groundwater zones is a matter of concern, as several tens to many hundreds of kilograms of RDX are dispersed both in the alluvial and large areas of intermediate groundwater zones, at concentrations ranging between 0 and 300 μg/L (see RDX Inventory, appendix A). Such a mass of toxic contaminant poses a threat to the regional drinking water resource. Though the recharge rate downward, through intermediate zones to the regional aquifer, is unknown, in recent years RDX has been detected in three regional wells with some concentrations gradually increasing. Gradient in the regional aquifer, generally from west to east, is driven by topography and mountain precipitation.

To some degree, recharge that feeds the regional aquifer appears to interact with the contaminated groundwater. The central question addressed by this study, the attribution of recharge water to immediate source, has significant implications for RDX remediation. If direct mountain block or focused fault zone recharge far exceeds intermediate zone infiltration, contaminated groundwater may be relatively static. Continuous dilution as water enters the regional aquifer, possibly from higher velocity flow near the water table surface, could keep regional groundwater RDX at acceptably low levels. If lateral flow from the fault zone, together with surface infiltration in Cañon de Valle, contributes to intermediate groundwater at a high rate, an acceleration of RDX input to the regional

aquifer could occur.

Infiltration from the TA-16 section of Cañon de Valle is thought to be minor. However, even a small input may influence RDX mobility greatly, as it represents a downward push on the plume. Unlike laterally-migrating subsurface recharge, which would be expected to further dilute RDX in solution, recharge that enters through surface or near-surface areas at TA-16 could potentially dissolve additional HE solids. RDX occurs in discharge from both Burning Ground Spring and SWSC Spring, suggesting that it is stored and mobilized from somewhere within the vadose zone.

1.2.2 Site geology

Regional and perched intermediate groundwater are both found in the Puye Formation, an alluvial fan deposit of between 3 and 1.61 million years in age (LANL EP-2016-0113). The Puye Formation is composed of dacitic cobble, gravel, sand and silt weathered from the older Tschicoma Formation. In this area it is represented by a fanglomerate facies, characterized as highly stratified, poorly sorted and poorly cemented, with a sandy to silty matrix (LANL ER2001-0697). Clay and possible soil horizons appear near the top of the formation. Groundwater flow in the Puye is expected to be heterogeneous, and anisotropy suggested by interbedded silt and clay layers would indicate that lateral flow far exceeds vertical flow (LANL ER 2005-0679).

The Tschicoma Formation itself, the source material of the Puye, is composed of variously dacite to low-silica rhyolite that erupted as lava domes in the Sierra de los Valles about 3 million years ago (Broxton et al., 2007). A dense, massive lithology in the lava flow interiors transmits limited mountain block water through fractures, while a

brecciated lithology at the margins of the formation is likely to hold and interact with a greater amount of groundwater. Overall, however, the Tschicoma Formation is considered a poor aquifer. (LANL EP-2011-0227).

Overlying the Puye Formation is the Otowi Member of the Bandelier Tuff, formed by pyroclastic ash flows 1.61 million years ago; it is a relatively uniform, nonwelded, vitric tuff. Welding refers to the flattening of pumice fragments and adhesion of ash, and vitric indicates that rock has not experienced vapor-phase alteration, where clay mineral deposition in open pores occurs during post-eruption degassing. Much glassy silica is preserved in the Otowi Member, in a porous matrix. At the base of the Otowi is the Guaje pumice bed, a highly porous and potentially important flow pathway between 5 and 15 feet thick. However, because the Guaje pumice bed lies beneath a rock formation of lesser porosity, it may act as a capillary barrier, restricting downward percolation but pushing lateral groundwater movement (LANL EP-2016-0113).

The voluminous upper zone of perched intermediate groundwater at TA-16 resides in both the Otowi and Puye, though closer to the mountains perched water may be stratigraphically higher. Screen 1 of well R-26 samples perched intermediate water in the Cerro Toledo Formation, overlying the Otowi Member (KA Project No. 37151).

The Cerro Toledo Formation is a relatively porous sedimentary formation of sandstone and tephra with ash, pumice and clasts of lava derived from nearby volcanic dome structures. An unconformity occurs between the Otowi and the Cerro Toledo, and in the area of Cañon de Valle the Cerro Toledo fills a paleochannel eroded into the Otowi tuff (LANL ER 2005-0679). At well R-26, the section of Cerro Toledo is over 300 ft. thick.

Overlying the Cerro Toledo, the Tshirege Member is the upper sequence of the Bandelier Tuff; it forms the bulk of mesa structures seen at the surface as well as most of the thick unsaturated zone. Much of this unit is massively welded and relatively impermeable; within it, flow is understood to occur largely through tectonic fractures and cooling joints (Birdsell et al., 2005; Newman et al. 2007). In Figure 3, the Tshirege Member is divided by individual cooling unit. Unaltered glass occurs mainly in the base, in unit Qbt 1g, and near the surface, in Qbt 4 (Broxton, 2007). Burning Ground Spring and SWSC Spring, which feed the Cañon de Valle alluvial aquifer, emerge from Qbt 3t, which is also exposed in upper Cañon de Valle. Martin Spring emerges from Qbt 4, the uppermost cooling unit of Bandelier Tuff, which has a distinctly different chemical profile (LANL ER2001-0697).

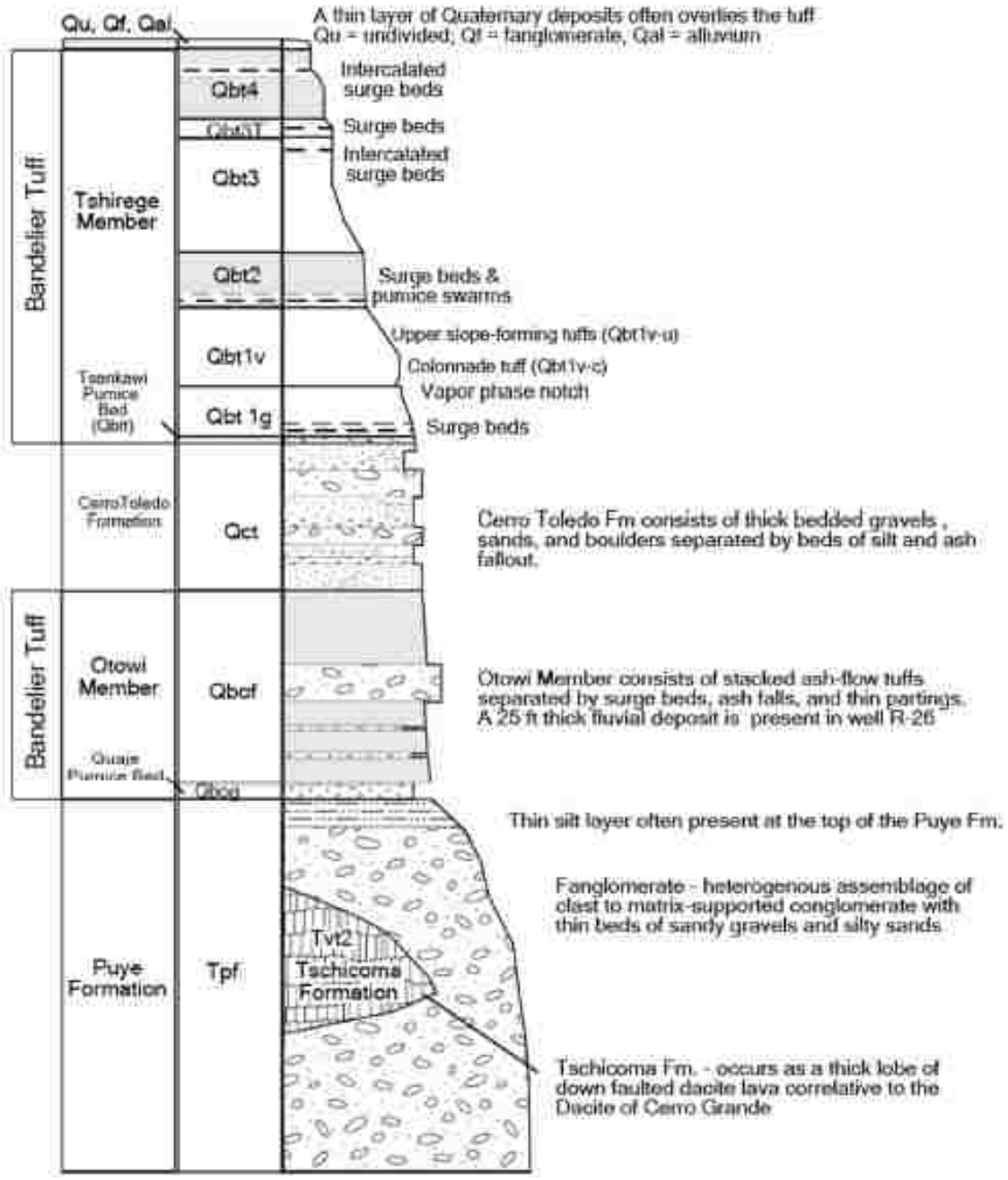

Figure 3: Stratigraphy of the geologic units at TA-16 (LANL EP-2016-0113)

1.3 Mountain front hydrology

1.3.1 Conceptual model of groundwater recharge in Cañon de Valle

A conceptual model of intermediate recharge is represented in Figure 4. Sources to the perched zones include: the channel in Cañon de Valle, fed by intermediate spring water that saturates a limited shallow alluvial zone; lateral seeps across the fault and into the tuff vadose zone, Cerro Toledo Formation and underlying Otowi Member; and water that reaches deeper through the fault zone, accessing beds of cobble and gravel in the upper Puye Formation.

Intermediate springs at TA-16 discharge from saturated pathways connected to surface water and shallow groundwater in mountain block fractures. A parting between two upper cooling units of welded Bandelier Tuff carries water from the fault zone to the springs (LANL EP-2016-0113). These feed a perennial section of stream, and associated shallow alluvial aquifer in lower Cañon de Valle.

Perennial flow in the high section of upper Cañon de Valle yields to ephemeral flow in the lower part, typically diminishing and terminating at various points in or above the fault zone. Following the Las Conchas fire, a major flooding event in 2013 deposited massive amounts of fine material in the lowest reach of upper Cañon de Valle, and scoured some bedrock in the fault zone. Though some alluvial material remains, there is no longer a continuous interflow zone. Focused recharge is now fed directly by channel flow. Across the fault zone, where surface runoff was once infrequent, it is now highly improbable and would be limited to rare storm events.

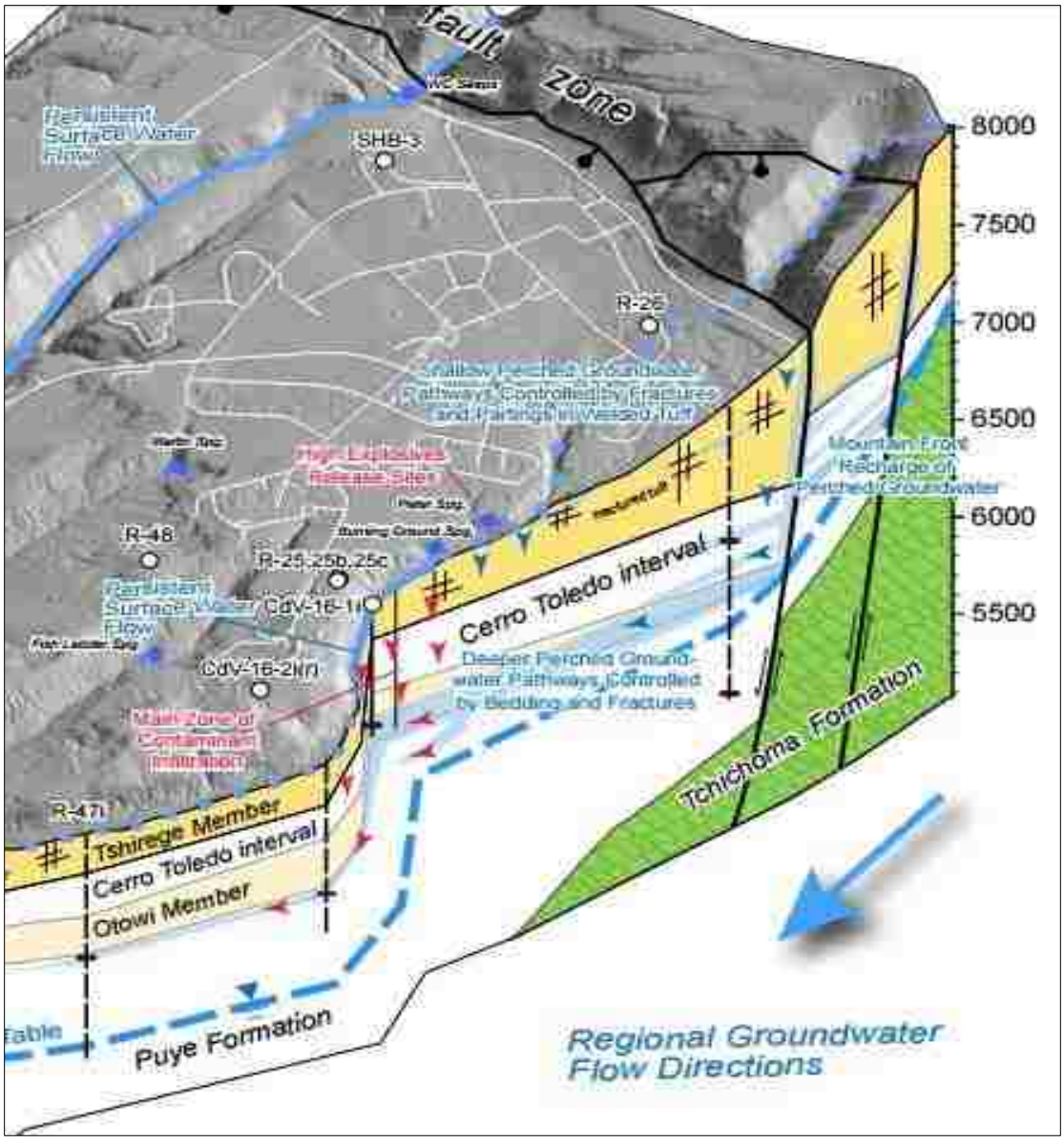

Figure 4: Conceptual model of recharge at TA-16 (LANL EP-2011-0227).

Focused infiltration along the fault may move downward relatively quickly, along damage zones in the rock that run parallel to fault cores (Bense et al., 2013). Mountain block groundwater that would travel laterally across the fault may be restricted to some degree. Fault cores in consolidated or crystalline rocks are expected to have lower permeability; however, both the Cerro Toledo and Puye are poorly sorted and poorly consolidated sedimentary formations, so hydraulic head in the fault zone is likely to help

charge these zones with groundwater moving laterally eastward. Regional groundwater, residing in pore space in the Puye Formation and underlying Santa Fe Group rocks, is presumably connected to deep bedrock fractures, and fed by infiltration of higher elevation precipitation in the Sierra de los Valles. Infiltration through the fault zone is probably distributed between the regional water table, porous rocks and fractures in the intermediate zone, and fractures and partings between cooling units of the tuff vadose zone.

There is the possibility that upper intermediate groundwater in the Puye Formation is influenced by deep mountain block recharge. Mixing probably occurs between fault-associated infiltration and water from mountain block fractures, with some migrating across the fault zone to stratigraphically higher rocks in the downthrown Plateau strata. Direct mountain front infiltration may contribute somewhat to regional groundwater, though in proportions that are not well understood. It is expected to mix with water in mountain block fractures and penetrate the fault, contributing to perched intermediate groundwater in the vicinity of well R-26.

The cutaway section of Figure 4 would show the north side of Cañon de Valle and well 9-1(i), where unconfined water in the upper intermediate zone appears to have a higher phreatic surface, as seen in piezometers (Figure 5). Screen 1 at CdV-9-1(i) is situated in a seemingly separate lens, possibly of confined water. The water level in this well responds to snowmelt recharge events in the upper canyon. Well CdV-16-1(i) shows some response as well, as do Screens 1 and 2 in well R-25, indicating connection between the fault zone and upper perched groundwater.

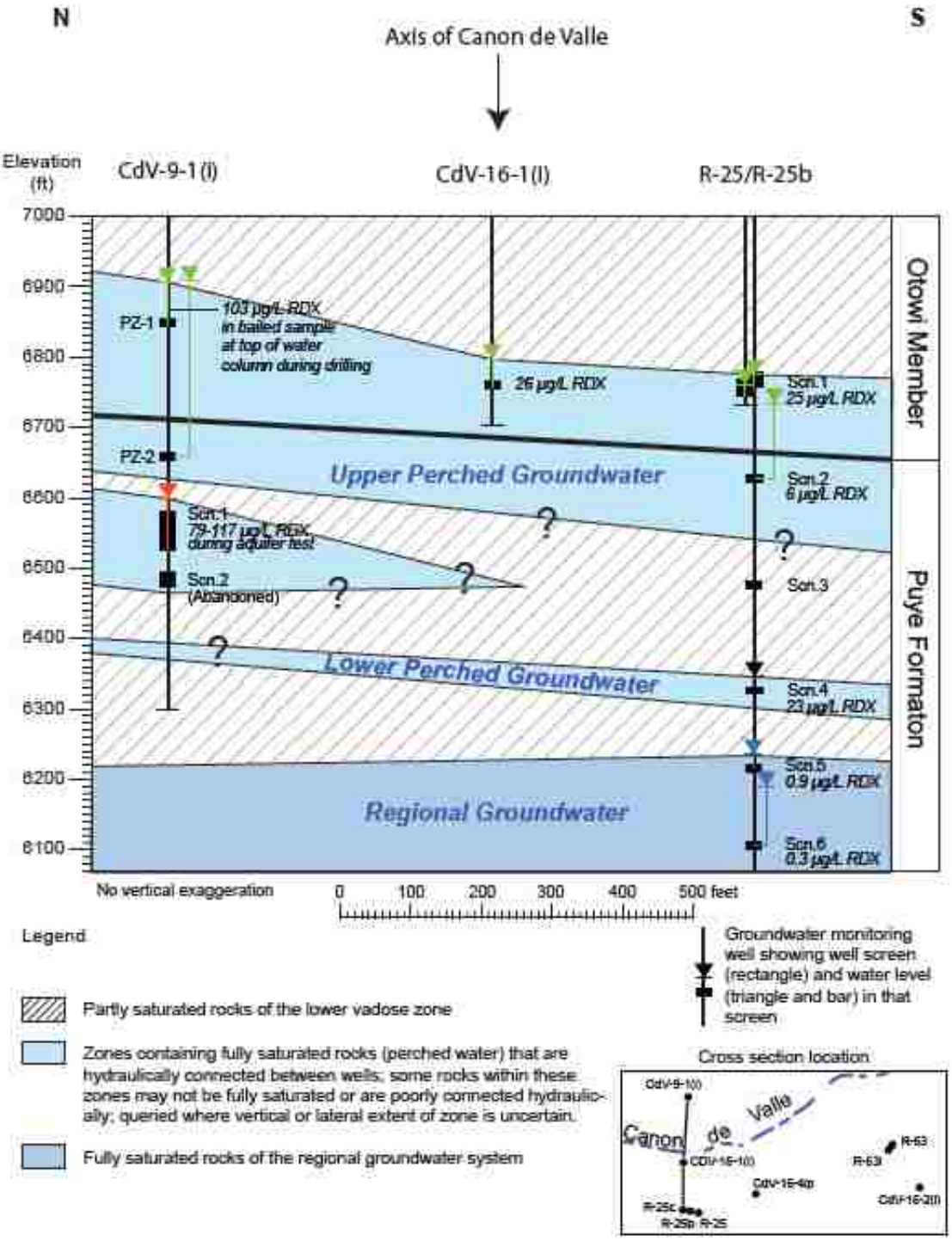

Figure xx North-south geologic cross section for the lower part of the vadose zone showing geologic contacts and groundwater occurrences in wells CdV-9-1(i), CdV-16-1(i), R-25b, and R-25.

Figure 5: TA-16 X-sections for CdV-9-1i pump test (Broxton)

1.2.2 Theory and classification of mountain front recharge

The conceptual model of groundwater flow developed by József Tóth indicates that recharge to regional aquifers originates in highland areas, while intermediate and local systems are more likely controlled by basin topography (Freeze & Cherry, 1979). In idealized, uniformly permeable sediment, nested flow pathways articulate this concept; however, a realistically accurate subsurface model is nearly impossible to represent, due in part to heterogeneity and hydraulic conductivity variability and uncertainties. Nonetheless, diverse hydrologic studies support the idea that high-altitude precipitation is the primary component in regional groundwater systems (Manning, 2010; Ajami, 2011). In semi-arid basins, snowmelt can be the most important recharge mechanism to deep groundwater (Wahi et al., 2008). The term mountain block recharge (MBR) is sometimes used to describe the input of mountain precipitation to permeable bedrock, analogous to the regional flow path in the Tóth model. In the Sierra de los Valles, MBR could be connected to an extension of the regional aquifer, in some form, reaching across the fault zone. Intermediate groundwater, perched over aquitards in sedimentary formations or impermeable volcanic strata as described above, may take other recharge pathways from mountain bedrock. These would be lateral pathways through anisotropic media, or downward along fractures or other discontinuities.

Wilson and Guan (2004) note that mountain system recharge has been typically understood from a basin-centered perspective, where input from above the mountain front is limited to stream runoff. Subsurface characteristics of the mountain block itself are often complex, poorly understood, and therefore neglected (Tromp-van Meerveld et al., 2006; Aishlin & McNamara, 2011). Mass-balance approaches may attempt to estimate

deep recharge by quantifying all other outputs and subtracting them from precipitation, though both mountain precipitation and evapotranspiration are difficult to estimate. A hydrological model focused on partitioning of mountain water between deep bedrock and shallow fracture infiltration, channel runoff, soil layer interflow, and evapotranspiration - a mountain-centered model that would rely on technologically advanced methods of data collection to limit uncertainty (Wilson and Guan, 2004), would be an improvement. The salient feature of such a model would be the ability to account for storage in the subsurface above the mountain front zone.

Mountain Front Recharge (MFR), in the terminology used by Wilson and Guan (2004) and others, includes all the water leaving a mountain block and recharging a valley aquifer at the mountain front. In this study, the mountain front is considered as a plane aligned parallel with the Pajarito fault zone. The four components of MFR are as follows: focused surface recharge (FS), consisting of surface streams directly feeding the aquifer at the mountain front; diffuse surface recharge (DS), consisting of precipitation entering the subsurface through thin soils at the mountain front; focused recharge (FR), which includes both water entering the subsurface through streambed sediment and water moving from bedrock fractures in the mountain block directly to the valley aquifer; and finally, diffuse recharge (DR) is unfocused flow from the mountain block to valley sediments. The relationship between these components can be mathematically represented as follows (Wilson and Guan, 2004):

$$MFR = FS + DS + FR + DR$$

The latter part of the description above for (FR), involving movement of water held

within mountain block fractures to the valley aquifer, is usually referred to as mountain block recharge (MBR); however, the entire focused recharge definition captures the two aspects of local recharge, as applicable to this study. Water entering the subsurface through streambed sediment (FR part a) is alluvial aquifer water in Cañon de Valle, and water moving from bedrock fractures in the mountain block directly to the valley aquifer (FR part b) is water in the shallow intermediate zone that emerges from Cañon de Valle springs.

In upper Cañon de Valle, the length of the flowing channel is variable by season; typically, it is longest when summer monsoon patterns bring rain, and during spring snowmelt. Though extreme flood events could cross the fault zone as channel flow, virtually all rain and snowmelt does not; rather, it disappears underground in the mountain front zone, with the termination point dependent, apparently, on the magnitude of flow. Most of this water is probably drained to the subsurface directly as focused surface recharge (FS), via the fault zone. Some of this appears to travel along bedding planes of welded and devitrified tuff in the Tshirege Member, rather than accessing the deeper subsurface. Water present in the fault zone may also charge porous rocks and feed preferential flow paths in the Cerro Toledo Formation and the Guaje pumice bed (LANL ER 2005-0679).

The absence of an alluvial interflow zone over the fault, the condition described previously as resulting from flood scouring, may have an effect on the subsurface distribution of recharge, possibly limiting saturation in the shallow intermediate zone that feeds SWSC and Burning Ground Springs. However, some MFR, possibly a combination

of precipitation as diffuse surface recharge (DS), and focused fault-associated water, perches above the tuff cooling unit Qbt3. In either case, this component emerges at the springs in the area above contaminated perched intermediate groundwater; in this study, it is accounted for as focused recharge (FR part b). This may be enhanced by snowmelt conditions, when channel flow in upper Cañon de Valle terminates at lower points in the fault zone. During a recent drought, the lower canyon springs ceased to flow, though presumably mountain block recharge from the upper canyon continued to feed the regional aquifer.

Because of the small area of mountain front considered here, diffuse surface recharge (DS) is normally a small amount of water, and is neglected. Due to the porous character of the Cerro Toledo interval, diffusion of surface infiltration might be expected across the fault zone, so (FS) and diffuse recharge (DR) may be considered closely related, with fault-associated infiltration augmenting (DR). However, reduced permeability of fault cores (Bense et al., 2013) may cause groundwater to back up laterally against a fault, as shown in Figure 4. In this study, diffuse recharge (DR) is thought of as groundwater penetrating fault cores into the unsaturated zone of the Tshirege, Cerro Toledo, or Otowi; this water likely occurs heterogeneously along preferential flow paths such as fractures or "ribbon-like structures" (LANL 2003, 77965; LANL ER 2005-0679), moving into the shallow perched intermediate zone to the east. Neglecting diffuse surface recharge (DS), the three types of recharge that constitute MFR can be thought of as entering the Plateau groundwater system differently: focused surface recharge (FS) directly into the Puye Formation, entering the subsurface at or above the fault; diffuse surface recharge (DR) into the intermediate Otowi of Cerro Toledo groundwater from the fault, and focused

recharge (FR) through the fault and upper Bandelier Tuff to Cañon de Valle alluvium. Amending the formula given above for MFR, this study is based on partitioning TA-16 groundwater as follows:

MFR = recharge to Puye Fm (FS) + recharge to Otowi/Cerro Toledo Fm (DR) + recharge via Cañon de Valle alluvium and Tshirege fractures (FR)

MBR = Tschicoma/Puye Fm waters (FS) + Otowi/Cerro Toledo Fm waters (DR)

Local recharge = alluvial aquifer water (FR part a) + Tshirege Member water (FR part b)

Components are conceptualized as end-members in the mixing model analyses, and represented by characteristic water chemistry profiles. They are expected to differ according to their respective interactions with mineral and glass phases. By the definition of Wilson and Guan, MBR through permeable, deep bedrock would be the subsurface component of (FR); however, this is complicated by the mixing assumed to occur within the fault zone. Here, characteristics of Tschicoma Formation-associated regional water would be present, if at all, in focused surface recharge (FS) to the Puye Formation. Though groundwater influenced by contact with the Puye Formation above the fault may contribute to diffuse recharge (DR), water in the upper zone is expected to be more strongly influenced by contact with vitric glass in the Otowi Member and basal Guaje pumice bed. Focused recharge (FR) is expected to make a small contribution to upper intermediate groundwater, influenced less by vitric glass and more by the evaporated signature of alluvial aquifer water. Figure 6 presents generalized lithologies of rock formations at the site together with assumed flow regimes in each.

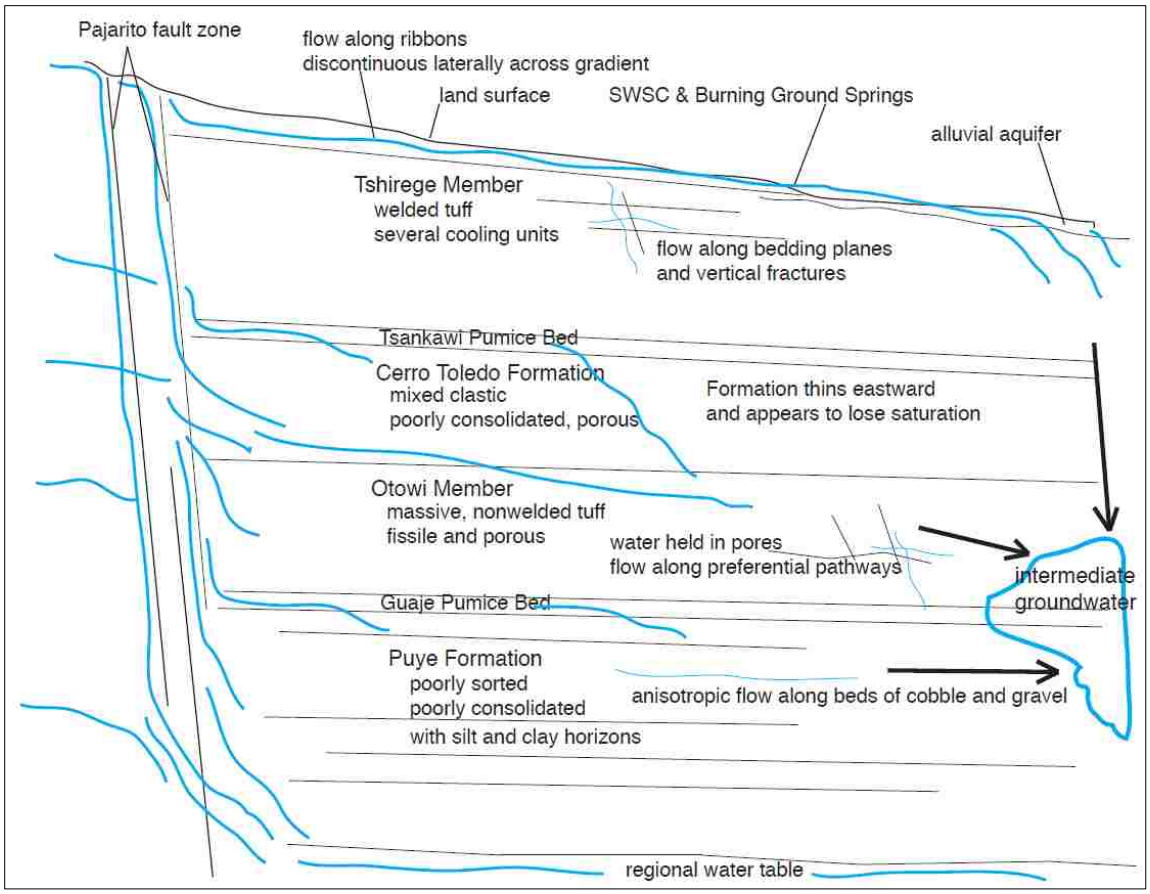

Figure 6: Schematic diagram of possible recharge pathways through TA-16 geologic formations. Intermediate groundwater connects to mountain block sources.

1.2.3 Variability in hydraulic conductivity

In the fall of 2015, conservative groundwater tracers were introduced in screen 1 of CdV 9-1(i), in the Puye Formation, and R-25b, in the Otowi Member. Point dilution tests (Drost et al., 1968) were performed to estimate the local velocity of groundwater around each screen. For each test, water in the casing, screen, and pump riser is purged and replaced with a solution of conservative tracer, which is then pumped and cascaded back to the water table. An automated device at the surface takes samples every 30 minutes, for 48 hours. Using fluorimetry for analysis, the slope of first-order decay is plotted. The slope [1/hour], times volume of solution in the flow loop, gives an estimate of volumetric

flow rate through the screen. When divided by a two-dimensional area through which the flow passes (screen length x filter pack diameter), then divided by the formation porosity, the result is an estimate of local linear flow rate, considered reliable where flow laterally across the screen far exceeds vertical flow. In the Otowi around R-25b, this result was 0.06 meters/day, consistent with matrix flow through indurated porous tuff. By contrast, the dilution test at CdV 9-1(i), situated in a lower intermediate section of Puye sediment, gave a result of 3.2 meters/day (LANL ER Group, unpublished research). The disparity between these numbers can be partly explained by heterogeneity within the Puye, but suggests that overall flowrates are greater below the level of the Bandelier Tuff, where the Puye Formation offers a pathway of lesser resistance.

Observations from the drilling of well R-26 tend to support the idea that locally within the top of the Puye Formation, water has greater mobility. Potassium bromide (KBr) was circulated with drilling fluid and monitored at the surface, with concentrations remaining stable during drilling to a depth of about 650 ft., which is about halfway through the Cerro Toledo. Below that level, KBr was diluted by water entering the borehole. The geophysical log report describes this zone as not entirely saturated, but “with a high degree of water-filled porosity” (KA Project No. 37151, 2005). When drilling penetrated the Guaje pumice bed, a switch was made to mud-rotary drilling, and a significant amount of mud was lost into the formation. Drillers reported pumping 42,000 gallons of mud into a ~6,000-gallon hole over the course of three days, and were unable to seal the hole with lost-circulation material. The bottom of the R-26 bore hole, where a now-abandoned screen was placed, is in regional groundwater at a depth of 1445 feet below the ground surface. Hydraulic conductivity was estimated, for intervals around 1,100 ft.

and 1,200 ft. depth, to be in excess of 3 gal/day/ft^2 (KA Project No. 37151, 2005).

In nearby Los Alamos Canyon, a wet canyon environment, permeability in the Otowi Member was found to be lower in the clay-filled fractures than in unaltered tuff matrix, by one to two orders of magnitude (Vaniman et al., 2005). However, Los Alamos Canyon differs in the sense that it lacks a thick section of Tshirege vadose zone; extensive weathering by surface water generates clays to a degree not observed in TA-16 wells. In well R-25, open fractures observed in borehole videos were seen transmitting water, and similar high-angle fractures were seen in CdV 16-1(i), on a Formation Micro Imager (FMI) log (LANL EP-2016-0113); also, well CdV-16-1(i) has a pressure response to snowmelt wetting events that is consistent with fracture flow dominance. Fracture flow appears to be dominant in the Otowi Member beneath Cañon de Valle; matrix flow, as described above for R-25b, is restricted by lower transmissivity.

1.2.4 Tritium and RDX as indicators of groundwater flow and age

Tritium concentrations at various sampling points give a general idea of the ages of water at different depths. In certain regional wells, groundwater with no detectable ^{3}H indicates recharge that occurred decades before the present, either before the early 1960's increase in atmospheric tritium or long enough ago for it to have decayed to very low or non-detect levels. This is the case in well R-37-2 S2, S3 and S4, which are situated in the Tschicoma Formation; these wells probably express regional flow pathways and are unaffected by modern infiltration through the fault. A similar condition exists, interestingly, in well R-26 screen 1. The groundwater that enters this screen, situated in the Cerro Toledo Formation, is tritium-dead, indicating minimal communication with

younger water infiltrating through the fault. It seems to be mostly, if not all, diffuse mountain block recharge that bypasses fault-associated mixing.

In some regional wells, a very small but detectable amount of tritium may indicate a dilute mixture of younger water in otherwise tritium-dead older water. This can be observed in wells R-47, R-47i, and R-48. The screens of these wells are in, respectively, the regional Puye Formation, the intermediate Puye, and the regional Tschicoma Formation. There has been no RDX detected, to date, in these wells.

Water introduced during drilling can be the cause of low-level detection of tritium; this is probably the case, for instance, in R-25b, in which tritium was detected in 2009 and 2010. During that time, RDX levels were sometimes above 8 μg/L, though by 2016 they had come below 3 μg/L. The borehole dilution result indicates very slow replacement of water in the screen, and the older water coming in is nearly tritium-dead.

In R-63, a regional Puye Formation well, the initial sample was a low-level tritium detection, though it was followed by nine non-detects. In the initial sample, RDX was 16 μg/L, though in the next sampling round it came down to below 2 μg/L, and has remained consistent for several years. The initial spike seems to have been introduced during drilling or pumping associated with well development, with older formation water subsequently replacing it as RDX persists somehow. There may be communication with water in the area of upper regional screens of R-25, where a strong pulse of RDX is thought to have been introduced by the borehole left open between drilling and well installation, a period of one to two years.

Well R-18, with its screen in regional groundwater to the north of R-47, has a pattern of low-level tritium detects and non-detects, not unlike R-47 and R-47i. However, this well has seen RDX increase consistently for ten years, from near zero to over 3.5 μg/L. The introduction of RDX has not been followed by a concurrent rise in any indicator of younger water addition. The reason may be that the original contaminated water was pumped from the regional aquifer before being used in the machining process; it may represent RDX that has been in solution for decades, which has in recent years arrived at the surface of the regional aquifer, and is now mixing with older formation water. It is unlikely that older mountain block-associated water would dissolve RDX in the vadose zone and then find a path to regional groundwater.

Other intermediate wells in the Puye Formation are CdV-16-4ip, which saw tritium decrease from 16 to 8 pCi/L between 2010 and 2014, and CdV-16-2ir, which has consistently had tritium between 6 and 9 pCi/L. These wells are below 800 ft in depth, and the values differ noticeably from the springs and near-surface alluvial wells, where tritium has declined from concentrations often above 100 to below 50 pCi/L, over the time of about one half-life of ^{3}H. The intermediate wells seem characteristic of older water moving along anisotropic flow pathways, with tritium suggesting some addition of young water. This could be from snowmelt events infiltrating through the fault and feeding transiently saturated recharge pathways, or water moving downward through vertical fractures in the Otowi tuff.

In the case of CdV-16-4ip, RDX has been variable since 2011 between 120 and 165 μg/L. During that time, there has not been an obvious increasing or decreasing trend. In CdV-16-2ir, which is downgradient from CdV-16-4ip, RDX has had an increasing trend for ten

years, from just above 40 to 130 μg/L. This indicates that, while some younger water may be entering into the screen, older water is the likely source of RDX. The RDX may have been originally introduced to the intermediate zone by downward pulses of water, as the tritium appears to be. However, these data, when considered together, suggest a front of laterally-migrating groundwater, with RDX concentration of 130 to 150 μg/L, moving eastward in the intermediate Puye Formation between CdV-16-4ip and CdV-16-2ir.

In the Otowi Member well CdV-16-1(i), at 624 ft depth, tritium declined consistently from above 65 to 32 pCi/L between 2005 and 2011. This is more dilute tritium than in alluvial groundwater, and more dilute than spring water as well, so it indicates mixing with at least some older, diffuse recharge (DR) water. In that well, RDX has been variable, mostly between 25 and 30 μg/L – noticeably lower than samples from the underlying Puye intermediate wells.

If a spring, with discharge determined to be of recent precipitation, were to feed a losing reach of stream, with the vadose zone fractures connected to an intermediate well, tritium could be used for a rough approximation of mixing proportion. An important assumption would be that the intermediate water is otherwise tritium-dead. If the spring discharge declines from 150 to 100 pCi/L over the same time that the well screen water declines from 15 to 10 pCi/L, there would be a dilution factor 0.1.

Considering a pathway from Burning Ground Spring into the stream channel and downward to CdV 16-1(i), with tritium in Burning Ground Spring declining from 73 to below 30 pCi/L between 2005 and 2011, and CdV-16-1(i) declining from 65 to 32 pCi/L in the same time period, the dilution factor is closer to 0.9. In 2011, Burning Ground Spring had a tritium level of 29 pCi/L, while CdV-16-4ip (Screen 1) had a tritium level of

15.6 pCi/L – the dilution factor there would be closer to 0.54. In the lens of lower intermediate groundwater, CdV-16-4ip (S2) had tritium at 3.4 pCi/L, a dilution factor of 0.12 with respect to spring water, or 0.22 with respect to the upper screen. Going by this alone, it would seem that no more than 22% of lower intermediate water comes from the upper intermediate zone.

Well R-25, with screens in the Otowi Member, upper and lower perched intermediate Puye Formation, and several depths within the regional aquifer, offers an opportunity to approximate dilution based on tritium data (Figure 7). From 2003 to 2011, ^{3}H in the upper intermediate zone declined from 50 to 28 pCi/L (in S2), and lower intermediate water declined from 37 to 12 pCi/L (in S4). The dilution factor of Screen 4 to Screen 2 started as 0.74 in 2003; by 2011 it was 0.43. In the uppermost regional screen (S5) tritium has been variable between 14 and 18 pCi/L, showing no obvious decline between 2001 and 2010. One hundred feet deeper into the regional water (in S6) tritium has been below 5 pCi/L since 2002, also with no clear decline. The steadiness of tritium in the regional screens is difficult to explain, but it suggests that some addition of younger recharge occurs in the fault zone.

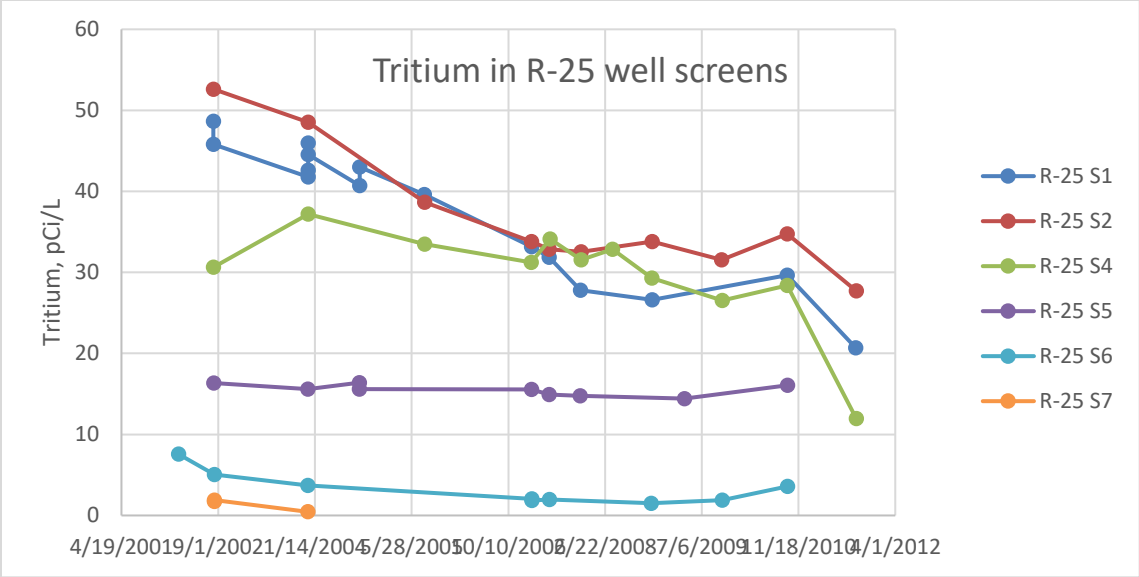

Figure 7: Tritium concentrations in screens of well R-25 over 11 years, slightly less than one half-life of tritium (www.intellusnm.com).

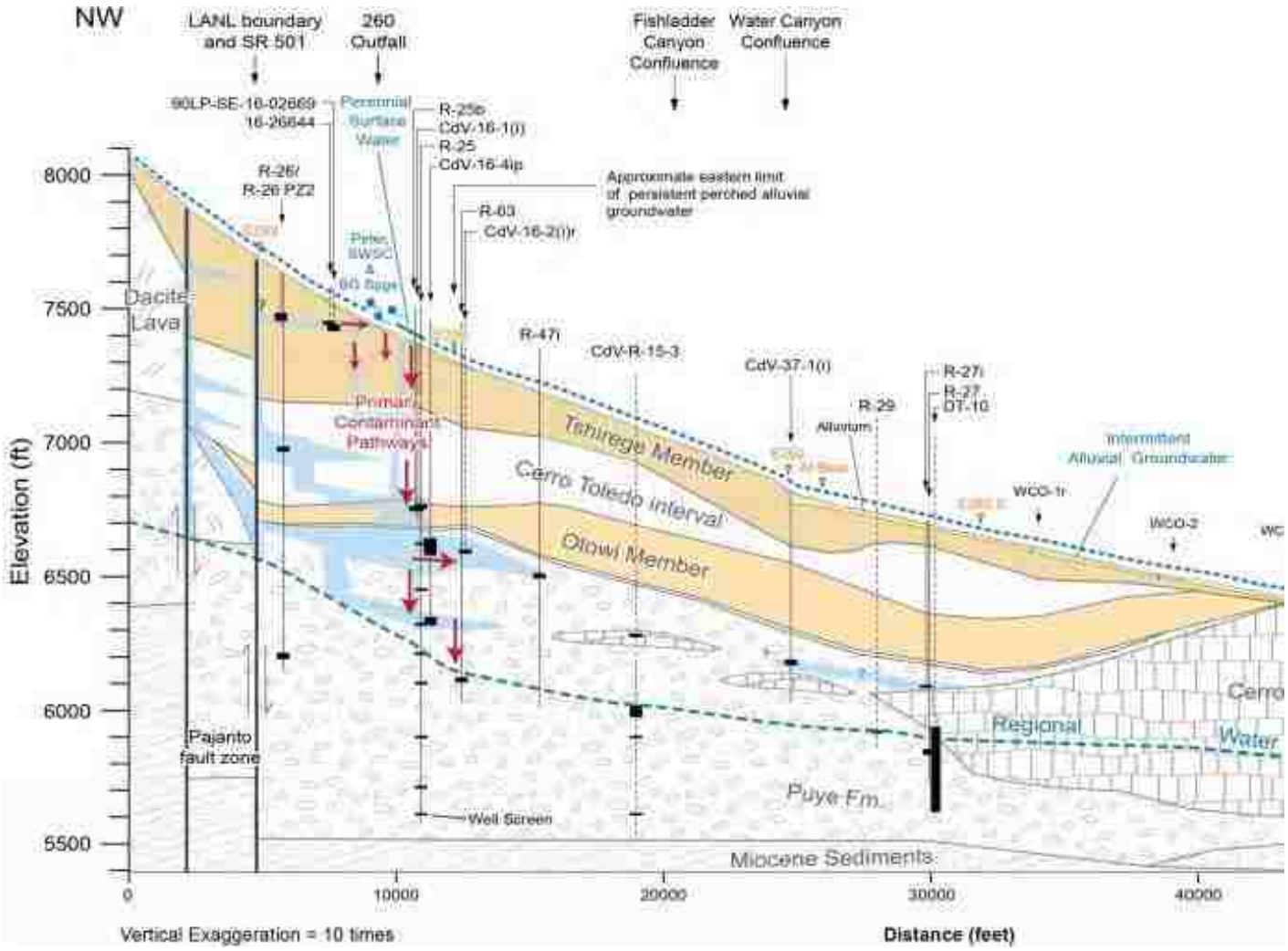

al

Figure 8. Vertically exaggerated schematic of geologic formations and perched intermediate groundwater. (LANL EP-2011-0227)

2.0 Methods

2.0 Use of geochemical modeling processes and data

Inverse mass balance modeling is used to improve understanding of the dominant geochemical reactions taking place along a groundwater flow pathway between sampling points. Reacting mineral phases are input to a process that proposes specific sets of reactions, each mediating mass transfer between solids and fluid, that satisfy chemical constraints of the water at either end of the flowpath. In this study, three modeling processes are used together to integrate several types of data and observations, as shown in the flow chart below (Figure 9).

Initially, the solubilities of aquifer materials are determined by equilibrium chemistry (Phase 1), using the log K data in llnl.dat, the Lawrence Livermore National Laboratory thermodynamic database. This forward modeling process also returns a charge balance error for each water chemistry, providing confirmation that it is useful for modeling purposes.

In Phase 2, solubility and occurrence of phases in each rock formation inform the inverse modeling process. On its own, inverse modeling generates results without regard to thermodynamic considerations, searching only for arrangements of stoichiometry that meet the specified parameters. It is left to the user to identify and constrain phases to dissolve or precipitate in agreement with saturation indices, and doing so eliminates the need to consider arrays of unlikely model results afterward. For example, secondary minerals tend to be resistant to weathering, and alter slowly by diagenetic processes. Thus, they are specified only to precipitate, in agreement with their (positive) saturation indices.

In Phase 3, where the mixing function is combined with the inverse modeling process, two or more initial waters are input with a single final water chemistry, and mixture percentages of initial waters accompany the sets of mass transfer reactions in results. In inverse modeling, mass balance constraints are limited to elements participating in reactions, which excludes chloride. Working from the mixing ratio and chloride concentrations of the initial waters, chloride concentration is projected for the final water algebraically, as follows:

Cl_{water1} (mix $coefficient_{water1}$) + Cl_{water2} (mix $coefficient_{water2}$) = Final water $Cl_{projected}$

The absolute value difference between this and the actual chloride in the final water, defined here as "chloride mass balance error", is used to identify preferred mixing models independently of the processes performed in PHREEQC (Parkhurst and Appelo, 2013).

Final water $Cl_{projected}$ – Final water Cl_{actual} = |Cl error| = chloride mass balance error

Final mixing estimates are based on minimum Cl mass balance errors and inverse model results that are consistent with preferred Phase 2 results and rock formation data.

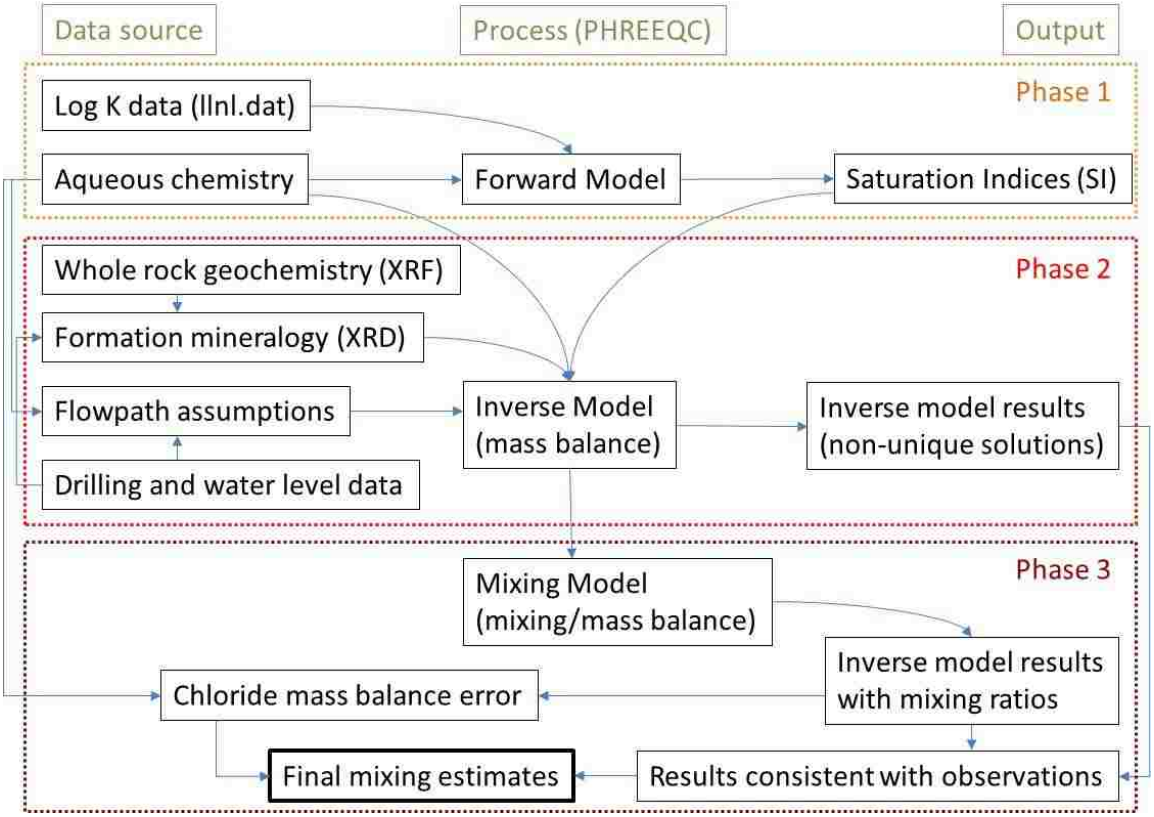

Figure 9: Flow chart showing relationships of data and modeling processes in this study.

2.0.1 Solubility

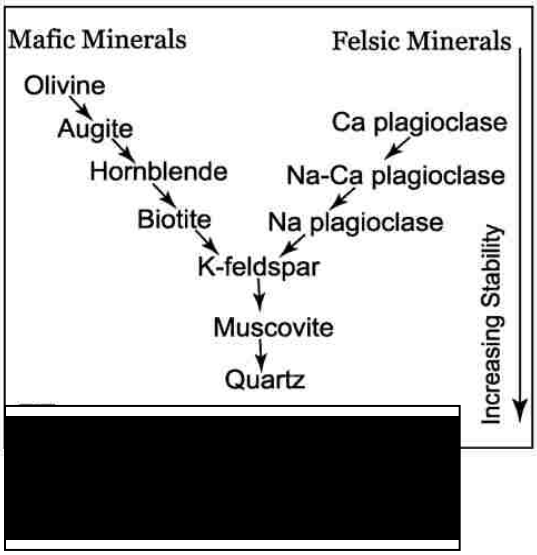

Chemical contributions of rock, to both fluid and secondary minerals, are dependent on mineral content and surface area, time of exposure to groundwater, and weatherability of the mineral phases at near-surface conditions. Langmuir (1996) cites the hierarchy of minerals known as Goldich's Sequence (Figure 10), which reflects the recalcitrance of phases such as quartz and muscovite to chemical weathering, due to their greater bond strength. In contrast, minerals such as calcium plagioclase (anorthite) and hornblende, commonly subject to

hydrolysis and iron oxidation, weather more rapidly and under more neutral conditions. Kinetics are not expressly considered in this study; however, Goldich's Sequence indicates the stability of certain crystalline primary minerals. Silicate alteration products, such as oxides and clay minerals, are also resistant to weathering. Based on a compilation of experimental results and field observations, a guide to relative solubilities of mineral phases is given by Eggleton and Aspandiar (2007) below, with numbers on a base-10 logarithmic scale at left (Figure 11). A comparable hierarchy of resistance to chemical weathering is apparent in the equilibrium constants of various silicates. A list of the logarithmic exponents of their equilibrium constants of is shown at right (llnl.dat). Both lists are shown in order of increasing solubility.

Relative solubility, base 10	
Gibbsite	11
Beidellite	10
Quartz	10
Kaolinite	10
Microcline	9
Muscovite	9
Sanidine	7
Albite	7
Biotite	7
Augite	7
Oligoclase	6
Andesine	5
Hornblende	4
Diopside	4
Bytownite	4
Anorthite	3
Forsterite	2
Glass	1
from Eggleton & Aspandiar, 2007	

Equilibrium constants (log K)	
Quartz	-3.999
Tridymite	-3.827
Chalcedony	-3.728
Cristobalite(alpha)	-3.449
Cristobalite(beta)	-3.005
SiO2(am)	-2.714
K-Feldspar	-0.275
Sanidine	0.924
Albite	2.765
Ferrosilite	7.447
Enstatite	11.327
Hedenbergite	19.606
Diopside	20.964
Anorthite	26.578
Ca-Al_Pyroxene	35.976
Tremolite	61.237
Log K values as used by llnl.dat	

Figure 11: Relative solubilities of silicate minerals at left, equilibrium constants at right. Solubility increases downward in each.

These equilibrium constants have a bearing on the calculation of the saturation state of each mineral phase, as expressed by Saturation Index (SI). Saturation Index is defined as the log of the ion activity product (IAP) divided by the solubility product constant (Ksp), which is the same as equilibrium constant (Keq).

$$SI = \log (IAP/Ksp)$$

The form of each product is the same; in the denominator, Ksp expresses the product at equilibrium, where the IAP expresses a calculation based on measured activities in solution. A positive SI suggests that a mineral is stable or could precipitate, while negative SI values indicate potential dissolving phases. Saturation indices for relevant

mineral phases, calculated by PHREEQC, are listed in Section 3.1 (Forward modeling results). Activity coefficients are calculated in PHREEQC using the Davies equation, where μ is ionic strength and *A* is a constant dependent on temperature, z_i is the ionic charge of the solute, and γ is the activity coefficient:

$$\log \gamma_i = -A z_i^2 \left(\frac{\sqrt{\mu}}{1+\sqrt{\mu}} - 0.3\mu \right)$$

(Parkhurst and Appelo, 2013)

Often (as in every water considered in this study) there is no undersaturation with respect to quartz or K-feldspar. These phases are kept out of Phase 2 inverse models accordingly. Amorphous silica (SiO_2 (am)), however, is undersaturated near equilibrium in all TA-16 waters, suggesting the potential for dissolution of non-crystalline glass.

Volcanic glass is metastable; Marshall (1963) and others note that in volcanic rocks older than Miocene, glass is nearly always missing, and is therefore considered a phase that is easily weathered (White and Claassen, 1980). As glass is not a mineral, in part because of compositional and structural variability, it is not represented in the database. A method for estimating an equilibrium constant for hydrated volcanic glasses is suggested by Wolff-Boenisch et al. (2004); this assumes a composition of hydrated glass leached of loosely bonded surface cations, and breaks it up into silicic acid and aluminum hydroxide, compounds with known log K's. By this method, a log K can be calculated with the molar ratio of Al to Si, as follows. The average Al/Si ratio in Tschicoma dacite is 0.27:

$SiAl_{0.27}O_2(OH)_{0.81} + 0.81\ H^+ + 1.19\ H_2O = H_4SiO_4 + 0.27Al^{3+}$ (Wolff-Boenisch et al., 2004)

SiO_2 (am) + 2 H_2O = H_4SiO_4; log K -2.71 (PHREEQC)

$Al(OH)_3$ + 3 H^+ = Al^{3+} + 3 H_2O; log K 10.8 (PHREEQC)

[1(Si)*(-2.71)] + [0.27(Al)*(10.8)] = log K for dacitic glass = 0.2

The same calculation for rhyolitic glass can be made, based on an average Al to Si ratio of 0.21:

[1(Si)*(-2.71)] + [0.21(Al)*(10.8)] = log K for rhyolitic glass = -0.44

To be clear, weatherability is estimated by taking the logarithm of a fraction, in which an equilibrium constant is the denominator. The log K values are comparable across phases that have the same chemical composition, such as quartz, tridymite, cristobalite, amorphous silica, and, approximately, glass. The near-zero log K values calculated above for glasses suggest that they are well within the range of phases susceptible to weathering, provided that the fluid is undersaturated with respect to amorphous silica as well. A larger denominator, with a log K of close to zero, gives a smaller fraction. If the SI is equal to one, equilibrium is achieved. Only where that fraction is less than one will the water be considered undersaturated with respect to the phase. These observations suggest that it is reasonable to include dacitic or rhyolitic glass as dissolving phases where quartz, tridymite and cristobalite are excluded, due to supersaturation. In practice, volcanic glass may weather far more readily than these estimated log K values suggest.

2.0.2 Inverse model construction

A stated previously, inverse modeling reconciles changes in aqueous chemistry along a flowpath by proposing specific exchanges between solid phases and fluid. The phases

specified to dissolve are documented to occur in the formation and have negative saturation indices; secondary precipitating phases are identified in XRD data from the formation. Almost all clay mineral phases are associated, in these waters, with positive saturation indices, though only one or two are observed as actual precipitates. Saturation indices are not predictive in that sense. Positive saturation indices identify phases with the potential to precipitate; however, not all minerals precipitate out of solution at low temperatures and pressures. With respect to these, positive saturation indices are perhaps better thought of as indicators of stability.

Certain ion-exchange reactions are relevant to silicate dissolution, and are included accordingly. The most important ion exchange reaction accounts for the tendency of sodium, as a cation displaced by hydrolysis, to remain in solution. Sorption of free sodium to clay mineral surfaces occurs, though it is reversed to some degree as calcium replaces it, pushing sodium back into the fluid. In the modeling, this has the effect of loosening the constraint imposed by sodium, allowing the inverse function to search for a slightly wider array of solutions; without ion exchange, the sodium dissolved is very close to the sodium in solution (Bowser and Jones, 2002).

The applicability of inverse mass-balance models is dependent on several factors, as described here. First is the assumption of a valid continuous flow pathway. Though uncertainty with respect to mixing along a flow path is unavoidable, it can be minimized by observing reasonably consistent values of a conservative parameter, such as Cl^-. Significant changes in chloride along an assumed flow pathway, one which is not associated with marine rocks or evaporites, indicate potential problems with this

assumption. Similarity of water level elevations suggests that well screens are situated in the same hydrostratigraphic unit, though again mixing along flow pathways could occur.

Additional assumptions of mass-balance modeling are that dispersion and diffusion have no meaningful effect on overall chemistry, and that sequestration of water enriched with respect to a particular solute, for example in dead-end pores, is insignificant. Steady-state flow and chemistry are assumed, and any temporal fluxes are overlooked. This is a reasonable assumption given the long timescales of deep groundwater flow.The water chemistry profiles used are aggregates of analytical samples for each sampling point; most of the data spreads across all seasons and many years. Therefore, variability associated with seasonal fluxes or drought conditions are largely averaged out as noise.

The specification of appropriate mineral assemblages is of great importance to valid results. In a review paper specific to silicate hydrolysis, this point is stressed by Bowser and Jones (2002), who observe that model results are sensitive, in particular, to many of the phases considered in this study: plagioclase compositions, secondary clay minerals such as smectite, and common mafic minerals such as pyroxenes. With respect to feldspars and pyroxenes, thermodynamic standards in the PHREEQC databases (llnl.dat alone is used for this study) are set for end-member compositions. Plagioclase, for example, as a solid solution of sodium and calcium feldspar, is not included as mineral phase in the database; but rather, the pure phase end-members albite and anorthite are used. While useful in determining saturation indices of various materials exposed to groundwater, end-member mineral compositions are less helpful as phases in mass-balance models. Solid solution minerals are provided to PHREEQC as necessary, by creating balanced dissociation reactions specific to each rock formation. Available XRF

data is used for this purpose; this is described below in Section 2.2.5, Phase specifications based on whole rock data.

2.1 Geochemical reactions in modeling processes

The following sections introduce the relevant dissolution and precipitation reactions used in PHREEQC to account for hydrochemical evolution along flow pathways.

2.1.1 Incongruent dissolution of silicates

As silicates exposed to groundwater dissolve, stabilities of the products are variable. Some elements remain in solution as free ions, while others either resist dissociation or complex immediately. Aluminum remains mostly in a solid phase that is not seen in aqueous chemistry data; it is, however, an important component of clays. 'Incongruent dissolution' describes the removal of cations from a crystalline structure, rendering the solid structure as amorphous. By coupling primary dissolution reactions with secondary precipitation reactions, the modeling program is able to account for mass transfer in stoichiometric terms, without requiring aluminum or iron to be measured in solution. If precipitation reactions are not joined with dissolution reactions, and aluminum is weak in solution, the mass transfer of other cations from aluminosilicates will be limited, perhaps not accounting for what occurs in solution.

Incongruent dissolution by acids, in which hydrolysis reactions facilitate preferential release of certain cations from a mineral, is an important mechanism of silicate weathering, and the means for dissolution of both feldspars and volcanic glasses (White et al., 1980; Velbel and Barker, 2008). Protons that drive these weathering reactions are normally supplied by dissolved CO_2 (carbonic acid), which leaves bicarbonate behind. The plagioclase dissolution reaction consumes H^+ ions and results in free cations and an

insoluble aluminosilicate solid, in addition to the bicarbonate. Similarly, calcite dissolution can consume protons together with plagioclase dissolution, leaving water, bicarbonate and aluminosilicate behind, with additional calcium cations. Again, carbonic acid can contribute protons and increase resultant bicarbonate. Generalized reactions for dissolution of solid solution plagioclase feldspar are (amorphous phase is indicated in braces):

CO_2 dissolution: $CO_2 + H_2O = HCO_3^- + H^+$

Plagioclase dissolution: $\underline{\text{Plag.} + H^+ = Na^+ + Ca^{2+} + \{Al^{3+} + SiO_2\} + H_2O}$

$$CO_2 + \text{Plag.} = Na^+ + Ca^{2+} + \{Al^{3+} + SiO_2\} + HCO_3^-$$

Calcite dissolution: $CaCO_3 + H^+ = Ca^{2+} + HCO_3^-$

Plagioclase dissolution: $\underline{\text{Plag.} + H^+ = Na^+ + Ca^{2+} + \{Al^{3+} + SiO_2\} + H_2O}$

$$CaCO_3 + \text{Plag.} + H^+ = Na^+ + Ca^{2+} + \{Al^{3+} + SiO_2\} + HCO_3^- + H_2O$$

CO_2 dissolution: $CO_2 + H_2O = HCO_3^- + H^+$

Calcite dissolution: $CaCO_3 + H^+ = Ca^{2+} + HCO_3^-$

Plagioclase dissolution: $\underline{\text{Plag.} + H^+ = Na^+ + Ca^{2+} + \{Al^{3+} + SiO_2\} + H_2O}$

$$CO_2 + CaCO_3 + \text{Plag.} + H^+ = Na^+ + Ca^{2+} + \{Al^{3+} + SiO_2\} + HCO_3^-$$

2.1.2 Clay mineralogy

Aluminosilicate solids typically reorganize to clay minerals. Clays observed in XRD analyses of TA-16 materials are limited to kaolinite and smectite, with the latter dominant. Kaolinite has a two-layer structure, with octahedral layers of Al^{3+}, in coordination with O^{2-} and OH^-, stacked between tetrahedral layers of silicon and oxygen. Smectite is a three-layer phyllosilicate, with octahedral layers sandwiched between two

layers of silica tetrahedra. In a smectite, Mg^{2+} or Ca^{2+} may often substitute for Al^{3+} in the octahedral layer, and Al^{3+} or Fe^{3+} may substitute for Si^{4+} in tetrahedral layers. Such substitutions, or alternatively, vacancies, create charge imbalances that are typically satisfied by adsorption of interlayer cations (Langmuir, 1996). The space created by interlayer cations allows for water molecules to enter, which is why smectites are known to swell with hydration. Kaolinite precipitates under wet conditions where leaching of cations is enhanced.

At well LAOI(A)-1.1 in Los Alamos Canyon, Vaniman et al. (2005) observed a pattern of initial precipitation of smectite clays along fracture surfaces, followed by kaolinite precipitation along axial zones, possibly resulting from a later introduction of water. As previously discussed, in Los Alamos Canyon surface flows provide hydraulic head directly to Otowi Member tuff fractures, as the Tshirege vadose zone is absent. While kaolinite generally follows a pure composition, smectites are variable. The mixed-cation composition “low Fe-Mg smectite” is given below; this is appropriate for clays developing from dissolution of the felsic (i.e., tuff) and intermediate (i.e., dacite) composition rocks at TA-16. The “high Fe-Mg smectite”, which relates to ultramafic rocks, is not applied in this study, and even mafic rocks such as basalt are not found in TA-16. Other smectite group (2:1) clay compositions, such as montmorillonite or nontronite, are available in the database; however, these are specific to the cations Ca, Cs, K, Mg, and Na, so they are not considered as useful in an environment where there is not a single type of enrichment occurring. In this study there appears to be undersaturation and perhaps dissolution of plagioclase, glass, and pyroxene together. Illite, though it is

also a mixed-cation clay, is considered less likely in this environment because it requires wet conditions and long times; illite is often considered a diagenetic product of smectite.

Kaolinite precipitation:

$2.0\ Al^{3+} + 2.0\ SiO_2 + 5.0\ H_2O = Al_2Si_2O_5(OH)_4 + 6.0\ H^+$
(llnl.dat)

Smectite precipitation:

$0.02\ Ca^{2+} + 0.15\ Na^+ + 0.16\ Fe^{3+} + 0.2\ K^+ + 0.29\ Fe^{2+} + 0.9\ Mg^{2+} + 1.25\ Al^{3+} + 3.75\ SiO_2 + 4.5\ H_2O = Ca_{.02}Na_{.15}K_{.2}Fe^{2+}{}_{.29}Fe^{3+}{}_{16}Mg_{.9}Al_{1.25}Si_{3.75}H_2O_{12} + 7.0\ H^+$
(llnl.dat)

Concurrent dissolution of a mafic silicate could provide the necessary cations for precipitation of a smectite composition to occur, if they are not already bound up in the original glass phase. Iron tends to sorb to solids or complex to form iron oxyhydroxides. Clay minerals have abundant interlayer surface areas, and thus retain iron that might otherwise be in solution. Clay mineral precipitation appears to be controlled less by thermodynamic considerations, and more by mineral structures of dissolving phases at the molecular level, as well as the type of leaching environment (Eggleton and Aspandiar, 2007).

The aluminum hydroxides gibbsite and boehmite, though associated with positive saturation indices, do not result directly from feldspar dissolution (Eggleton and Aspandiar, 2007). Like quartz or tridymite, these are stable. They would be left behind if, for instance, kaolinite were to dissolve. However, kaolinite is also highly stable. Rather, supersaturation of gibbsite indicates the stability of octahedral Al^{3+} and hydroxide structures, which are referred to as “gibbsite layer” in clay mineralogy. Thus, hydroxides

of aluminum are not expressly considered as precipitating phases in mass balance modeling, though their precipitation is implied.

2.1.3 Glass dissolution

Like silicate minerals, glass dissolution also consumes protons and produces bicarbonate (White and Claassen, 1980), and could be pushed by carbonic acid. Reactions for dissolution of volcanic glass were added to the database for this study, as none are provided by llnl.dat. A dissolution reaction given by Wolff-Boenisch et al. (2004) yields silicic acid and aluminum, which then decomposes to silica, water, and aluminum:

Glass dissolution: $SiAl_{0.27}O_2(OH)_{0.81} + 0.81\ H^+ + 1.19\ H_2O = H_4SiO_4 + 0.27Al^{3+}$

Silicic acid dissociation: $H_4SiO_4 = SiO_2\ (am) + 2\ H_2O$

$SiAl_{0.27}O_2(OH)_{0.81} + 0.81\ H^+ = 0.81\ H_2O + 0.27Al^{3+} + SiO_2$ (am)

The 1:1 molar relationship of Al and Si in kaolinite clay is not seen in volcanic glass; rather, the ratio in smectite clay, 1.25/3.75, or 0.33, is closer to what is observed in glassy rocks. Whole rock geochemical analyses, using XRF, were used to derive Al/Si molar relationships in both dacite and rhyolite glass. The ratio for Tschicoma Formation dacite averaged 0.27 (Broxton et al., 2007), consistent with the example above, while the more silica-rich rhyolite averaged 0.21. For dissolution of these types of glass to result in kaolinite clay, additional Al would be required; for smectite precipitation to occur, some amount of silica would result as well, either dissolved or as a secondary mineral.

Along the flowpaths considered in this study, potassium increases noticeably; however, in the forward model results, feldspars with K are not expected to dissolve (sanidine or microcline in Figure 11). To accommodate potassium flux in the modeling, K is included in glass dissolution reactions, according to the molar ratio of potassium to silicon in whole rock analyses. Starting with the reaction shown above, K and Al are adjusted and balanced accordingly for rock formations expected to have reactive glass.

2.1.4 Dissolution of mafic silicates

Velbel and Barker (2008) note that pyroxenes are known to weather to smectite compositions, which would require addition of some amount of aluminum; this is probably because they always do so in the presence of feldspar minerals or glass. By themselves, pyroxenes and amphiboles are expected to be dissolved congruently by acids, consuming protons and leaving cations, bicarbonate, and silica behind. Mafic silicate dissolution yields some cationic iron, which can become manifest as oxides or go into clays; magnesium substitutes for iron in solid solution, though for simplicity this is not shown in the following end-member dissolution:

CO_2 dissolution: (llnl.dat) $4\ CO_2 + 4\ H_2O = 4\ HCO_3^- + 4\ H^+$

Ferrosilite dissolution: (llnl.dat) $Fe_2Si_2O_6 + 4\ H^+ = 2\ H_2O + 2\ Fe^{2+} + 2\ SiO_2$

$$Fe_2Si_2O_6 + 4\ CO_2 + 2\ H_2O = 4\ HCO_3^- + 2\ Fe^{2+} + 2\ SiO_2$$

In mafic silicates, dissolution also results from iron oxidation, when an electron is stripped, for instance from a pyroxene molecule composed of silica and reduced iron.

Ferric iron has a smaller ionic radius, and the change in size causes breakage of the chemical bond. When ferrous iron is oxidized, it transforms to ferric hydroxide and then the mineral ferrihydrite, $5Fe_2O_3 * 9H_2O$, which adsorbs phosphate and silica, as well as metals and organic molecules (Eggleton and Aspandiar, 2007). Ferrihydrite can be dehydrated and rearranged into hematite, in warm regions, or crystallized to form goethite in cool regions (Langmuir, 1996). It may be possible for geochemical models to balance silicate dissolution with silica, oxides and protons - by oxidation alone, effectively; however, it is more likely that congruent dissolution and oxidation work together, and a smectite composition precipitates, dependent on concurrent dissolution of glass, plagioclase and pyroxene. Hematite may form as smectite is altered by loss of silicic acid, in the same way that gibbsite is considered as an alteration product of kaolinite. However, it is unlikely that this process is important here, as sufficiently low pH conditions do not apply. In soils, Al- and Fe-oxides are common only in hot, wet climates (Langmuir, 1996). In the groundwater studied here, goethite may be as likely to precipitate as hematite; it differs only by a water of hydration. It is assumed that no discernably different results would be given by specifying one or the other. Hematite is chosen, as it turns up more commonly in XRD data.

2.1.5 Phase specifications based on whole rock analytical data

This section outlines a process used to express solid solution mineral compositions in balanced reactions, allowing geochemical data to be used in inverse modeling. While end-member compositions are useful for evaluating solubility, as in the results of forward modeling, they are of limited use in inverse modeling. PHREEQC allows for specified phases to be used alongside those in a database, using the PHASES keyword and

balanced chemical reactions. This allows for an estimated plagioclase composition, for example, to be input as a ‘fictive phase’, improving the model calculation (Bowser and Jones, 2002). Though a fictive phase, unaccompanied by thermodynamic data, generates a spurious saturation index when the model is run (Parkhurst, 2013), it replaces the two end-member phases with one phase, scaled to the cation ratio as derived from whole rock XRF data. This practice aids in bringing the number of phases closer to the number of solute constraints in a model. The necessary balanced dissolution reactions are written as follows: first, the general formula for a weatherable phase is set up for cationic substitution. Stoichiometry of cations is based on molar ratios of calcium to sodium for plagioclase feldspar, iron to magnesium for pyroxene, hornblende and biotite, and aluminum to silicon for hydrated volcanic glass. Reactions are mass- and charge-balanced with water on the right, and hydrogen on the left. As the molar ratios are average values from the available whole-rock data, the phase reactions generated by this process aim to minimize the error introduced to inverse modeling. Fictive phase calculations are included in Supplementary Materials, part c.

2.2 Data and observations

This section introduces specific information relevant to guide inverse model construction: known or assumed groundwater flow patterns and estimates of mineral occurrence, as well as aggregated water chemistry profiles for each site.

2.2.1 Lithology and mineralogy of rock formations

The Tschicoma Formation, composed of dacitic rock of intermediate composition, erupted as a series of overlapping lava domes around 3 million years ago. Weathering of Cerro Grande and Pajarito Mountain, the domes adjacent to upper Cañon de Valle,

contributed locally to the sedimentary Puye Formation; of the several compositionally distinct dacites in the formation, these are predominant at TA-16 (Broxton et al., 2007). The dominant silicate is plagioclase feldspar, which makes up between 50 - 70% of the rock. Mafic silicates, primarily orthopyroxenes, are present at nearly 15%. There is a lesser amount of clinopyroxene, which is essentially orthopyroxene with some amount of calcium substitution in place of Fe or Mg. The amount of calcium in clinopyroxene is considered negligible compared to what is present in plagioclase, so it is overlooked in the modeling. Hornblende is also present, and though scarce compared to the other minerals, it is highly weatherable. The ratio of iron to magnesium is used to compose a specific formula for both orthopyroxene and hornblende.

The crystalline silica phases cristobalite and tridymite make up between 10 – 20% of the rock. No potassium feldspar, quartz or muscovite is observed in the Cerro Grande dacite. Smectite clay is observed in associated interlava siltstone at R-37-2, estimated at between 35 and 45 wt%. In XRD analysis, the smectite is shown to lack traces of relict mica that are present in soil clays, indicating that it formed at depth (LANL ER2002-0557). A Formation Micro Imager (FMI) log shows a massive lithology in well R-48 (Figure 12, right), which would allow for a limited amount of slow groundwater flow along fractures. The outer margin of the lava formation has a flow breccia lithology, which results from advancing surges of lava continually being rapidly quenched, and breaking through previously quenched flows. The FMI log of flow breccia in R-37-2 (Figure 12, left) suggests a far greater degree of permeability, and it is reasonable to expect that glassy materials are present in the breccia, due to quenching. In XRD analyses of dacite clasts in the Puye Formation at well R-37-2, glass is estimated at 33.7 wt%. The same sample has

plagioclase at 41.3 wt% and alkali feldspar (solid solution of Na- to K-Feldspar) at 8.5 wt%. Only plagioclase feldspar phenocrysts, and no K-feldspar, are seen in the lava; however, potassium oxide is represented in XRF data at around 3 wt%. An assumption is made that most of the potassium is present in glass. In the Tschicoma Formation, given that the most water is expected to reside in flow breccia, there is an unknown but possibly significant influence of dacitic glass as a non-crystalline silica phase. Therefore, a glass phase is specified, based on the ratio of Al to Si (Wolff-Boenisch et al., 2004). Because it is necessary as a component in PHREEQC modeling, K is incorporated in the amorphous phase of hydrated volcanic glass, according to the molar ratio of K to Si from elemental conversion of XRF data.

Calcite, as pedogenic calcite, is expected to be present in formations where soil horizons may exist, including the Puye and Cerro Toledo Formations, and Tshirege Member (Newman et al., 1997). Chalcedony, which tends to have positive saturation indices in these waters, is explored as a possible precipitate and outlet for excess dissolved silica, though is unclear what factors might control this type of precipitation. The actual secondary silica product may not be chalcedony; rather, it may be opal-CT, as appears in QXRD data from R-25, where opal has been observed in fracture fills within the Bandelier Tuff (LANL ER2001-0697). All secondary mineral compositions are as defined in the llnl.dat database. The ion exchange reaction with calcium keeping sodium in solution is used as well. Potential reactant phases in dacite are: plagioclase, orthopyroxene, hornblende, dacite glass with K, chalcedony, calcite, smectite, hematite, kaolinite, and both O_2 gas (DO) and carbon dioxide gas.

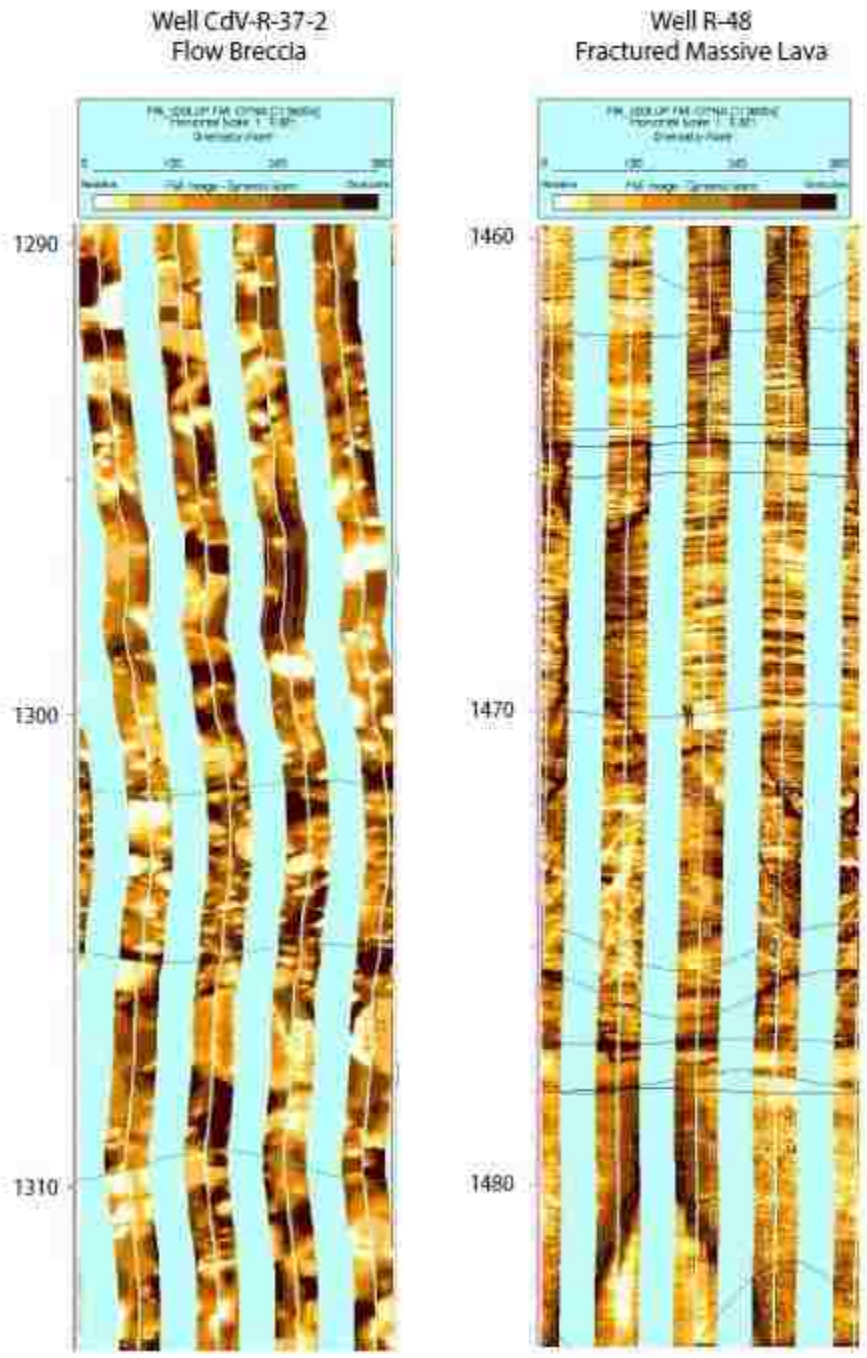

Figure 12: Comparison of Formation Micro Images (FMI) of flow breccia (left) and massive dacite lithologies (LANL EP-2016-0113)

The Puye Formation, deposited in the interim between Tschicoma lava flows and eruption of the Otowi Member of the Bandelier Tuff, is composed of variously weathered products of dacitic rocks. The fanglomerate facies present at TA-16 is heterogeneous, with boulder, cobble, gravel, sand and silt beds. The mineralogy is similar to that of the Cerro Grande dacite, though it differs in minor ways, as other dacites sources contribute small amounts of K-feldspar, biotite and quartz. A biotite phase is explored as a possible reactant in Puye Formation inverse models.

The differences between Tschicoma and Puye whole rock chemistries appear minor, with the Puye having slightly more silica, less calcium, and less iron (Figure 13). Away from the lava flow, there is perhaps less reactive glass, but more surface area. In the XRD analyses for R-25, glass is between 8 and 20 wt% for 7 different depths. Smectite is between 0 and 2 wt%, and kaolinite is absent in the Puye. Feldspars, which are unlikely to include significant K-feldspar, are between 52 and 66 wt%. Quartz, cristobalite and tridymite are present but not indicated to react. In soil horizons, some amount of pedogenic calcite may be available.

Chemically, there are obvious similarities between the Tschicoma and Puye Formations, as well as between the Tshirege and Otowi Members of the Bandelier Tuff, as seen in Figure 13. The differences between these groups is used to advantage in this study; beyond this, the solubility of glass is expected to be useful in differentiation and mixing of waters in the PHREEQC geochemical models.

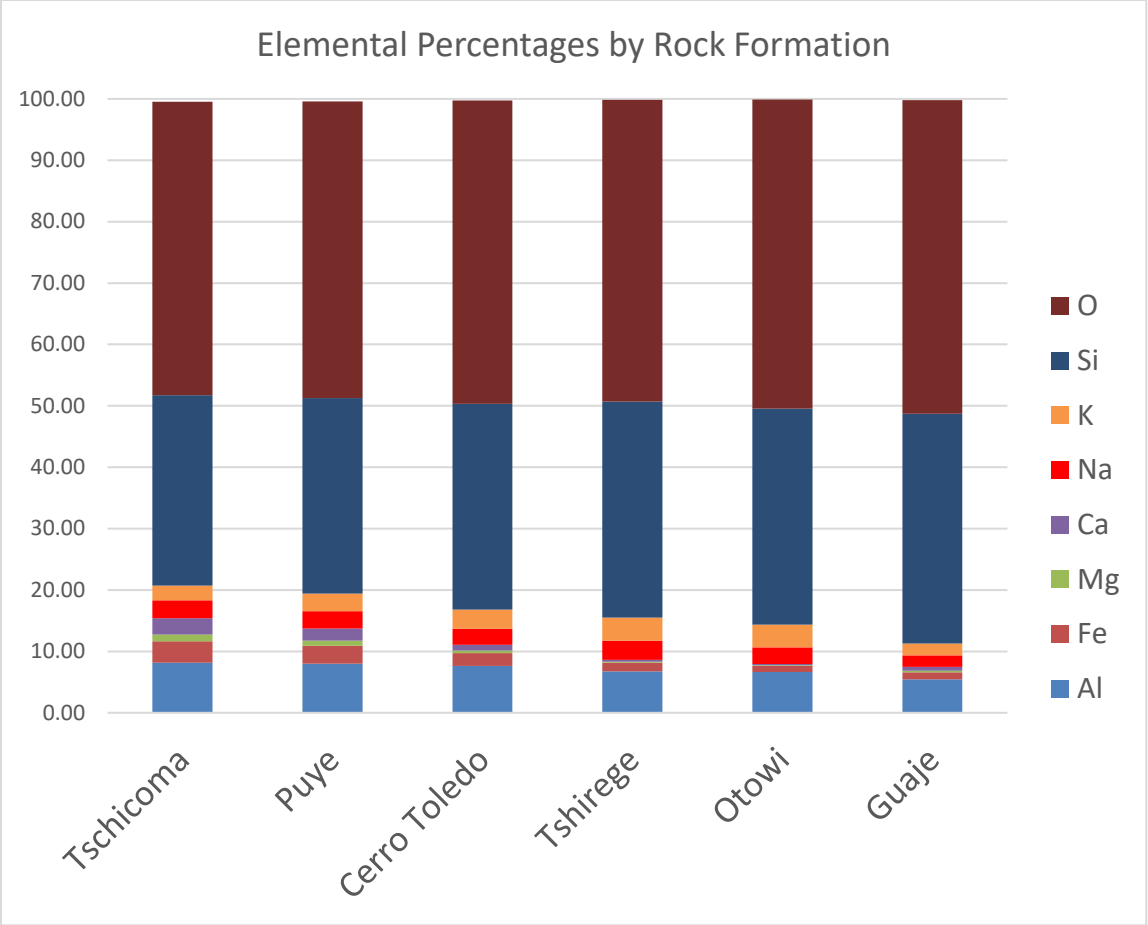

Figure 13: Average elemental weight percentages from available whole rock (XRF) data. Derived from data in (LANL ER2001-0697), (LANL ER2002-0557),

The two Bandelier Tuff units, the Otowi Member and the Tshirege Member, were emplaced by pyroclastic flows occurring 1.61 and 1.22 million years ago, respectively (LANL EP-2016-0113). Both differ compositionally from the rock formations described above in several ways. The tuffs are characterized by a greater degree of silica and less of the metals Ca, Fe and Mg. The Guaje pumice bed, at the base of the Otowi Member, is described as porous, glassy, and a potentially important lateral flow pathway. It also may serve as a capillary barrier. Though there are both quartz silica and abundant sanidine

(K-feldspar) in the Otowi, glassy silica dominates, at between 50 and 90% of the rock. For model runs in the Cerro Toledo/Otowi and Tshirege, a different plagioclase composition and a rhyolitic glass phase are specified using the same method as in the Tschicoma and Puye Formations. Mafic minerals, including biotite, are present in small amounts. Clay minerals are also present, probably mostly absent from the rock matrix but abundant along fractures.

Vaniman et al. (2005) provides a thorough account of clay mineralogy in Los Alamos Canyon, a drainage to the north which, like Cañon de Valle, has headwaters in the Sierra de los Valles. In the vadose zone of borehole LAOI(A)-1.1, QXRD data for the Otowi Member and basal Guaje pumice bed are similar to data from Cañon de Valle: hydrated volcanic glass as the dominant phase, with secondary feldspars and quartz in a fine-grained matrix. Petrologic analyses of fracture zones in the Otowi Member show smectite growth lining fracture walls with kaolinite primarily along fracture axes, or filling fractures developed after initial smectite growth. Kaolinite occurrence in Los Alamos Canyon correlates to zones of prolonged saturation in vertical tuff fractures, alluvium and, particularly, the Guaje pumice bed. In R-25, the same clays are indicated by QXRD analyses: the same stratigraphic section shows only traces (up to 2%) of smectite, and even less kaolinite, though a downhole video shows continuous flow of groundwater along open high-angle fractures (LANL ER2001-0697). Though neither clay composition is apparent in the Guaje pumice bed at R-25, precipitation of at least a small amount of smectite is assumed, along with possible kaolinite precipitation in zones of saturation. Abundant fine smectite was noted in an interflow zone in well R-37-2, between screens 3 and 4, during drilling, and this is thought to be authigenic, rather than transported from

elsewhere. At TA-16, kaolinite occurrence is generally discounted in this study, for the reason of more constrained flow conditions in the subsurface compared to LA Canyon; however, the possibility is considered in all modeling. A positively-correlated relationship between clay precipitation and water abundance in the Otowi Member is illustrated in Figure 14

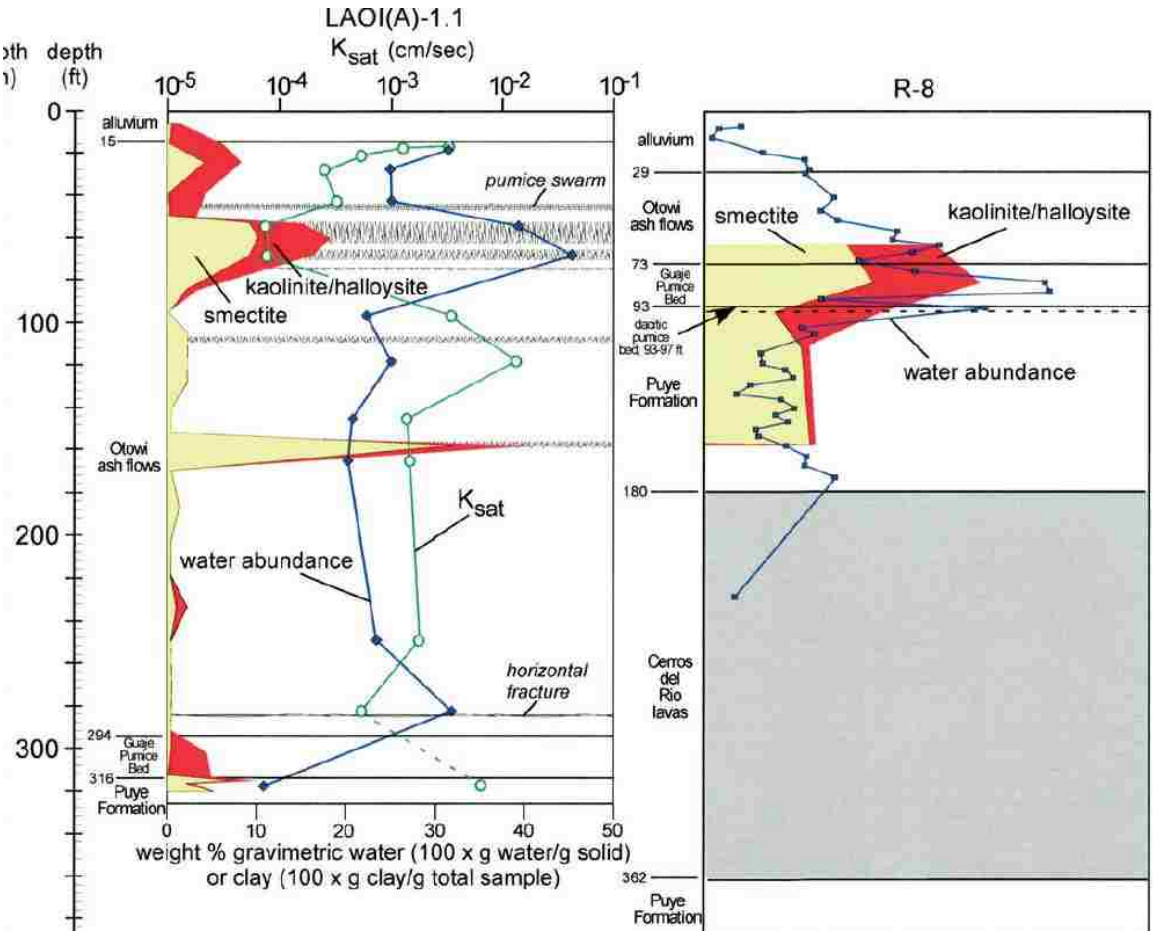

Figure 14: Clay mineralogy in the same rock formations under different flow conditions. (Vaniman et al., 2005)

The Tshirege Member has a similar overall composition to the Otowi, but differs in that it is composed of multiple distinct cooling units, many of which have undergone vapor-

phase alteration, resulting in less glassy silica. Glass is present at the base of the unit, in the Tsankawi pumice bed (in Qbt1g), and near the surface (in Qbt4) (LANL ER2001-0697). However, the groundwater in the Tshirege that emerges from Burning Ground and SWSC Springs, and is sampled in piezometer 2 of R-26 and well 16-26644, resides in unit 3t, a densely-welded ignimbrite (LANL EP-2016-0113). Martin Spring water chemistry is distinct, for reasons that are poorly understood; however, it emanates from Qbt4, so glass dissolution may be a major factor.

The Cerro Toledo Formation, deposited between the Otowi and Tshirege, is essentially composed of weathered fragments of the Otowi ignimbrite tuff, though it also includes clasts of dacite that were eroded during that time. In Cañon de Valle, the Cerro Toledo has a thickness of more than 300 feet and appears to fill a paleochannel eroded into the Otowi Member (LANL ER 2005-0679). This, together with the porosity of these rocks, supports the idea that a reservoir of mountain block groundwater could reside in the Cerro Toledo. However, the absence of tritium in well R-26 screen 1 suggests that this water is not influenced by recent snowmelt recharge through the fault zone, and is perhaps weakly connected to underlying groundwater in the Otowi, which does respond to snowmelt recharge events.

Though the hydraulic interconnectedness of groundwater zones is expected to be complex, the chemical influences are resolved, in this study, to correspond with the three main contributors to intermediate water at TA-16: water associated with dacite and weathered dacite rock chemistry, water associated with glassy tuff and pumice clasts, and alluvial aquifer water.

2.2.2 Aqueous chemistry data

Validated aqueous chemistry data used in this study are all publicly available at www.intellusnm.com. Analytical data collection methods consist of: ICP- AES for calcium, sodium, magnesium, iron, potassium, dissolved silica and some aluminum; ICP-MS for other aluminum concentrations; and IC (ion chromatography) for inorganic anions such as chloride. Alkalinity was determined by titration using EPA method 310.1, and pH values were determined electrometrically with pH meters. For each sampling location, mean solute values were compiled for all available filtered samples, resulting in aggregated water chemistry profiles (Table 1). The number of samples input to arrive at mean values varies widely, as a function of the age and sampling program of the well screen. The purpose of averaging water chemistry was to capture broad trends in spatial variability across the field area, while overlooking temporal variability and analytical error associated with any particular samples. Also, by this method charge balance errors are reliably smaller than when using particular water samples. Mean values for temperature, pH and ORP, are available from field condition records for each source. Using temperature and ORP, values for pe were calculated using the Nernst equation, though the effect of pe to the modeling appears negligible. Conditions are generally oxidizing, and several field records include dissolved oxygen concentrations. Water in the Cañon de Valle alluvial aquifer has relatively uniform characteristics, and data from three different shallow wells in this alluvial zone are considered as one location.

Unit	Alluvial Groundwater	Springs emerging from Tshirege Member			Tshirege Member of Bandelier Tuff		Cerro Toledo Formation	Otowi Member of Bandelier Tuff	
pH unit or mg/L	Aggregate of 3 wells in Cañon de Valle	Burning Ground Spring	SWSC Spring	Martin Spring	R-26 PZ2	16-26644	R-26 Screen 1	16-1i	R-25b
pH	7	7.34	7.0	7.06	7.07	7.2	7.55	7.2	7.46
Al	3.5	0.7	1.0	1.0	0.2	0.5	0.0	0.0	0.2
Ca	19.9	18.2	17.5	29.6	24.0	15.1	7.7	13.2	11.0
Cl	23.3	19.7	17.1	24.8	6.7	18.9	1.3	6.7	2.2
Fe	0.2	0.3	0.5	0.5	0.04	0.2	0.0	0.0	0.1
Mg	5.8	5.5	5.3	7.0	6.1	5.0	2.9	5.5	3.7
K	4.1	3.3	3.1	3.0	2.9	3.0	2.2	2.4	1.5
Na	29.8	16.2	16.3	32.7	9.9	15.7	8.4	12.0	17.1
SiO2	39.3	41.3	40.4	48.1	32.1	44.8	58.7	58.2	54.9
SO4	15.0	9.4	9.9	17.5	4.0	6.9	1.4	9.8	5.9
TDS	216	153.3	161.2	224.8	142.3	154.2	99.8	142.7	119.2
HCO_3^-	92	65.4	64.1	98.8	89.6	55.6	48.2	58.6	72.7

Table 1a: Aggregate water chemistry for springs, shallow intermediate zones, Cerro Toledo Formation and Bandelier Tuff waters. www.intellusnm.com

	Spring 5.29	**Puye Formation Intermediate Water**					**Puye Formation Regional Water**		**Tschicoma Formation Regional Water**		
		9-1 (i)	16-4ip Screen 1	16-2 ir	R-47i	16-4ip S2	R-47	R-63	R-48	R-37-2 S3	R-37-2 S4
pH	6.92	7.43	7.31	7.3	7.15	7.5	7.51	7.44	8.12	7.8	7.54
Al	0.9	0.19		0.0			0.00	0.07	0.04	0.03	0.03
Ca	7.4	10.8	10.6	9.4	10.4	9.9	9.6	9.6	10.3	9.9	9.0
Cl	1.4	11.1	3.5	2.5	3.3	2.1	1.7	1.3	2.6	1.9	2.0
Fe	0.3	0.13	0.0	0.0	0.1	0.2	0.03	0.03	0.1	0.08	2.38
Mg	2.8	3.6	3.1	2.4	2.6	3.1	2.9	3.0	3.3	3.0	2.7
K	1.5	1.3	1.0	0.3	0.6	0.7	0.9	0.8	1.3	1.4	1.7
Na	3.9	22.2	10.2	12.9	17.6	9.9	9.7	8.3	13.2	11.3	10.8
SiO2	32.7	48.1	61.2	62.4	61.3	59.1	58.4	60.0	54.4	64.3	59.4
SO4	6.1	7.3	3.7	4.1		3.6	1.6	2.5	4.7	2.0	2.0
TDS	79.0	134.5	117.7	111.6		119.3	97.7	100.4	113.5	127.7	122.8
HCO_3^-	33.1	64.6	47.7	51.4	58.7	48.1	50.6	48.8	57.3	57.1	56.7

Table 1b: Aggregate water chemistry for locations in regional and lower intermediate groundwater zones.

2.2.3 Trends in water chemistry

Inferences drawn from trends in aggregated water chemistry at individual sites help to inform inverse model design for discrete flowpaths (Table 2a) and mixing experiments (Table 2b).

- Spring 5.29 water is lowest in TDS and HCO_3^-, and nearly the lowest in chloride, silica and pH. These data suggest younger, less evolved water, consistent with the spring location in Upper Cañon de Valle.
- Most of the wells that have small Cl concentrations (below 2 mg/L) are in regional groundwater. Exceptions to this are R-26 Screen 1 and R-25b, with 1.3 mg/L and 2.2 mg/L, respectively. Other intermediate wells have slightly more Cl than regional (2.1 to 3.5 mg/L), but what stands out is 9-1(i), with 11 mg/L. Tshirege zone groundwater has higher Cl as well, probably indicating input from evaporated alluvial aquifer water.
- It is interesting that Martin Spring has the highest average Cl, higher than aggregate alluvial well water. It also has the highest concentrations of Na, Ca and Mg, the highest TDS, bicarbonate and sulfate, but not the highest silica. With respect to all of these parameters, it differs noticeably from both SWSC and Burning Ground Springs.
- In the Puye and Tschicoma Formations, calcium is consistently around 10 mg/L, and magnesium is consistently around 3 mg/L. In CdV-9-1(i), though Cl, Na, and SO4 are high, Ca and Mg are consistent with other intermediate wells. Silica is lower by more than 10 mg/L, and bicarbonate is higher; in these respects, it is similar to water in the Tshirege Member (Qbt3t) sites.

- Alluvial groundwater has more dissolved aluminum than any other groundwater in the system.
- R-26 PZ2 and 16-26644 are quite different, though they are in the same hydrostratigraphic unit, the shallow intermediate zone perched on the Qbt3/Qbt3t interface. The proximity of R-26 to the canyon, and the possibility that a greater amount of water moves through the zone, may explain why these are effectively two distinct end-members.

2.3 Inverse modeling flowpaths

All discrete and mixing model experiments (model runs) are designated by capital letters, A-U, in order to avoid confusion with numbered figures and tables in this document. In the Results and Discussion sections, individual models generated by the model experiments are designated by the letter followed by a number, corresponding to a column in a Results table. For example, A6 would refer to one of six non-unique solutions for the flowpath from Spring 5.29 to R-37-2 S3. The set of numbers in column A6 are phase mole coefficients, or fractions of moles of each mineral phase required to react (per L water) along the flowpath to produce the water chemistry at the endpoint, Screen 3 of regional well R-37-2. Phase mole coefficient is a more specific term for mass transfer coefficient.

Pathways for discrete inverse model experiments are lettered A-L (Table 2a). Simple mixing model experiments are lettered M-P, and exploratory mixing model experiments are lettered Q-U (Table 2b). Complete results tables are shown in Supplementary Materials, part b.

2.3.1 Flow pathways for discrete models

In this inquiry, flow pathways are assumed based on gradient and location of monitoring sites within each hydrostratigraphic unit. For insight into hydrochemical evolution between a recharge zone in upper Cañon de Valle to the regional aquifer, regional flow pathways are conceptualized from a mountain block spring to five different well screens located in the Tschicoma and Puye Formations. Additional sets of flow pathways are assumed within perched intermediate zones of groundwater, using monitoring well screens for both the start and end points (Figure 15). A general assumption is that the bulk of groundwater movement is lateral migration along gently-sloping bedding planes. The general direction of flow is from west to east, which is consistent with regional water level data. As these paths are mostly within discrete rock formations, the results help to identify dominant water-rock interactions. In evaluating results, important considerations are the mineralogy and whole rock chemistry of the unit, and saturation indices of minerals exposed to the fluid (results of Forward Modeling).

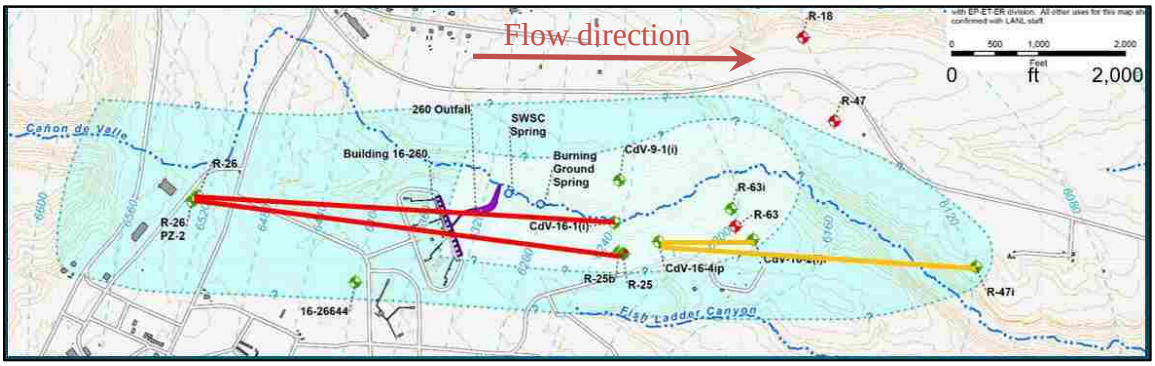

Figure 15: Flowpaths in intermediate groundwater. Red flowpaths are in Otowi Member, yellow are in Puye Formation.

In many cases, reasonable uncertainty limits, below or slightly above 10%, are input to PHREEQC and successfully produce model simulations. Along other flowpaths,

particularly those in shallow intermediate waters, the need to increase uncertainty limits to produce model results may indicate the importance of other factors. These may include the influence of rain or snow, or that mixing between hydrologic compartments is taking place before water enters the endpoint well screen.

A preliminary forward modeling step generates saturation indices for the relevant silicate minerals at the beginning and end of each pathway, based on aggregated water chemistry profiles from each location. The saturation states of mineral phases, along with XRD data on mineral occurrence in these rock formations, guide the input to inverse models.

2.3.2 Phase I mixing models

Mixing between mountain block water and local TA-16 area vadose zone infiltration in intermediate groundwater is explored with sets of models that combine the inverse mass-balance function with a mixing function. These scenarios aim to refine the preliminary inverse models in the upper intermediate water, estimating the contribution of local recharge from the alluvial aquifer below the perennial and ephemeral reaches of the canyon at TA-16. They are intended as an intermediate step from some discrete models that require large uncertainty limits to the subsequent mixing models in deeper groundwater. The purpose of these mixing models is to discover if reasonable mixing ratios between upper intermediate groundwater and springs or alluvial zone water could be modeled with more conservative uncertainty limits. These two items, along with a mass transfer scenario reasonably consistent with the discrete models, would give confidence in the overall approach.

2.3.3 Phase 2 mixing models

Further inverse mixing model runs are designed to explore mixing ratios in deeper screens where the recharge sources are not strongly indicated by the conceptual model. of shallow spring or vadose zone recharge with focused and diffuse mountain block recharge in deeper zones of lower intermediate groundwater, as well as water in regional wells that have had detections of RDX. End-member waters for mixing scenarios are defined by the aggregated chemistry of Spring 5.29 and R-26 Screen 1, as focused and diffuse recharge, respectively. Local recharge end members are defined by Burning Ground Spring, as shallow intermediate zone water, and aggregated alluvial aquifer water.

The results of inverse mixing model experiments are variable, in the sense that some of the proposed models specify unlikely mass-transfer scenarios, not in agreement with solubility indices and mineral abundances. The preferred mixing models are generally in agreement with preferred discrete inverse models, in the sense that mass transfer of each mineral phase should be relatively consistent in scale. Chloride, which is assumed to act as a conservative tracer, is not used as a mass balance constraint in the inverse modeling process; chloride concentrations are projected for all mixing models afterward, which is then used to evaluate the most reasonable models produced by each experiment

Inverse Model Flowpath	Aquifer	Rock Formation	Start point	WL elevation (2016 ft)	End point	WL elevation (2016 ft)	Surface distance (ft)	Elevation change in 2016 (ft)
A	Regional	Tschicoma	Spring 5.29	8557	R-37-2 S3	6132	22304	-2425
B					R-37-2 S4	6132	22304	-2425
C					R-48	6132	18049	-2425
D		Puye			R-63	6190	17844	-2367
E					R-47	6119	20518	-2438
F	Intermediate		CdV 16-4(i)p Screen 1	6611	CdV 16-2(i)r	6623	1068	+12
G					R-47i	6527	3651	-84
H		Cerro Toledo to Otowi	R-26 Screen 1	7034	CdV 16-1(i)	6794	4828	-240
I					R-25b	6758	4911	-276
J		Tshirege	R-26 PZ2	7464	Burning Ground Spring	7436	4057	-28
K					SWSC Spring	7434	3690	-30
L			16-26644	7458.0	Martin Spring	7448.0	2631	-10

Table 2a: Flow pathways used to create discrete inverse models.

Inverse Mixing Model Experiment	Mixing occurring in:	Mixing end members	End point
M	Otowi Member	-R-26 Screen 1 -alluvial aquifer	CdV 16-1(i)
N		-R-26 Screen 1 -alluvial aquifer -16-26644	R-25b
O	Puye Formation	-CdV-16-4(i)p Screen 1 -CdV-16-1(i)	CdV-16-2(i)r
P		-CdV-16-4(i)p Screen 1 -CdV-16-1(i) -alluvial aquifer	R-47i
Q		-5.29 Spring -R-26 Screen 1 -Burning Ground Spring -alluvial aquifer	CdV-16-4(i)p S1
R			CdV-9-1(i)
S		-5.29 Spring -R-26 Screen 1 -Burning Ground Spring -alluvial aquifer -CdV-9-1(i)	CdV-16-4(i)p S2
T		-5.29 Spring -R-26 Screen 1 -Burning Ground Spring -alluvial aquifer	R-63
U			R-18

Table 2b: End-member mixing scenarios for inverse mixing model runs

3.0 Results

3.0 Forward model results

Saturation states observed for individual mineral phases are generally consistent across all aggregated water samples used in this study. Along assumed flow pathways, phases may approach equilibrium, but none are observed to cross equilibrium, which is perhaps normal for relatively dilute mountain water. Complete tables of saturation indices for relevant minerals are shown in Supplementary Materials part a (Tables 10a, b, c, d); distribution of key phases is shown in a histogram below (Figure 16).

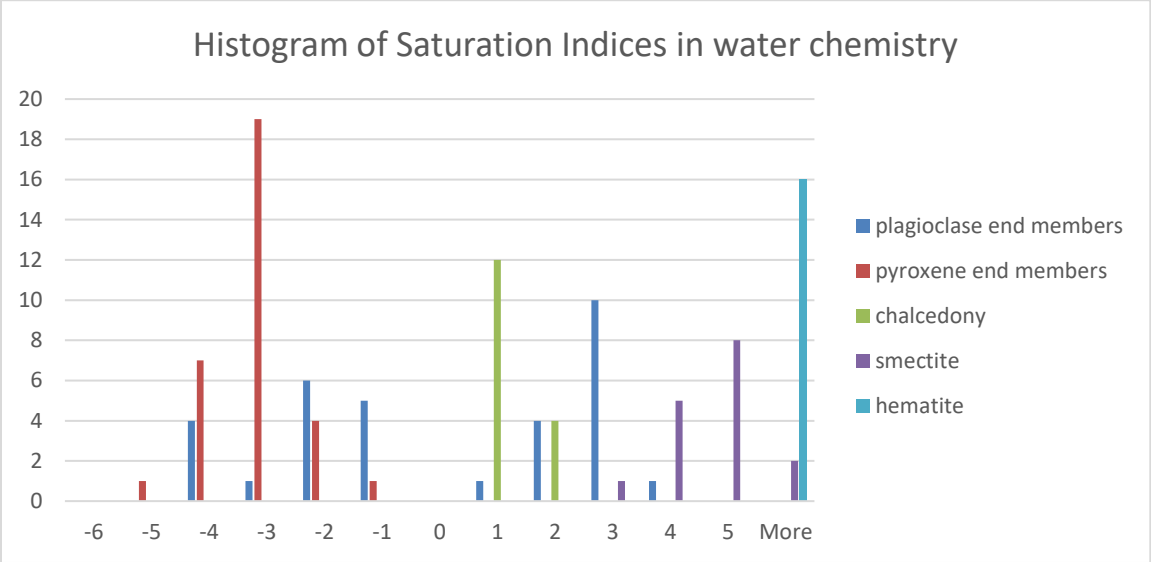

Figure 16: Histogram of Saturation Indices from Forward Model results, for relevant mineral phases

Groundwater remains undersaturated with respect to calcium feldspar (anorthite), though all other feldspar end-members are stable. There is undersaturation with respect to orthopyroxenes (Enstatite, Ferrosilite) and clinopyroxenes (Diopside, Hedenbergite). Crystalline silica minerals are stable, and there is supersaturation with respect to chalcedony; however, amorphous silica is undersaturated. Waters are also undersaturated

with respect to calcite. Saturation indices of iron oxides and clays are positive. Saturation indices for secondary minerals are not, however, necessarily indicative of actual precipitates that would be seen in the system. These results are used to constrain the direction of reactions in inverse modeling, as a way of pre-screening the output. Because inverse modeling is based only in stoichiometry, and not thermodynamics, this step restricts the generation of unrealistic solutions, simplifying evaluation of inverse models.

While it is normal for a saturation index to change somewhat from the beginning to the end of a flowpath, differences of a few units or more across several indices may indicate that the flowpath is not entirely valid consistent with the continuous flowpath assumption; there may be limited hydraulic connection between the points, or mixing may occur (Bowser and Jones, 2002). This is probably the case with the flowpath assumed between R-26 Screen 1, which has chloride of 1.3 mg/L, and CdV-9-1(i), which has chloride of 11.1 mg/L; these points are probably in different hydrostratigraphic units. Their connection is explored in the inverse mixing model for CdV-9-1i, rather than as a discrete model. Well CdV-9-1i may receive some input from the zone where water is characteristically similar to R-26 Screen 1, which the mixing model is intended to capture.

3.1 Inverse model results

The following sections discuss the various nonunique solutions produced by inverse model experiments in PHREEQC, aiming to identify the most favorable model simulations for each assumed flowpath, based on solubility and mineral occurrence in respective rock formations. Consistent mass transfer scenarios are sought across model experiments within each formation; variability among formations is expected to be

explained by different mineral abundance or mixing influences. Positive mass transfer coefficients indicate dissolution, and negative mass transfer coefficients indicate precipitation. The mass transfer coefficients, termed in PHREEQC as “phase mole coefficients”, represent the moles of the particular mineral phase that would have to react, per liter of water, to explain the evolution of water along the flowpath as indicated.

3.1.1 Discrete inverse models

Identification of favorable model simulations is addressed by flowpath group, beginning with regional flowpaths assumed to move within the Tschicoma Formation, followed by regional flowpaths that end in the Puye Formation (Table 2a). There are three of the former and two of the latter, and all five use the same start point, Spring 5.29. Two shorter flowpaths within intermediate water in the Puye Formation, and two flowing from the Cerro Toledo Formation into the Otowi Member, are discussed with respect to their model inputs and results. Three shallow intermediate pathways, ending at springs, are a final group. The flowpaths are alphabetized, and particular model simulations are referred to by the letter together with a number (ex. “L6”), indicating a specific set of mass transfer reactions. For each letter, the simulation determined to best agree with solubility, soluble mineral and precipitate occurrence, is compared with favored simulations for other flowpaths.

Several factors constrain the models generated by PHREEQC, some of which are well illustrated by regional flowpath models. Among the most obvious are acidity, sodium, aluminum, and silica, as described below. The pH of deep groundwater rises along the regional Flowpath A (Table 2a) by nearly one pH unit, from 6.92 to 7.81, requiring a significant consumption of H^+ ions by dissolution reactions. Removal of protons results

from dissolution of both felsic and mafic silicate minerals, as well as silica glass. Precipitation of secondary minerals consumes water molecules and reintroduces protons into solution. However, precipitation does not keep up with dissolution, as much of the mass of cations remain in solution, so overall the pH of dilute waters tends to rise.

Sodium is an important parameter in these models, as it is nearly conserved in solution. A very small amount of Na precipitates in smectite, but otherwise it remains and can be seen as indicating the amount of plagioclase dissolution. In ion exchange reactions within clays, electrostatically bound sodium is typically replaced by calcium or magnesium and pushed into solution (Bowser and Jones, 2002); consequently, aqueous sodium is close to the real amount of sodium associated with mineral dissolution.

The opposite is the case with both aluminum and iron, which have affinity for solid phases and are weakly represented in solution. Though free aluminum can be attributed to both plagioclase and glass dissolution, these phases tend to dissolve incongruently. Mostly, aluminum remains in amorphous solid phases, as aluminous clays are formed in more of a leaching process than as precipitates. However, PHREEQC accounts for aluminum mass transfer from plagioclase and glass, to clay minerals, in the same way as if it were dissolved congruently and reprecipitated.

From dissolution of a glassy phase, stoichiometry is uncertain; there are likely to be various products in trace amounts, including both anions and cations. Some small amount of proton is consumed, and the primary product is dissolved silica, or silicic acid. This silica could potentially precipitate as chalcedony, or perhaps as a microcrystalline opal phase. Chalcedony precipitation occurs without an H^+ byproduct, only the release of

water, so pH is not lowered. Therefore, glass dissolution along the regional flow pathway can explain the pH rise, though it requires an excessive and unlikely mass transfer of silica. This type of model simulation is shown in Figure 17 (A0); a simulation that indicates silica mass transfer of an order of magnitude greater than all other simulations, was generated for each regional flowpath.

3.1.1.1 Regional Groundwater Tschicoma Formation models

Regional flow pathways are conceptualized from the high spring (Spring 5.29) to well screens within the dacite Tschicoma Formation. Model results for Flowpath A, ending at R-37-2 S3, are shown in Figure 18.

Besides the glass-to-silica reaction, there is some mass transfer of pyroxene and feldspar to smectite. This model might describe a rock formation where glass greatly exceeds all other soluble minerals and CO_2 gas is all but absent. The likelihood that glass dissolution is such an outsized mechanism for pH change in this system seems low, considering that it would have to exceed plagioclase dissolution by a factor of ten. Even though glass solubility exceeds plagioclase solubility, the latter is dominant in the R-37-2 XRD data; also, for this model to be realistic chalcedony or opal would need to exceed iron oxides and clays in the data, which it does not. For each regional flowpath, one such outlier model is removed (as in Figure 18). Other processes may then be better represented, as the rise in pH is more realistically attributed to dissolution of glass alongside other silicates and possibly calcite.

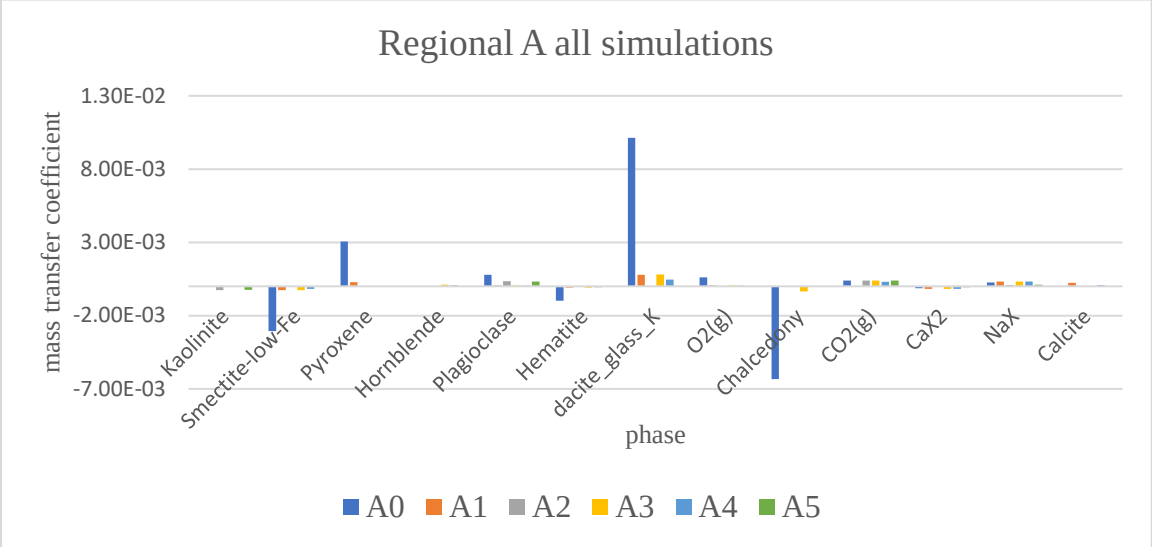

Figure 17: All inverse model results for regional Flowpath 1a, set at 7.5% uncertainty

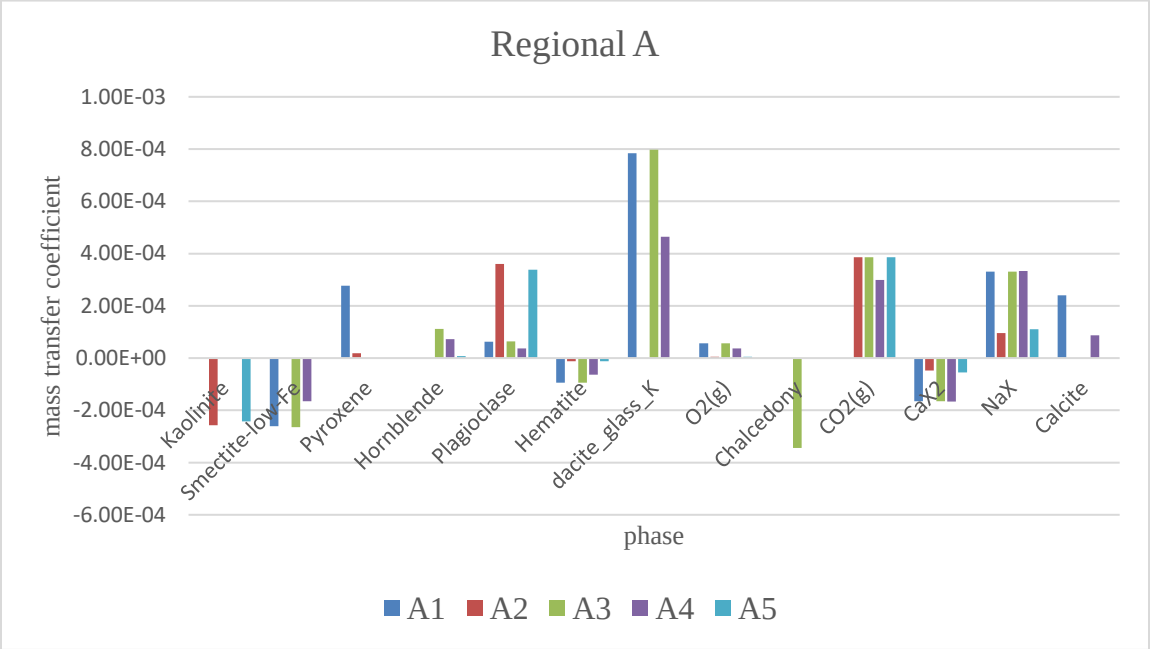

Figure 18: Regional Flowpath A inverse model results with outlier removed, set at 9.5% uncertainty.

In the following sections, observations of model outputs are discussed in order to better understand how PHREEQC reveals possible chemical reaction pathways to generate inverse model solutions. The program appears to choose between precipitating kaolinite or smectite. In very few of the models produced for this study did the program combine pyroxene and hornblende dissolution, though both mafic phases were usually available. A bimodality is apparent in these results, in the sense that enhanced plagioclase dissolution associates with kaolinite and less ion exchange (Series A2, A5). In three models, glass dissolution is associated with both smectite and hematite precipitation, and a greater degree of ion exchange (Series A1, A3, A4). Among these, one indicates chalcedony precipitation and CO_2 dissolution, while the others dissolve calcite. Calcite is not a component of dacite; however, this water may be exposed to pedogenic calcite in surface soils or rock fractures (Newman et al., 1997). Series A4 combines a small amount of calcite dissolution, smectite and minor hematite precipitation, dissolved CO2 and a small amount of dissolved oxygen, and ion exchange. It indicates a smaller degree of plagioclase dissolution, which seems appropriate considering that the true saturation state of the plagioclase composition could be close to equilibrium. It is likely that mafic components are derived by a combination of pyroxene and amphibole not articulated here – and that pyroxene, rather than hornblende, is the principal donor of iron and magnesium.

In XRD analyses of sediments from this well (R-37-2), a siltstone layer between lavas above Screen 3 (just below Screen 2) has over 43 wt% smectite, and less than 1% kaolinite, and no opal or chalcedony (LANL ER2002-0557). Glass is present in two

samples from the overlying Puye Formation at 5% and 12%, and in dacite clasts at 33.7%; though in none of these sediments are there clays. Also, in the clay-rich siltstone there is no glass, which suggests that glass dissolution and smectite precipitation are important processes in this zone. The siltstone also has about 1-1.5% clinoptilolite, a zeolite alteration product not present in the Puye samples. In the model results, water in Screen 3 of R-37-2 is supersaturated with respect to hydrous clinoptilolites. Both plagioclase and alkali feldspar are present in the underlying siltstone at roughly half the weight percentage as in the overlying Puye sediment, suggesting that plagioclase dissolution is another, though perhaps minor, aspect of weathering in this zone. Because no secondary silica phase is indicated by the data, Series A3, with dominant chalcedony precipitation, is not preferred. Rather, based on the above observations, Series A4 would appear to most accurately express the alteration processes in the Tschicoma Formation regional groundwater. Dissolution of dacitic glass, in this particular case, appears to be related to dominant smectite and minor kaolinite or hematite. For each regional flowpath, models that include CO_2 are preferable to models dissolving calcite and not CO_2. These models support glass as the dominant dissolving phase in the Tschicoma Formation, with smectite as the dominant secondary phase. At Spring 5.0, issuing from dacite bedrock in upper Cañon de Valle, rocks in every stage of this weathering process can be observed, including unweathered surfaces, surface leaching exposing weathered phenocrysts of plagioclase, friable weathered matrix, and orange smectite clays. Cloudy white clays, which would indicate kaolinite, have not been observed during spring and summer flow gauging activities.

Of the simulations for Flowpath B, starting at Spring 5.29 and ending at Screen 4 in the same well (R-37-2), none dissolve similarly small amounts of plagioclase unless glass dissolution or kaolinite precipitation is excessive. Model B10 dissolves dacite glass and precipitates dominant smectite with mass transfers similar to A4. Calcite dissolution is also similar to A4 (Figure 19).

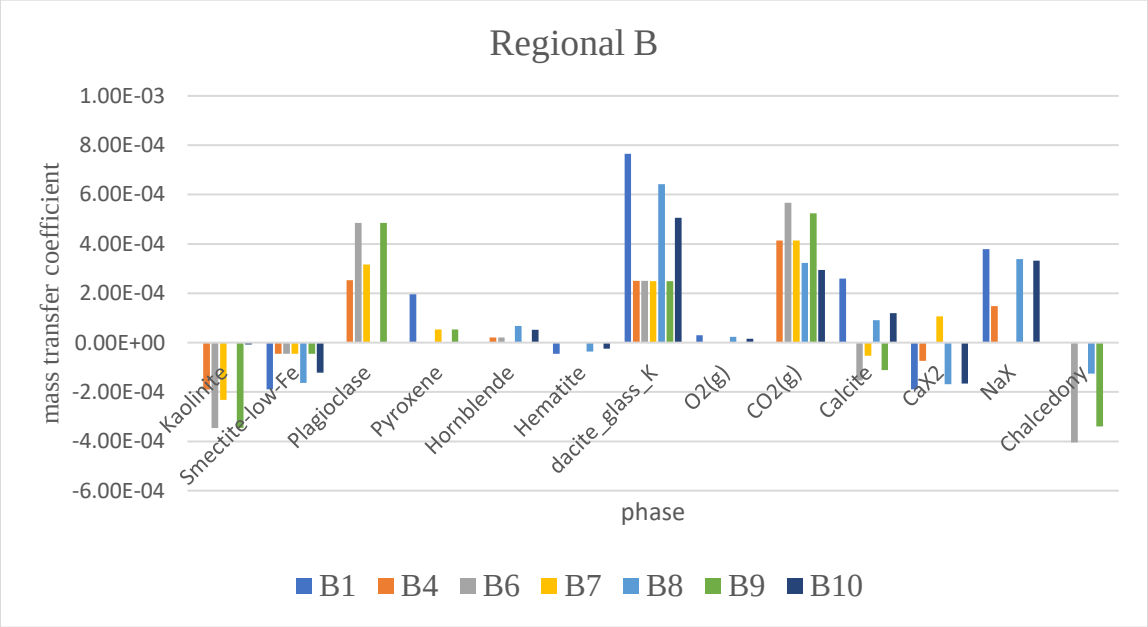

Figure 19: Regional Flowpath B inverse model results with outliers removed, set at 9.5% uncertainty.

Of the models for flowpath C, also entirely within the Tschicoma Formation, those that precipitate both types of clays are not considered representative because kaolinite is dominant and glass is not dissolved. Two of the others dissolve calcite; the one that also dissolves CO_2 is favored and is consistent with the models chosen for the flowpaths discussed above. Table 3 summarizes mass transfers for the favored Tschicoma Formation flowpath models.

Inverse model	Plagioclase	Smectite	Dacite Glass	Hematite	Calcite
A4	3.73 e-5	-1.65 e-4	4.65 e-4	-6.35 e-5	8.70 e-5
B10	---	-1.22 e-4	5.06 e-4	-2.39 e-5	1.19 e-4
C2	3.13 e-5	-1.20 e-4	2.79 e-4	-5.14 e-5	1.53 e-4

Table 3: Comparison of mass transfer between selected models for regional Tschicoma Formation flowpaths.

3.1.1.2 Regional Groundwater Puye Formation models

Two regional flowpaths (Flowpaths D and E) begin at upper canyon Spring 5.29 and terminate in the Puye Formation. Flowpath D ends at well R-63 (Figure 20); along this flowpath the rise in pH is smaller than those ending in the dacite formation, closer to a half pH unit. In a general sense, this might indicate that regional groundwater recovers some acidity in the Puye Formation, possibly through precipitation of clays in pore space. It could also indicate dilution of evolved regional groundwater with younger water at the top of the water table. Biotite is added as a phase, as it is a potential contributor of potassium to solution, and appears in the Puye Formation at R-25 (LANL ER2001-0697). The effect may be negligible; in simulation D5 it enables a model where pyroxene, plagioclase and glass dissolve in nearly equal proportion, and where secondary minerals are dominantly smectite and lesser hematite, enhanced respectively by potassium and iron from the biotite. A similar model, D1, has a smaller amount of glass dissolution, nearly equal amounts of plagioclase and hornblende dissolution, and smectite and hematite precipitation. Simulation D3 has less dissolution of pyroxene and plagioclase, but more glass dissolution, and calcite dissolution as well. Other models from this flowpath

combine plagioclase and CO_2 dissolution, smectite and kaolinite precipitation, and do not dissolve glass or calcite. It is worth noting that chalcedony precipitation was not employed by any of the models in this run, nor was it used in the R-47 model run.

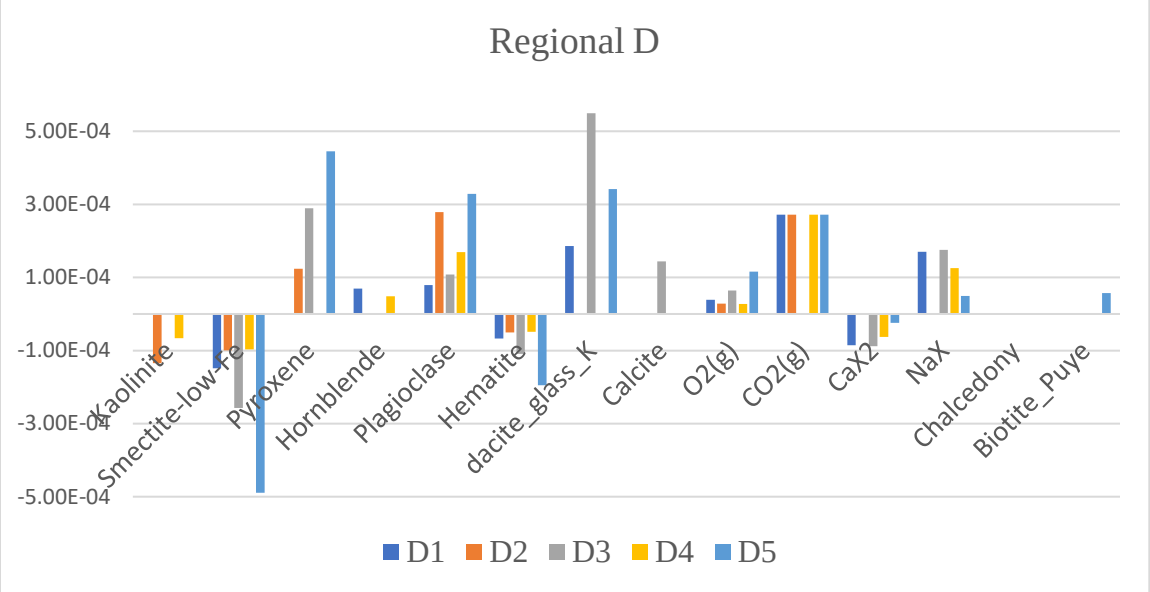

Figure 20: Inverse model results for flowpath connecting Spring 5.29 and R-63, set at 7% uncertainty.

As XRD data are available from nearby R-25, they are used to evaluate model results for the flowpath to R-63. In upper Puye samples, glass is present on the order of 10 to 20 weight percent. Feldspar makes up between 50 and 70 weight percent. There is between 0 and 3% smectite, no kaolinite, and no opal-CT below the Otowi Member. There is about 1% hematite (LANL ER2001-0697). Among the simulations, D1 (Figure 19) best expresses the mass transfer trends as observed at R-25, because it precipitates the least amounts of secondary minerals from among the models that dissolve glass and do not precipitate kaolinite. If calcite were available, it would accelerate silicate dissolution and

smectite and hematite precipitation, as in Series D3. Neither of the preferred models for Flowpaths D or E rely on calcite presence. Of the models for Flowpath E, values for glass and smectite mass transfer, consistent with D1, guide the selection of E3, which has similar mass transfer of plagioclase and hematite. Compared to the models chosen for regional Tschicoma Formation flowpaths, these appear to dissolve slightly less glass and slightly more plagioclase. Table 4 summarizes favored models for regional flowpaths ending in the Puye.

Inverse Model	**Plagioclase**	**Smectite**	**Dacite Glass**	**Hematite**	**Calcite**
D1	7.89 e-5	-1.49 e-4	1.86 e-4	-6.75 e-5	---
E3	7.43 e-5	-1.70 e-4	3.10 e-4	-7.39 e-5	---

Table 4: Comparison of mass transfer between selected models for regional Puye Formation flowpaths.

3.1.1.3 Intermediate Groundwater Puye Formation models

Inverse Flowpaths F and G connect beginning and end points in a saturated intermediate groundwater zone entirely within the Puye Formation and above the regional groundwater table. Flowpath F is the shortest segment considered, with start and end points little more than 1,000 feet apart, and virtually no change in pH. Calcium, magnesium, and potassium each decrease slightly, while sodium and bicarbonate both increase. Variation in the model results is slight. In three of the four, mass is transferred from plagioclase and pyroxene to smectite, without kaolinite but with some hematite. This is generally consistent with Puye Formation XRD data from R-25 (LANL ER2001-0697). The data also suggest that some glass is also available to dissolve, which is not

reflected in the model. The increase in sodium of 2.7 mg/L, explained by plagioclase dissolution, ion exchange and smectite precipitation, seems to constrain the models narrowly. Series F1, F2 and F3 are nearly identical; the preferred model is Series F1 (Figure 21), which has plagioclase and pyroxene, though no calcite, dissolving.

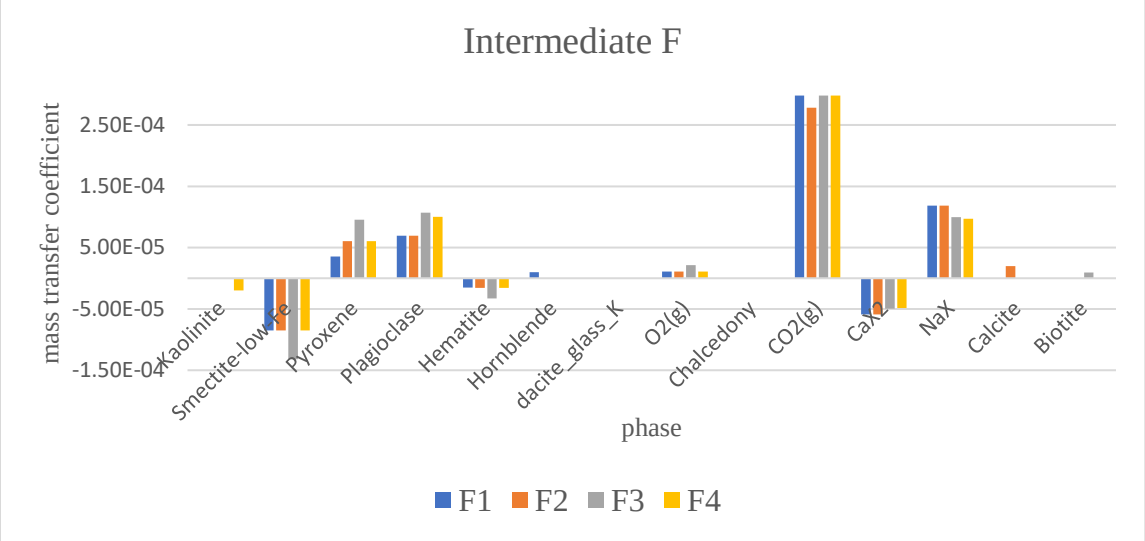

Figure 21: Inverse model results for flowpath connecting 16-4(i)p Screen1 and 16-2(i)r, set at 3.6% uncertainty

In each case, the mass transfer coefficient for plagioclase is 6.96 e-5. Flowpath G shares the start point with F, but the pathway is 3650 feet, approximately 3.65 times as long.

(6.96 e-5) * (3.65) = 2.5 e-4

This suggests the scale of mass transfer for plagioclase dissolution along flowpath G should be on the order of 2.5 e-4 moles/L.

Along flowpath G (Figure 22), pH actually goes down by 0.16 units. Again, Ca, Mg and K decrease slightly, though Na increases by 7.4 mg/L. PHREEQC again derives this amount of sodium from plagioclase dissolution and ion exchange. There is a pattern of

calcite dissolution with more ion exchange and less plagioclase dissolution (Series G2, G4), or no calcite, less ion exchange and more plagioclase dissolution, with chalcedony precipitation (Series G1, G3,5,6). To meet the projection of plagioclase dissolution from Flowpath F, one of the latter type would be appropriate; the former type have less mass transfer of plagioclase than in the shorter F models. Again, since no kaolinite is observed, and limited smectite and hematite are, G6 is preferred. It is interesting to note that most of the simulations indicate precipitation of opal would occur; the two simulations that do not precipitate opal seem to rely on dissolution of large amounts of calcite. Though model G1 hits the plagioclase dissolution target almost exactly (2.4 e-4), it indicates kaolinite precipitation that is not observed. Series G6 has mass transfer of plagioclase at 1.23 e-4, which is reasonable, if only half of the target. Overall there are similarities between Series G6 and F1; however, the difference lies in chalcedony, or perhaps opal-CT, precipitation along the flowpath to R-47i, which would pass below the Cañon de Valle channel. Table 5 compares the regional Puye models shown in Table 4 with these intermediate Puye models.

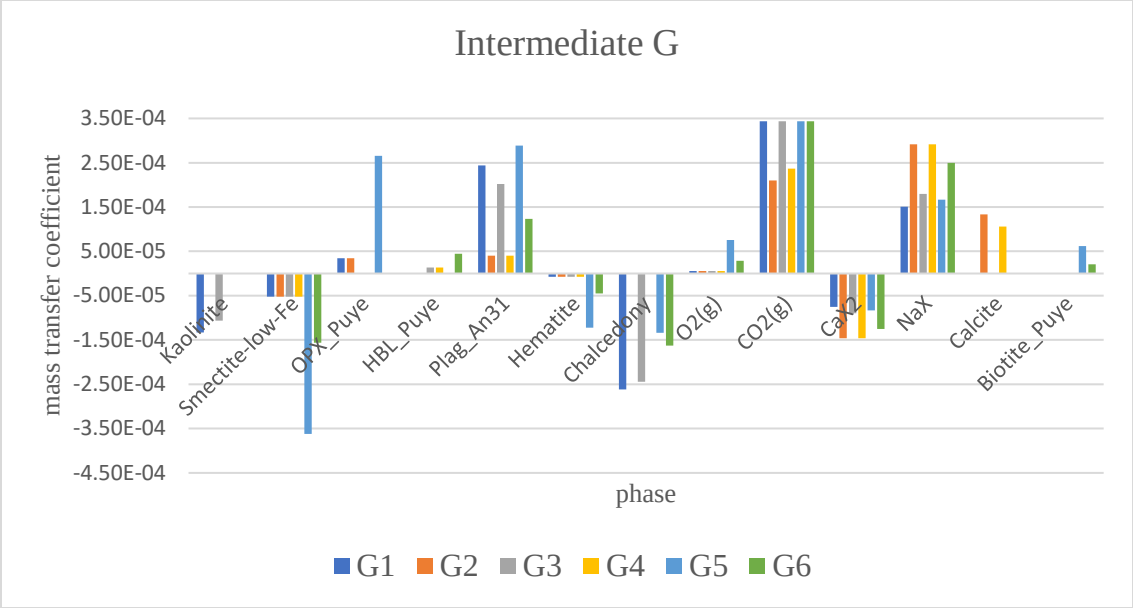

Figure 22: Inverse model results for flowpath connecting 16-4(i)p and R-47i, set at 3.5% uncertainty.

Inverse model	Plagioclase	Smectite	Dacite Glass	Hematite	Chalcedony
D1	7.89 e-5	-1.49 e-4	1.86 e-4	-6.75 e-5	---
E3	7.43 e-5	-1.70 e-4	3.10 e-4	-7.39 e-5	---
F1	6.96 e-5	-8.53 e-5	---	-1.53 e-5	---
G6	1.23 e-4	-1.56 e-4	---	-4.51 e-5	-1.63 e-4

Table 5: Comparison of mass transfer coefficients for selected regional and intermediate Puye models.

3.1.1.4 Intermediate Groundwater Bandelier Tuff models

3.2.1.4.1 Otowi Member and Cerro Toledo Formation

High percentages of glass in well R-25 are coincident with opal-CT, a type of hydrated, amorphous silica. In QXRD analysis, three of the samples are from the Cerro Toledo, two from the Otowi and one from the Guaje pumice bed. Except for one feldspar rich sample

in the Cerro Toledo, they are all between about 52% and 98% glass. In the 52% glass sample (568 ft depth), the analysis shows about 8% opal-CT (LANL ER2001-0697). Likewise, in the lowest cooling unit of the overlying Tshirege Member, Qbt1g, 49% glass is associated with 7% opal-CT. Also, in two samples of the other glassy cooling unit of the Tshirege, Qbt4, glass at 67% and 29% is associated with opal-CT at 2% and 6%, respectively. Though other samples from R-25 have various amounts of glass, none have opal-CT, which may be a function of low permeability or little exposure to groundwater. Overall, these data suggest that glass is a dominant weathering phase. The actual crystallography of the secondary phase is outside the scope of this study, though chalcedony appears, by saturation indices, to be viable as a solid phase outlet for dissolved SiO_2. It is used as a proxy for opal-CT.

Above the Puye Formation, intermediate flowpaths are assumed between R-26 screen 1, situated in the Cerro Toledo Formation, and two wells in the underlying Otowi Member to the east, 16-1(i) and R-25b. These flowpaths would pass through vitric rock material, which is unaffected by vapor phase alteration, the slow-cooling process that results in the crystal silica phases tridymite and cristobalite. In the QXRD analysis, these are present everywhere in the Bandelier Tuff where glass is absent, including in the feldspar-rich sample in the Cerro Toledo. They are also absent where glass is present. Reactive, unaltered glass, in pyroclastic rocks such as pumice, is generally more permeable than altered material, in which pumice lapilli are coated and filled by devitrification products. Mass transfers for the CdV-16-1(i) flowpath (H) are shown in Figure 23.

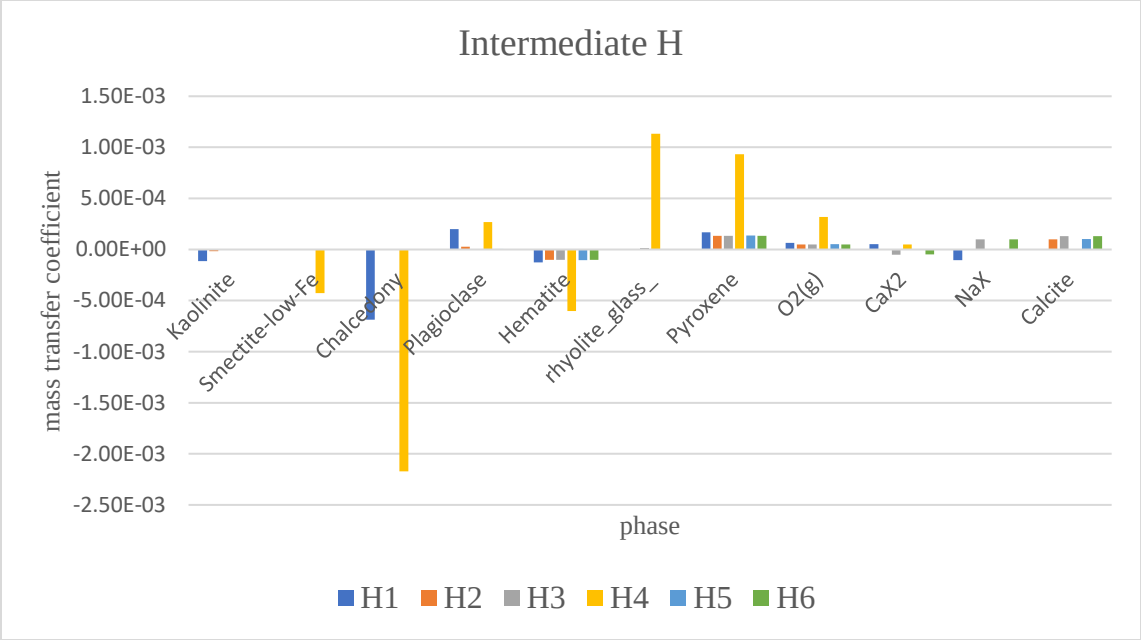

Figure 23: Inverse model results for flowpath connecting R-26 Screen 1 with 16-1(i), set at 15% uncertainty.

The aggregated water in 16-1(i), in the Otowi Member below Cañon de Valle, shows some indication of mixing with alluvial infiltration, as both Cl^- and SO_4^- concentrations rise. Bicarbonate increases by 10 mg/L, and TDS rises by over 40 mg/L. A slight drop in pH may explain why none of the models dissolve CO_2 gas, as dissolution is pushed by protons that are already in solution. Along this 4800+ ft flowpath, cations generally increase, which may also be partly due to input from a shallower intermediate zone. However, the presence of soluble glass in both the Otowi and Cerro Toledo suggests that the overall pattern of reactions described by simulation H4 is generally valid, if not necessarily at the scale indicated in the plot. This model precipitates smectite clay and dissolves rhyolitic glass; other models here dissolve little to no glass, so they are not considered valid.

Along Flowpath I (Figure 24), from R-26 Screen 1 to well R-25b, bicarbonate increases by 25 mg/L, and TDS increases by 20 mg/L. Among other parameters, the most noticeable changes are a 9 mg/L increase in sodium, and that dissolved silica decreases slightly. Though the geochemical models generated for this flowpath required a 19% uncertainty limit, it is worth noting the similarity between the prominent model here and at CdV-16-1(i), and the pattern of reactions in both: dominant glass dissolution on the order of 1.0 e-3 moles/L, pyroxene, plagioclase and oxygen also consumed, and a secondary silica product with smaller amounts of clay and iron oxide.

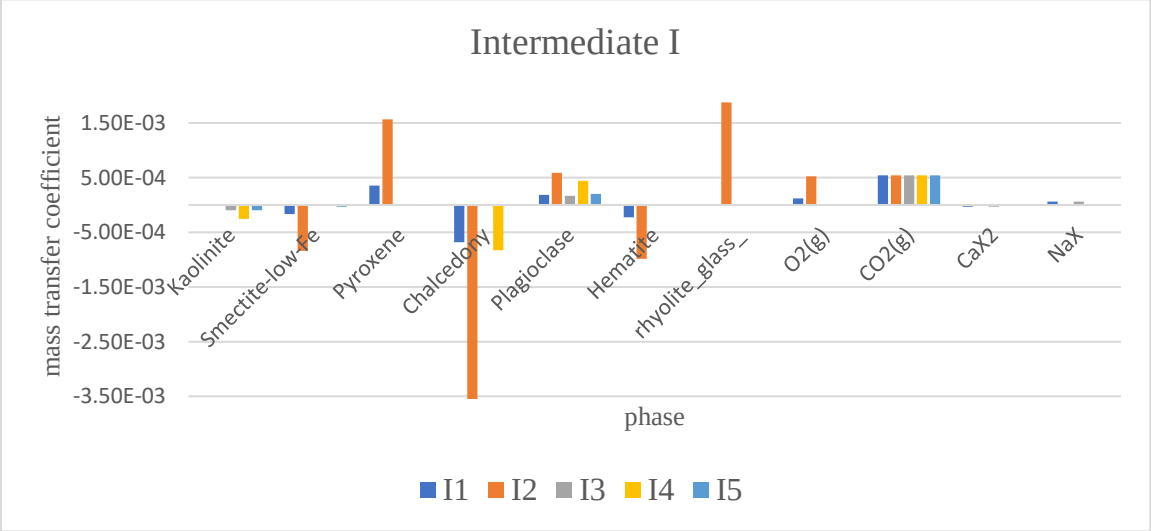

Figure 24: Inverse model results for flowpath connecting R-26 Screen 1 with R-25b, set at 19% uncertainty.

Due to the higher uncertainty limits of 15% and 19%, and in an effort to gauge the input of alluvial groundwater to the upper intermediate groundwater, both of these model runs are improved by adding mixing with vadose zone water in a later section on Phase I mixing models. Preferred mass transfer coefficients are recorded from those model results, which have smaller uncertainty limits.

3.1.1.4.2 Shallow intermediate and spring water

Successful inverse models for Flowpaths J and K, including models with mixing of various dilute spring or precipitation waters, proved difficult to create without uncertainty limits of 25% or greater. Because SWSC and Burning Ground Springs are the source and westernmost point of the alluvial aquifer at TA-16, alluvial groundwater was not considered as a component in mixing along pathways ending at these springs. The aim of discrete inverse models in this section is to reveal something about chemical processes that are active along the flow pathways, as far as perched water residing in fractured, welded tuff.

At 35% uncertainty, eight models were generated for the pathway to Burning Ground Spring, five of which indicate glass dissolution. Since glass is not observed in the Tshirege unit Qbt3t, the unit from which this spring discharges, these are not preferred models; influence of diffuse infiltration through the glassy overlying Qbt4 tuff would probably not be sufficient to dominate the chemistry by dissolving glass, as in Series J1, J3, J4 and J5. Some plagioclase and pyroxene dissolution is expected, with smectite resulting as in Series 4. However, these results are not considered necessarily valid or particularly useful because of the high uncertainty limit. Average chloride nearly triples between R-26 PZ2 and Burning Ground, indicating that this may not be valid as a discrete flowpath. Surface conditions unrelated to water-rock interactions are perhaps not represented in the data sufficiently for these analyses to be successful. Nonetheless, simulation J2 in the plot below (Figure 25) represents a set of reactions that is reasonably consistent with observed soluble and secondary minerals. The mass transfer coefficient for plagioclase and smectite, 9.2 e-5 and -7.0 e-5, are consistent with Puye Formation

flowpaths and more conservative than the values that appear in the Otowi models. Several attempts to create inverse models using SWSC Spring as an endpoint were unsuccessful, for reasons that are unclear. Without a mixing influence of surface infiltration, it is unclear whether these models should run at all with reasonably small uncertainty limits. Flowpath J (and unsuccessful Flowpath K) models seem to illustrate that some important influence, which could be related to the 260 Outfall water, is not captured here.

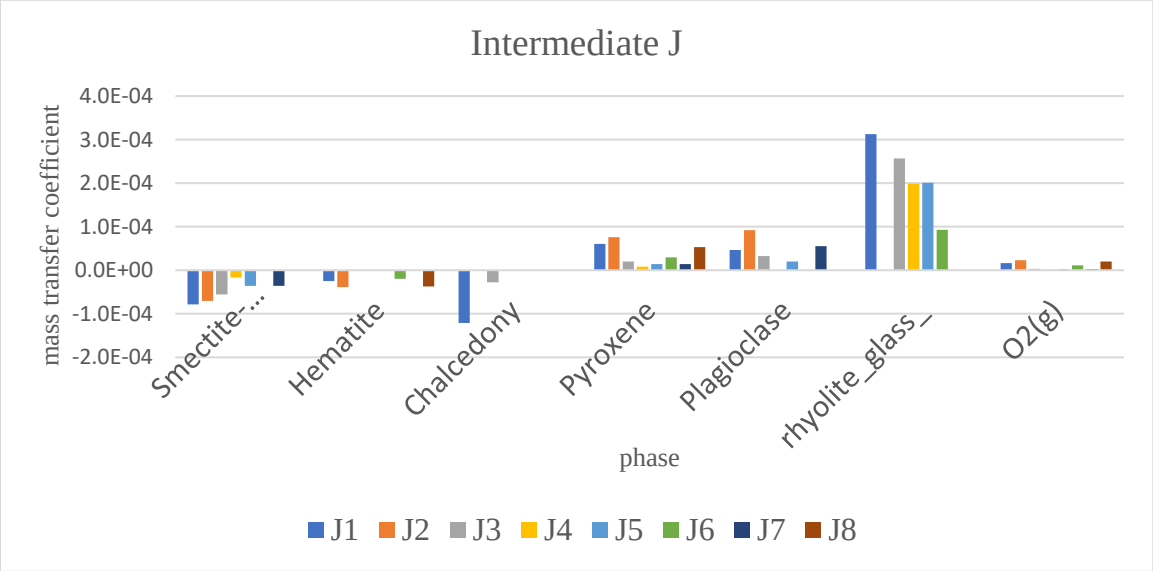

Figure 25: Inverse model results for flowpath connecting R-26 PZ2 and Burning Ground Spring, set at 35% uncertainty.

Martin Spring water chemistry contrasts with that of both Burning Ground and SWSC Springs, in several ways that hint at the different influences of cooling unit Qbt4, from which Martin Spring discharges, and Qbt3t, the underlying welded tuff unit from which the springs in Cañon de Valle emerge. At Burning Ground and SWSC, average chloride and calcium are below 20 mg/L, and bicarbonate is around 65 mg/L. Martin Spring has

Ca close to 30 mg/L, Cl at almost 25 mg/L, and HCO_3^- at almost 100 mg/L. Martin Spring water has almost twice the sodium as in other springs, and though it has the highest total dissolved solids (TDS) of any aggregate water in this study, it has dissolved silica concentrations lower than almost any intermediate or regional groundwater. Because glass is present in Qbt4, and not in Qbt3t, the strong bicarbonate without excessive silica suggests active dissolution and reprecipitation of an amorphous or microcrystalline phase such as opal.

As described previously, two of three Qbt4 samples in the R-25 QXRD data are glassy: in a partially welded caprock at a depth of 5 ft, approximately 67% glass occurs with 2% opal-CT, while at 30.5 ft depth, 29% glass occurs with about 6% opal-CT. The latter and more devitrified of the two is in a more permeable zone of nonwelded tuff. The third Qbt4 sample, at 59 ft depth, has feldspar, quartz, tridymite and cristobalite, but no glass or opal-CT; the base of the unit, it appears, has undergone vapor phase alteration. Traces of smectite, but no kaolinite, are noted for the lower two samples, and the 30.5 ft depth sample has about 1% hematite (LANL ER2001-0697). The flowpath between shallow intermediate well 16-26644 and Martin Spring yields several models using a reasonable uncertainty limit of 7% (Figure 26). Among them, one minimal model agrees both with the above mineralogical data and saturation indices: it has dissolution of a limited amount of plagioclase but greater amounts of pyroxene and glass (2.6 e-3 and 3.6 e-3, respectively), and the chalcedony (opal-CT) precipitation exceeds smectite and hematite by about 5 to 1. This singular model, which describes reactions along a potentially short-residence time pathway, is consistent with groundwater residing in vitric, high surface area-to-volume surge beds. Because no alluvial aquifer is present overlying the pathway,

it is reasonable that the models run at 7% uncertainty without mixing. The halogens Cl^- and F^- increasing in solution as volcanic glasses are dissolved, as documented by White (1980) and others could explain the increase in chloride.

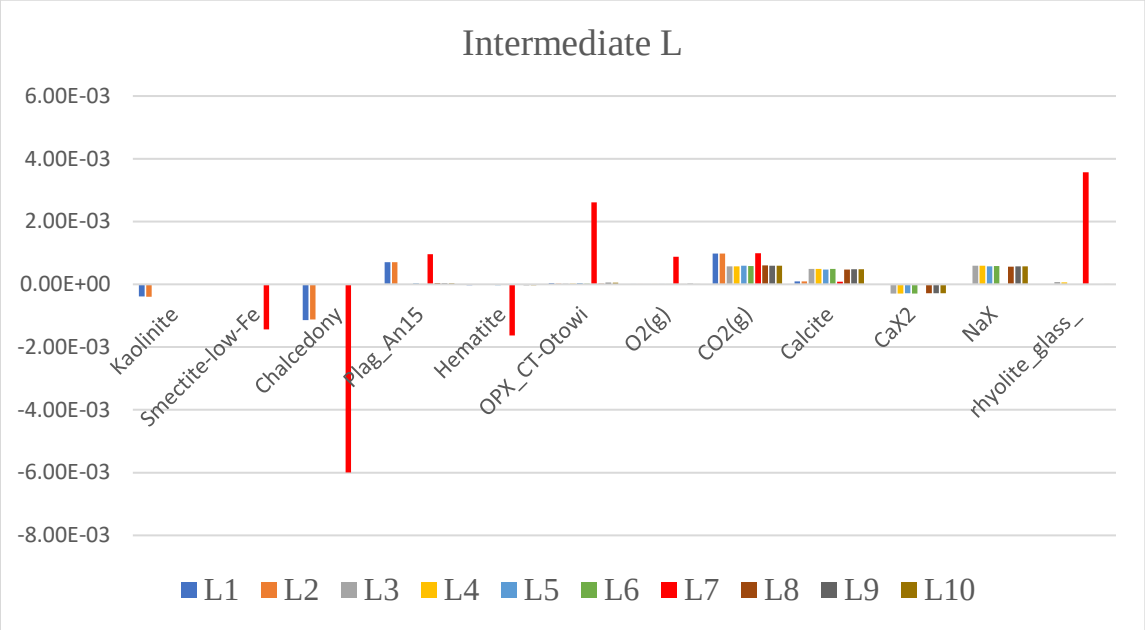

Figure 26: Inverse model results for a flowpath from 16-26644 to Martin Spring, set at 7% uncertainty.

Inverse model	Plagioclase	Smectite	Rhyolite Glass	Hematite	Calcite	Chalcedony
L9	9.58 e-4	-1.44 e-3	3.57 e-3	-1.64 e-3	8.14 e-5	-6.0 e-3

Table 7: Martin Spring flowpath inverse model mass transfer.

Martin Spring water is not used as an end member in mixing models in this study; however, this model and the related data for Qbt4 are presented as a means of validating the similar results of models for the glassy Otowi section of the Bandelier Tuff. Recalling that glass solubility can exceed that of anorthite by one to two orders of magnitude, it is reasonable to accept this model if glass composes 30% to 60% of the rock formation.

3.1.1.5 Uncertainty in discrete inverse models

Managing uncertainty in geochemical models can be critical to bringing out informative results. In PHREEQC, constraints placed by any particular parameter can be loosened with the "-balances" command. For this study, sulfate was initially problematic, in the sense that it is not present in any rock formation as a primary phase, such as pyrite, nor do saturation indices suggest that it precipitates in a secondary phase, such as gypsum. There is variability of sulfate in the data, probably as a consequence of mechanisms other than solid phase/aqueous phase flux. It is present as atmospheric sulfur incorporated in recharge, which may complex or adsorb to sediments. Because oxygen gas is a mass balance constraint, PHREEQC seeks solutions involving sulfate reactions. It is retained in the data for modeling in order to charge balance waters, but if considered with the same resolution as other parameters, it restricts models unless an unlikely phase is specified as a sink or source of sulfur. As a non-conservative ion and a non-silicate, it reveals little, and was eliminated as a factor by putting its uncertainty at 2.0 or above, as necessary.

Overall uncertainty can be useful as an indicator of how valid assumptions are, and possibly as a tool to calibrate models. For any inverse model run, the number of models generated can be manipulated somewhat by a user-specified uncertainty limit; an uncertainty limit of 0.04, for example, adds or subtracts 4% of any parameter, as necessary, adding flexibility to inverse modeling and thereby generating additional models. Trial-and-error was used to find the best range of uncertainty, yielding a manageable number of model solutions. In some cases, a small uncertainty gives an error related to inability of the program to converge. Too large an uncertainty limit tends to give minimal model results excluding phases that are likely to react.

The long, regional flowpath models in this paper were produced with uncertainty of around 9%, which is acceptable considering their conceptual nature, and the heterogeneous and unknown geology of the mountain block. The short intermediate models within the upper Puye Formation were produced with uncertainty of about 3.6%, which seems reasonable and consistent with the idea that flow is anisotropic along beds of cobble, gravel, sand and clay, and there lack clear indicators of mixing, within the upper intermediate zone and along relatively short flowpaths.

In the Otowi it seems likely, based on tritium and chloride observations, as well as fractures observed during well drilling, that mixing occurs. The six models in H were generated with 16% uncertainty. Below that, the run either produces zero models or fails to converge to a numerical solution. In modeling flowpath I, a 19% uncertainty limit was required. In the shallower Tshirege zone, the uncertainty limits for some discrete inverse models can go to 25% or more. At 35%, a wider array of results is generated, some of which tend to explain the change in water chemistry with fewer reactions than would be expected. These can be thought of as short circuiting the processes indicated by saturation states, and are not considered valid.

Tritium in the shallow zone is variable over time, with an overall downward trend corresponding to tritium decay. This, as well as isotopic evidence (LANL 2003, 077965), suggests that slow, laterally-moving baseflow receives input from the surface during individual rain and snowmelt events. This influence may explain the requirement for a greater uncertainty limit in the shallow perched zone. The effects of mixing are explored in the following sections.

3.1.2 Mixing model results

Mixing model experiments are divided into two groups; in the first, Phase I models are designed to improve discrete flowpath model results by introducing an assumption of mixing, as informed by the conceptual hydrologic model. The addition of some alluvial zone water to the upper intermediate zone, for instance, can be reasonably assumed from the observation that surface flow is lost in certain places, probably to discontinuities in the vadose zone. The addition of shallow perched intermediate water to the upper intermediate zone is explored as a possibility as well, expected where well screens are perhaps poorly connected to streambed saturation. In Phase II, mixing in deeper intermediate and regional well screens is explored differently, without making flowpath assumptions. Rather, end member waters that are characteristic of mountain block recharge, in both the Puye Formation and the Otowi Member, and local recharge are input as potential end-members.

3.1.2.1 Phase I mixing models

Two Phase I mixing experiments estimate the input of alluvial water and shallow intermediate zone water to the upper intermediate zone. Another two Phase I mixing experiments attempt to gauge mixing within the upper intermediate zone.

3.1.2.1.1 Mixing between mountain block recharge, alluvial and shallow intermediate water

The inverse model described above for Flowpath H is expanded to include mixing with alluvial groundwater input, as a way to both estimate the amount of shallow groundwater that may percolate through the vadose zone to the top of intermediate water, as well as to improve upon the uncertainty in the discrete inverse Otowi model. Mass transfer results are screened to agree generally with the pattern of dissolution and precipitation in the Bandelier Tuff, as established in the previous section. The preferred model is chosen by considering chloride as a conservative tracer; reasonable models are expected to have minimal chloride mass balance errors between the average and projected chloride. As chloride does not interact in mineral phases or precipitates, it is not a mass balance constraint in the modeling process, and can be used as an independent check on model results.

Alluvial aquifer water is mixed in inverse model experiments with R-26 Screen 1 water, representing mountain block recharge, on flowpaths ending at CdV-16-1(i) and R-25b, respectively. In the first case (Experiment M), 4 similar models were produced with 2.5% uncertainty, with alluvial water making up between 17% and 19% of the end water composition. However, of these, none are considered preferred models; only one dissolves glass, and all four appear to have secondary silica resulting mainly from pyroxene dissolution. Run again with 12% uncertainty, a wider array of solutions results, including several unlikely mixtures not in agreement with saturation indices. Three models are singled out as potentially realistic; these are shown in Figure 27 below.

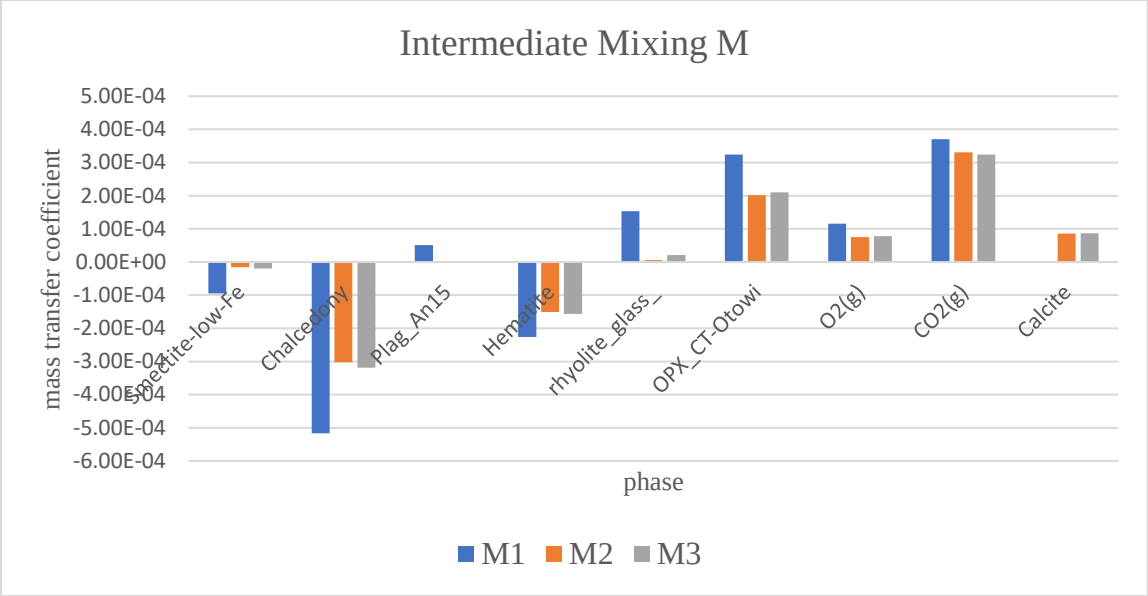

Figure 27: Mixing inverse models in Otowi Member, flowpath ending at CdV-16-1(i). Alluvial aquifer water represents 25% in Series M1, 17% in Series M2, and 18% in Series M3.

Parameters that are not participants in model reactions are not evaluated as mass balance constraints in inverse mixing, so the results given above are evaluated using chloride as a conservative tracer, by estimating a chloride mass balance error as follows:

alluvial Cl^-	23.3 mg/L * (0.25) = 5.825	23.3 mg/L * (0.17) = 3.961
R-26 S1 Cl^-	+ 1.3 mg/L * (0.75) = 0.975	+ 1.3 mg/L * (0.83) = 1.079
Projected Cl^-	25% alluvial: 6.8 mg/L	17% alluvial: 5.04 mg/L

Chloride in CdV-16-1(i) averages 6.7 mg/L, which supports the model result with 25% input of alluvial water to the upper intermediate zone in the Otowi Member (Figure 28). Simulation M1 has a 0.1 mg/L mass balance error. The 25% mixture also helps explain why there is tritium in CdV-16-1(i), where in R-26 Screen 1 there was none

5%

(www.intellusnm.com); the alluvial water has tritium.

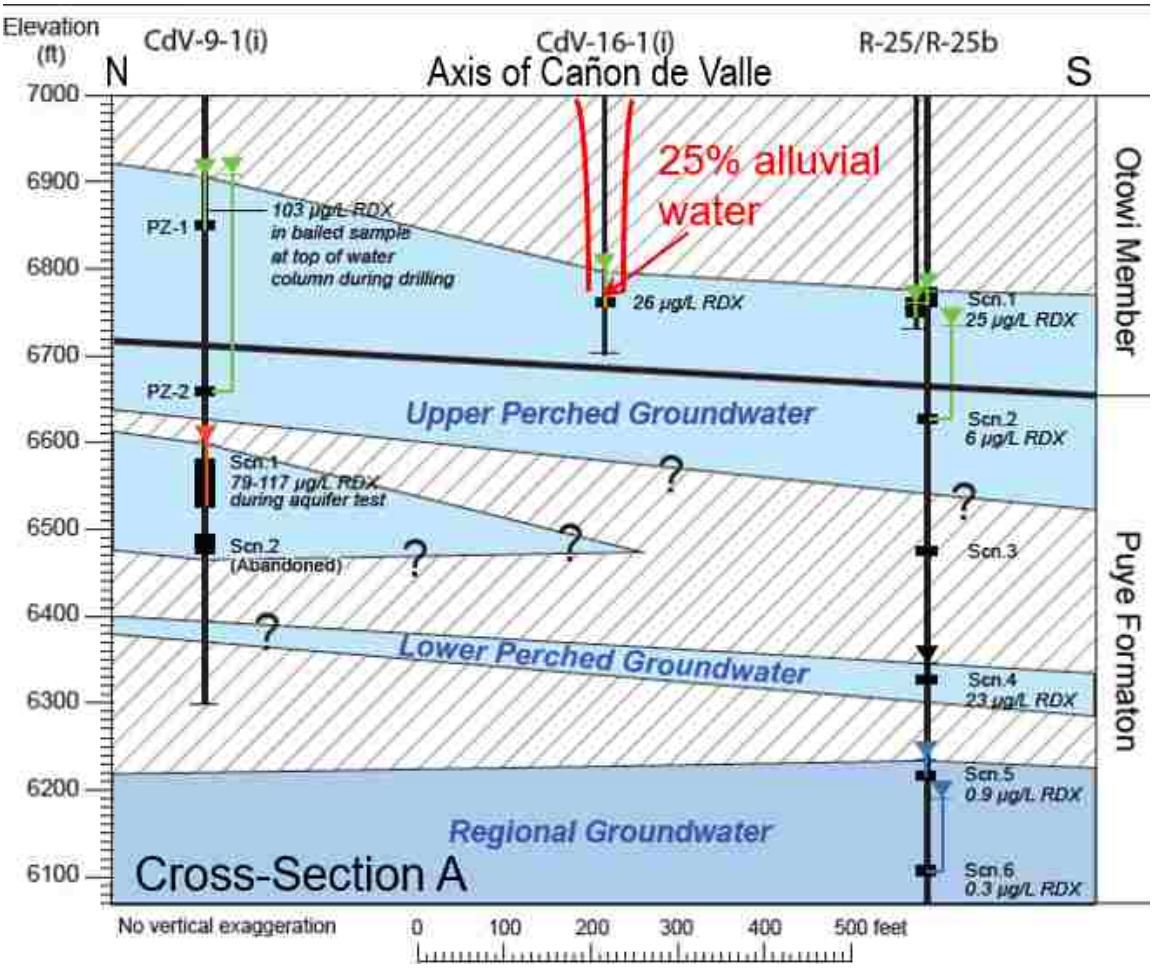

Figure 28: Mixing estimates for well screens in the upper perched zones are shown on conceptual cross-section TA-16 X-sections for CdV-9-1i pump test (Broxton).

An extended (ternary) mixing model was constructed, with water from R-26 PZ2 added to represent infiltration to the Otowi from the shallow intermediate zone. The best results of the ternary (added here as M3), based on dissolution of glass, similarity to the pattern of reactions in the discrete model, and chloride mass balance, were binary results very similar to M2 – there were no results mixing three end members. Therefore, M1 is chosen because it best fits the pattern of likely dissolving phases, and gives the greater estimate of alluvial mixing. Considering the surface location of CdV-16-1(i) on the alluvial

aquifer and in the perennial reach of Cañon de Valle, this analysis suggests that intermediate groundwater in the top of the upper intermediate zone consists of 25% alluvial percolation at a maximum. Outside of the wet canyon environment the influence of alluvial or shallow intermediate groundwater is smaller, as illustrated by the following model.

For modeling of flowpath N, ending in the Otowi at R-25b, which is a mesa location rather than a canyon location, nine mixing models were produced with a 9% uncertainty limit. The shallow intermediate zone, represented by water chemistry of 16-26644, mixes with the intermediate groundwater represented by R-26 Screen 1. Unlike the mixtures with 17-25% alluvial water in CdV-16-1(i) models described above, all but one of these models have no alluvial aquifer water; this is consistent with the restricted, matrix flow character of groundwater at R-25b as described previously, and the location or R-25b on the mesa and not directly below the alluvial zone. Perhaps also consistent with longer residence times, the mass transfer of glass and chalcedony (in Series N6 and N7) is an order of magnitude greater than in CdV-16-1(i), which accesses, apparently, a fracture-flow network and pulses of snowmelt. Series N6 has the smallest error of chloride mass balance (0.05 mg/L); it results from a mixture with 95% input from R-26 Screen 1 and about 5% shallow intermediate zone water (Figure 28). Series N7 has 99% input from R-26 Screen 1. The added mixing aspect of this model does very little to change the mass transfer coefficients from the discrete inverse model; however, the uncertainty limit for this plot is 9% rather than 19%. Larger mass transfer coefficients for this model, as compared to the preferred M model, make sense as a function of longer residence time of

water under matrix flow conditions. Five of the models that precipitate silica are shown in Figure 29. Series N6 and N7 stand out as the only two that dissolve glass.

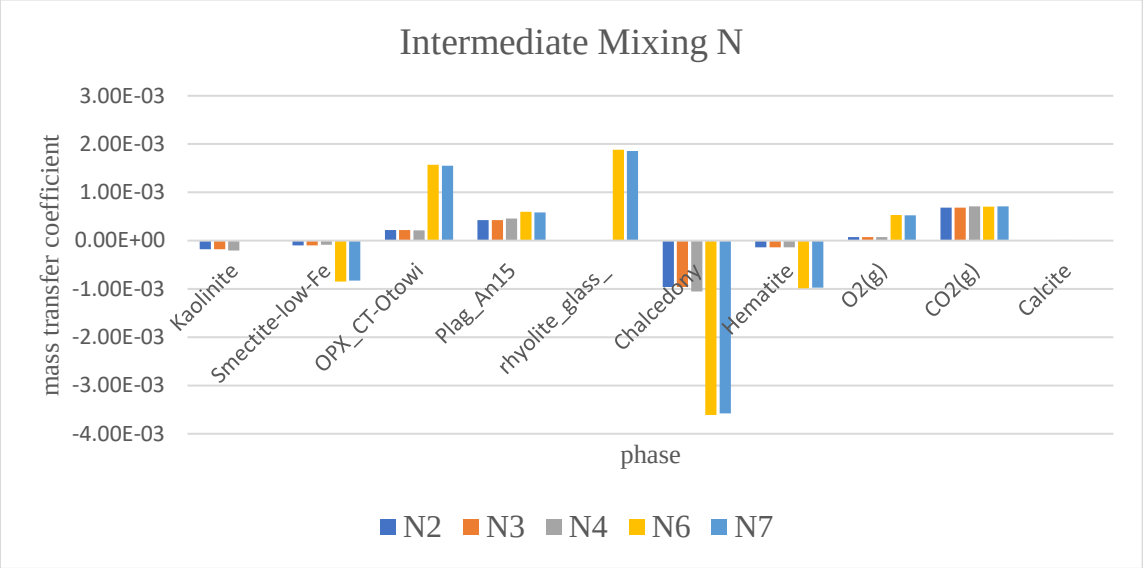

Figure 29: Inverse mixing model results for flowpath N. Two prominent models consist of 95% (N6) and 99% (N7) R-26 Screen 1 water chemistry. These two also have the lowest Cl mass balance errors.

Preferred models for M and N are compared to the Martin Spring discrete flowpath (Table 8), demonstrating the potential for precipitation of a phase such as chalcedony or opal-CT, given sufficient silica saturation. Saturation indices for chalcedony are positive uniformly, around 1, in several waters. At R-26 Screen 1 the value is 0.91; at CdV-16-1(i) it is 0.96; at R-25b it is 1.02; at Martin Spring it is 0.97. Though it is also 1.02 at CdV-16-4(i)p Screen 1, there is no evidence of soluble glass there. It is possible that precipitation of a silica phase keeps the saturation index low where glass is actively dissolving, and that the tipping point is somewhere in the range of 1.

	Plagioclase	**Smectite**	**Rhyolite Glass**	**Hematite**	**Calcite**	**Chalcedony**

M1	5.10 e-5	-9.50 e-5	1.53 e-4	-2.26 e-4	---	-5.16 e-4
N6	5.97 e-4	-8.46 e-4	1.88 e-3	-9.88 e-4	---	-3.61 e-3
L9	9.58 e-4	-1.44 e-3	3.57 e-3	-1.64 e-3	8.14 e-5	-6.0 e-3

Table 8: Comparison of mass transfer for selected models in the Otowi and Qbt4 tuff (Martin Sp)

3.1.2.1.2 Otowi and Puye mixing models

Assuming that water in CdV-16-1(i) is generally representative of mobile intermediate water in the Otowi, the following model uses its chemistry to explore mixing between the Otowi Member and the Puye Formation along flowpath F, between CdV-16-4ip Screen 1 and CdV-16-2ir. At the same uncertainty limit as the discrete model experiment (3.6%), mixing model O generated the same five non-mixing models plus one other, O5, shown in yellow in the plot below (Figure 30). The mixing proportions are 85% Puye Formation water and 14% Otowi Member water from 16-1(i). This model cannot be validated by chloride mass balance, however, which would predict increasing Cl^- with mixing along the flowpath. Chloride is lower at 16-2ir (2.5 mg/L) than at 16-4(i)p Screen 1 (3.5 mg/L), while in the Otowi Member at CdV-16-1(i) it averages 6.7 mg/L. Attempts to make models for this flowpath with mixing of water from R-25b, where Cl^- is 2.2 mg/L, were unsuccessful. Model O1 was rejected, and is not shown in the figure, because it dissolves glass and precipitates silica within the Puye Formation, even though there is no addition of water from the Otowi Member.

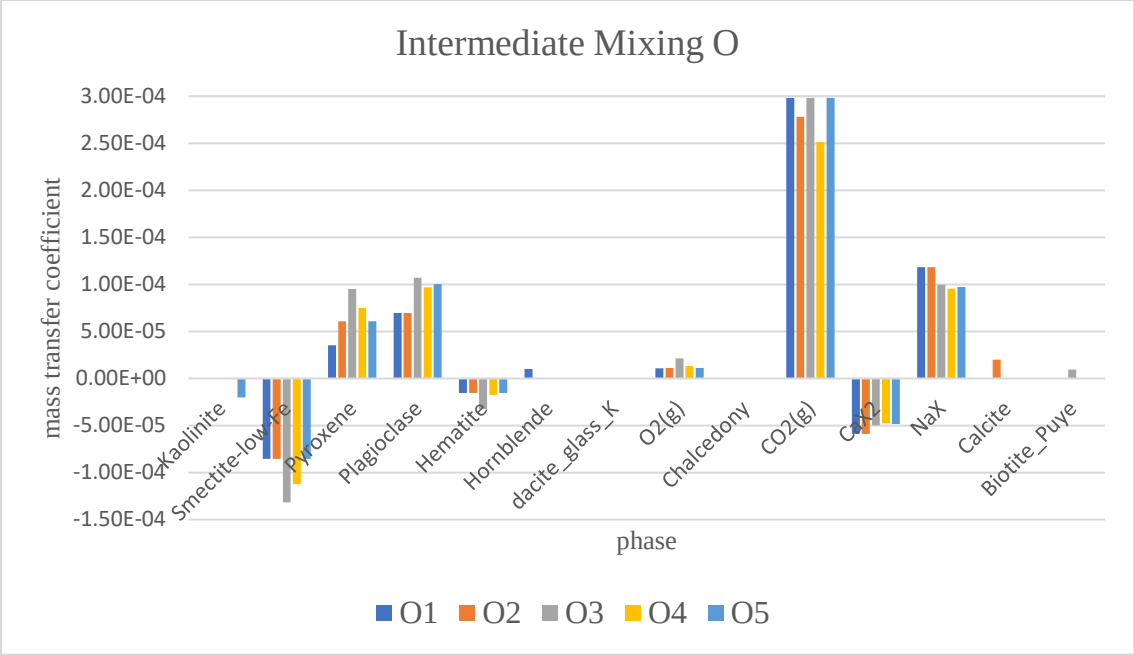

Figure 30: Results from mixing model O, with overlying Otowi Member water added to the inverse model for flowpath F, in the Puye Formation.

Flowpath G, discussed above, begins at CdV-16-4(i)p Screen 1 and ends at well R-47i, crossing below an ephemeral section of the channel in Cañon de Valle (Table 2a). Mixing experiment P reworks this flowpath as a mixing model which, in addition to water from the Otowi Member moving downgradient and downsection toward R-47i, explores the possibility that alluvial groundwater is added to the upper Puye Formation below the saturated channel (Table 2b). Reasonable chloride mass balance errors, below 4 mg/L, were given for four mixing models. Simulation P1, which has the smallest chloride mass balance error, would indicate that roughly half of the downgradient water in the upper intermediate zone moves down from the Otowi tuff (Figure 31). Though it has a larger chloride mass balance error, simulation P2 could be preferred because, like other preferred models, it includes hematite precipitation; it consists of 81.3% water from CdV-

16-4(i)p Screen 1 and 18.7% alluvial aquifer water, and the remaining two models have similar mixing ratios, mass transfers, and chloride mass balance errors. Overall, the mass transfer coefficients are consistent with the discrete intermediate Puye models.

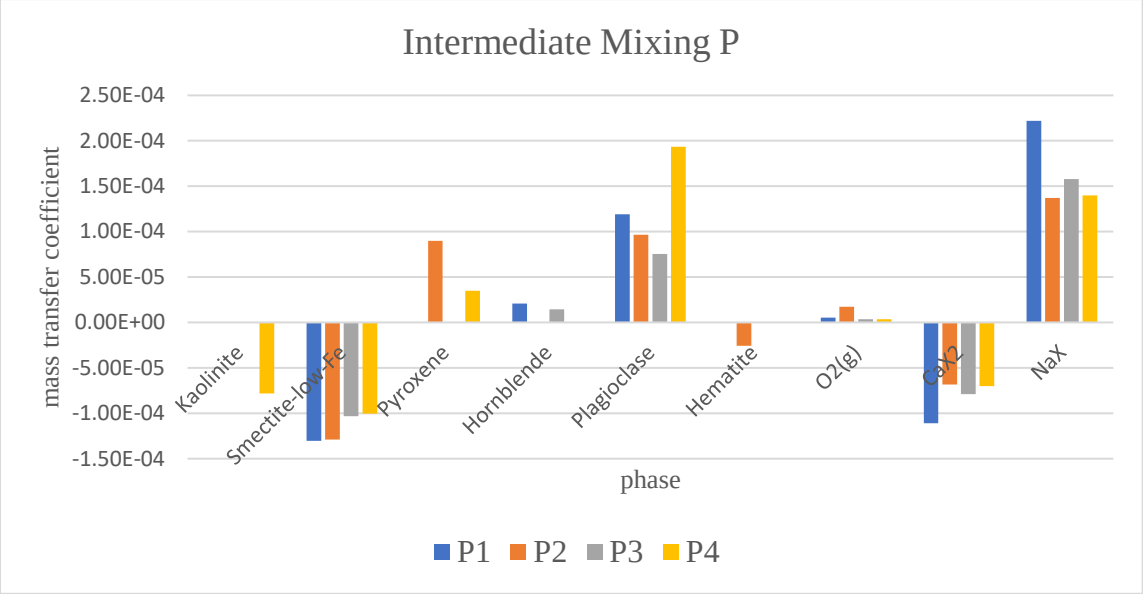

Figure 31: Inverse mixing model results with 16-1(i) water and alluvial water added into flowpath G in the Puye Formation, ending at well 47i. Uncertainty limit was set at 9%.

3.1.2.1.3 Summary of Phase I mixing results

The models presented above support a conceptual model where between 5% and 25% of upper intermediate groundwater originates at the surface or in the vadose zone of TA-16. The area of surface saturation in Cañon de Valle, between Burning Ground Spring and the channel to the north of R-63, would be the alluvial source from which up to 25% of water in CdV-16-1(i) comes. There is probably some spreading laterally of this recharge, especially if the Guaje pumice bed acts as a capillary barrier in any way. In the Otowi Member adjacent to the channel, there may be less mobile groundwater held in porous

rock matrix. Infiltration through adjacent mesa structures probably makes up less than 5%, and perhaps less than 1%, of upper intermediate water, judging from the results of the R-25b models N6 and N7. At least seventy-five percent of water in the Otowi Member, according to the conservative estimate made by model M1, would be laterally-migrating recharge from the fault zone, though some part of that could result from downward fracture flow or stair-stepping of water perched on bedding planes in the Tshirege tuff. To say that local recharge represents 25% of water in the CdV-16-1(i) screen is not to suggest that a similar proportion is present throughout the upper intermediate zone; due to anisotropy, vertical mixing is expected to be limited. Groundwater in sedimentary formations tends to follow anisotropic, laminar flow patterns (Freeze and Cherry, 1979), so it is assumed that the top of the hydrostratigraphic unit represents the maximum local input. Mixing experiment P takes a similar approach to modifying experiment G, which follows an intermediate flowpath to the downgradient well R-47i; both alluvial water and Otowi Member water are added. Results suggest either is possible, but no model incorporates both. From the mesa wells to the south of the canyon to below the channel section where saturation is transient, model P2 suggests that about 19% of water in the upper intermediate zone could originate at or near the surface. Alternatively, P1 suggests that at R-47i, about half of the water is Otowi Member mountain block recharge. Although none of the models mixed three end members, there is consistency between each of these models with respect to local recharge input and the conceptual hydrologic model.

3.1.2.2 Phase II mixing models

Sets of mixing models were constructed to explore the origins of intermediate water in

the Puye Formation, including some deeper zones that are not well understood in the conceptual hydrologic model, as well as regional water in wells that have had detection levels of RDX. In Phase II models, no main source water is assumed, but rather, groundwater chemistry profiles that are characteristic of mountain block recharge and local recharge are supplied as initial water end-members. Mountain block recharge is represented by upper canyon Spring 5.29 water, a proxy for water exposed to dacitic bedrock, and water in well R-26 Screen 1, which is located in the Cerro Toledo Formation and exposed primarily to weathered or in-situ Otowi Member tuff. Local recharge is represented by alluvial aquifer water and water Burning Ground Spring, which has exposure to welded Tshirege tuff.

3.1.2.2.1 Upper intermediate zone mixing

In the upper intermediate zone, CdV-16-4(i)p Screen 1 is the endpoint for mixing experiment Q. Model simulation Q7, with the smallest chloride mass balance error (0.79 mg/L), has mass transfer reactions that are comparable to the previous Puye models (lower half of Table 5), and indicates 13% contribution by local alluvial aquifer water (Figure 32). A pattern of dominant mountain block water can be observed among other models with reasonably low chloride errors (below 2 mg/L), such as models Q4 and Q9, which indicate about 20-21% intermediate spring zone water. These percentages are consistent with previous simple mixing model projections of local recharge.

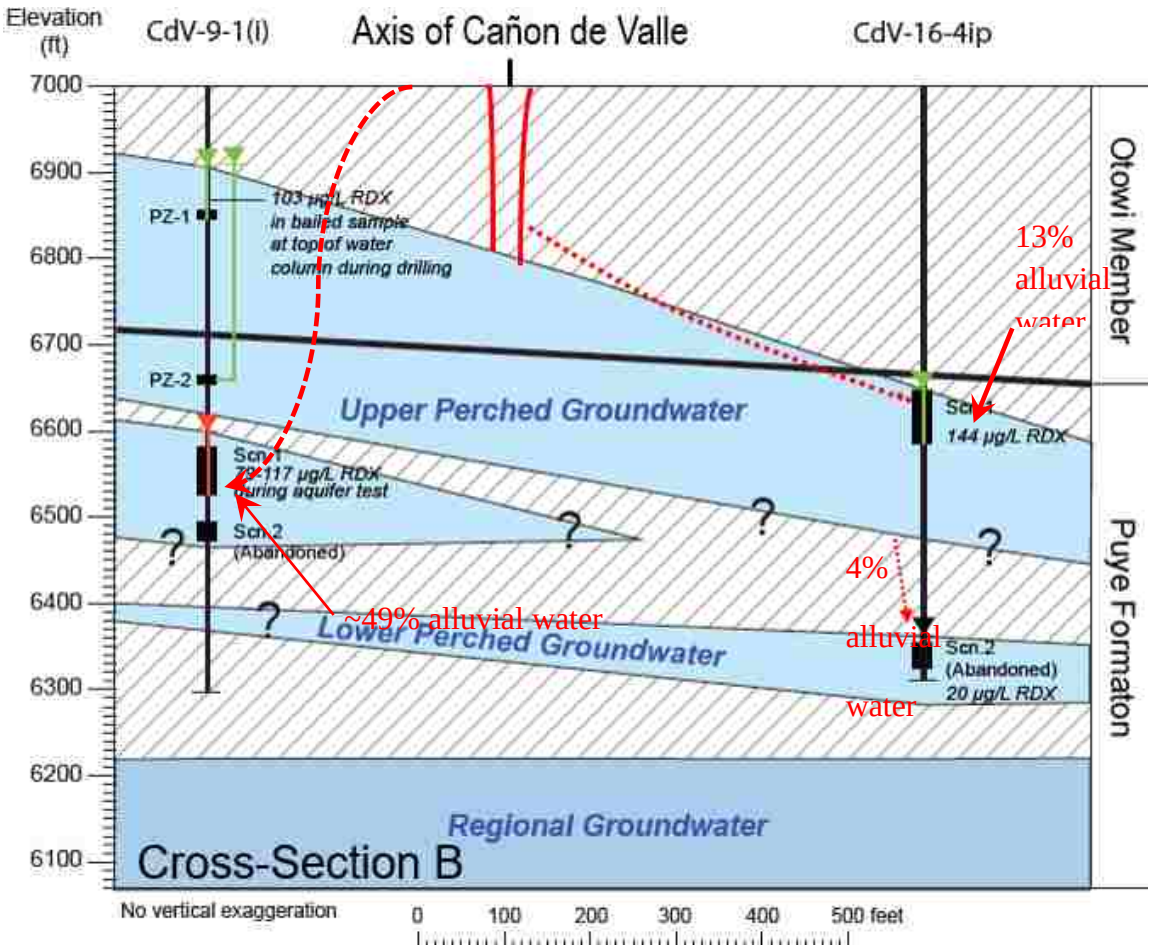

Figure 32: Estimates for local recharge in upper and lower intermediate well screens TA-16 X-sections for CdV-9-1i pump test (Broxton).

3.1.2.2.2 Lower intermediate zone mixing

The origin and extent of lower intermediate groundwater at TA-16 are poorly understood, due to a general lack of data and information about features in the deep subsurface. Some developed or planned well screens have been abandoned due to technical difficulties associated with working in unconsolidated formations at depth. Limited useful water chemistry data exists for two well screen locations, which may or may not be connected hydraulically. The following analyses are intended to suggest likely sources of water in these zones by extending the geochemical analysis of the previous sections. Rather than

assuming probable flow pathways, as with the discrete models and upper intermediate zone mixing models, these are more open-ended mixing models. The same four end-member water chemistry profiles, representing mountain-block and focused recharge, and spring zone and alluvial aquifer water, are input to PHREEQC as possible components of a final water, with the same phase specifications for reactions in the Puye Formation as used in previous runs. The final phase of this study builds on the previous modeling work to characterize mixing in deeper groundwater environments, from which less data is available. Though the mixing models give interesting quantitative results for source attribution, the intent is to show the most probable recharge sources from among defined end-members, as well as to identify source waters that PHREEQC was unable to reconcile with each of the final aggregate water compositions.

3.1.2.2.2.1 Mixing Experiment R - CdV-9-1(i)

The main screen of well 9-1(i) samples water from a zone of intermediate saturation that appears unconnected, or connected in a limited way, to the main upper zone, as shown in Figure 32. Recent water level data from this screen suggests that the zone may receive focused snowmelt recharge fairly rapidly. Average chloride is 11 mg/L, which exceeds other intermediate water in the Puye Formation by a factor of three or more, suggesting that near-surface groundwater could be a contributor. Also, the wellhead lies just north of the channel, about 1000 ft east of Burning Ground Spring.

The mixing model simulations from CdV 9-1i show the weakest input of mountain block recharge to the intermediate zone from among the results in this study. Among these models, the lowest chloride mass balance errors are associated with strong alluvial input,

between 38 and 51%; otherwise, it appears that if perched water from Qbt3t were a strong influence, the local recharge fraction would be even higher, from 64 to 83%. However, the chloride mass balance errors associated with Qbt3t water are higher. The mass transfer coefficients of selected Puye inverse models are compared to selected Puye mixing models. In the lower intermediate zone at CdV-9-1i, simulation R6 is favored, at 39% alluvial recharge, because of low chloride error and best agreement with mass transfers in other preferred Puye models (Table 9). Consistency among mass transfer coefficients of preferred model simulations in the Puye Formation can be observed.

Inverse model	Plagioclase	Smectite	Dacite Glass	Hematite	Calcite
A4	3.73 e-5	-1.65 e-4	4.65 e-4	-6.35 e-5	8.70 e-5
B10	---	-1.22 e-4	5.06 e-4	-2.39 e-5	1.19 e-4
C2	3.13 e-5	-1.20 e-4	2.79 e-4	-5.14 e-5	1.53 e-4
D1	7.89 e-5	-1.49 e-4	1.86 e-4	-6.75 e-5	---
E3	7.43 e-5	-1.70 e-4	3.10 e-4	-7.39 e-5	---
F1	6.96 e-5	-8.53 e-5	---	-1.53 e-5	---
G6	1.23 e-4	-1.56 e-4	---	-4.51 e-5	---
Inverse mixing model					
P2	9.67 e-5	-1.29 e-5	---	-2.57 e-5	---
Q7	8.47 e-5	-1.13 e-4	---	-4.42 e-5	
R6	1.09 e-4	-1.65 e-4	---	-6.63 e-5	---
S4	9.27 e-5	-1.18 e-4	---	-5.68 e-5	---
T6	8.19 e-5	-1.14 e-4	---	-6.08 e-5	---
U4	7.63 e-5	-1.08 e-4	---	-6.12 e-5	---

Table 9: Comparison of mass transfer coefficients for selected Tschicoma and Puye models. A to C are Tschicoma; D and E regional Puye; F and G intermediate Puye; P to U are Puye mixing models.

3.1.2.2.2.2 Mixing Experiment S - CdV-16-4(i)p Screen 2

Lower perched groundwater, as depicted in Figure 32, was sampled in now-abandoned CdV-16-4(i)p S2. The end member waters given as sources of this saturation lens include those considered for the previous models: Spring 5.29 and R-26 Screen 1 as mountain block recharge sources, and alluvial aquifer water and Burning Ground Spring water as

local recharge sources. Also included is the water from CdV-9-1(i), to the north of the canyon. Again, the Puye Formation mineral phase specifications were used. Results show a stark contrast from 9-1(i), in that almost everything traces back to mountain block recharge, with only small amounts of input from local sources. The two smallest chloride errors are associated with 96% or above mountain block sources; one showing 3% influence of Tshirege shallow intermediate zone (S8) and one showing 4% influence of the alluvial aquifer (S4). Simulation S4 mass transfers are in better agreement than simulation S8, which has only slightly less Cl error, though both are very low. The dominant source in all but one of the models is Spring 5.29, associated with dacite rock influence, rather than R-26 Screen 1, associated with tuff. In none of the reasonable models was there any input from CdV-9-1(i). These model results suggest that lower intermediate water to the south of the canyon has been supplied slowly by a mountain block source in dacite, while the lower zone to the north is supplied more rapidly by a source closer to the surface.

3.1.2.2.3 Regional aquifer mixing models– R-63 and R-18

Mixing models for the two regional wells with RDX detections, R-18 and R-63, also show dominant mountain block recharge sources, as would be expected. The same mountain block recharge sources (Spring 5.29 and R-26 Screen 1) and local recharge sources (alluvial water and Burning Ground Spring) are used as inputs.

Of eight model simulations for mixing at R-63, two have more than 8% local recharge; these are also models with the highest chloride mass balance errors, and the only two that include dissolution of dacite glass, though it may occur in the Puye Formation. Of the six

simulations with lower chloride mass balance errors, three specify 95% mountain block water to 5% alluvial water. Series T6 is preferred, as it has mass transfers reasonably similar to the Puye inverse models, with smectite as the only clay, and ion exchange as expected. The other three models that do not dissolve glass indicate 8% shallow intermediate zone water, and 92% mountain block recharge.

Model U4 is preferred for the R-18 mixing model; this also indicates a mixture of 95% mountain block recharge with 5% local recharge. Like T6, it is chosen because smectite as the only clay precipitated, and ion exchange agrees with previous favored Puye Formation models. In none of the R-18 models is there glass dissolution, though this is not entirely consistent with the results of discrete regional flowpaths in the Puye Formation.

These mixing model results suggest that 5% is a reasonable figure for local recharge in the regional aquifer, though the number could be higher close to the water table or near faults.

4.0 Discussion

4.0 Chloride mass balance errors and model residuals

Conservative behavior is assumed for chloride, and since it is not a mass balance constraint in PHREEQC inverse models, it can be observed in mixing scenarios as an independent check, to either validate or reject model results. Chloride mass balance error was contrived for this purpose, first as a way to make reasonable flowpath assumptions, then later as a means to assess individual mixing models. As part of each inverse model produced, a sum of residuals is included, providing a sense of which simulation in each experiment is closest to optimal, mathematically, given the constraints. Due to the approximate nature of nearly every aspect of the modeling exercise and the uncertainty involved, it is assumed that neither metric is necessarily more accurate; however, in many instances there is agreement between low chloride errors and lower residuals. Results for mixing models often include inverse models where mixing does not occur, but rather a single end member evolves to the final water composition by mass exchange with the solid phases within the specified limits. This type of model is sometimes associated with lower residuals, though these simulations were rejected as mixing was assumed for the purpose of conservative estimation of local recharge. Invariably, non-mixing inverse models for lower intermediate groundwater, where they occur, produce results with 100% mountain block recharge. For the upper screen of CdV-16-4(i)p, three residuals are below 7, and the lowest chloride error is associated with the third-lowest residual in Q7, the preferred model. In CdV-9-1(i), the preferred model R6 has the smallest residual and second smallest chloride mass balance error. The model with the next largest residual, R7, also has the smallest chloride mass balance error. In many cases, the values for each are very close among models, with the models themselves generally agreeing with

respect to mixing proportions.

4.1 Dominant geochemical processes as supported by modeling

Modeling of the geochemical processes in Cañon de Valle groundwater provides a foundation for inputs to mixing model experiments, as well as a basis for evaluating results. The discrete model experiments are intended to test certain assumptions with regard to flow pathways, explore the activity of soluble phases such as glass and calcite in different formations, and establish working patterns of mass transfer with each. Not detailed in this thesis are many preliminary inverse model trials, including and excluding various glass phases, chalcedony, calcite, and sulfate minerals.

Limited comparison can be made to similar inverse model work done on the Pajarito Plateau by Hereford, et al. (2007). In that study, reaction rates were determined along a broader regional flowpath, the first section of which is analogous to flowpaths discussed in this study, involving migration of perched intermediate water to the regional aquifer. Clay precipitation was observed evenly on grains of potassium and plagioclase feldspars, informing model inputs that forced Ca-montmorillonite precipitation and dissolution of feldspars. Saturation rates are only shown for calcite, silica, and glass; the saturation states of aluminosilicates were not calculated, for lack of data on dissolved Al. Potassium feldspar was thought to be subject to dissolution, though at a much slower rate than plagioclase. Inverse model simulations show that kaolinite was not constrained in model inputs, and was determined in preferred models to dissolve, which is at odds with the positive Saturation Indices calculated for kaolinite in all waters for this study. Also, in the preferred model, calcite precipitated significantly, though the water was shown to be

undersaturated with respect to calcite until the third segment, within the regional aquifer. These issues were identified and resolved somewhat in the text, by the suggestion that although calcite was undersaturated at both sampling points, it may have been supersaturated locally at points in between. The study used little analytical chemistry data and few sampling points, three of which are in the Santa Fe aquifer; however, it used more in the way of electron scanning micrographs to observe precipitation and dissolution.

In forward modeling compiled for this thesis paper, calcite is indicated to be a dissolving phase; though it was not constrained as such in model inputs, inverse results are all in agreement and never show it precipitating. Kaolinite is indicated as a precipitating phase, based on forward modeling results, and there is no reason to expect it to dissolve, especially in an environment where illite and Ca-montmorillonite clays are precipitating. Also, though the Santa Fe Group aquifer may be undersaturated with respect to potassium feldspar, it is stable in every water considered in this study. It is unlikely that much potassium could accumulate in solution even if dissolution were taking place, and so slowly compared to glass and plagioclase.

Equilibrium chemistry provides critical tools for constraining reacting phases in inverse models. An assumption that little to no aluminum was in solution would have helped determine saturation indices for aluminosilicates and clays, better guiding the analysis in Hereford, et al. (2007).

Ultimately, it appears that regional pathways between the high spring and Tschicoma Formation well screens rely on some exposure to soluble calcite, while those that end in

regional Puye Formation screens do not. The five regional models suggest that soluble dacitic glass is encountered along regional flowpaths in both the Tschicoma and Puye Formations; however, glass reactivity does not appear to be an important factor in intermediate groundwater in the Puye Formation. Among preferred models in the Puye, a consistent plagioclase feldspar composition yields mass transfer coefficients between about 7.0 e-5 and 1.2 e-4. Smaller values are recorded for plagioclase models in the dacite formation, together with larger values for both glass and calcite dissolution. This is reasonable because both are highly soluble, and calcite and carbonic acid could be present together in the upper mountain vadose zone.

Phase I mixing models are used to gauge local recharge to the top of the upper intermediate zone, and the contribution of predominantly tuff zone mountain block water to the underlying section of the main intermediate zone. These estimates are necessarily inexact, but each refines an oversimplified discrete model derived with a high uncertainty limit. Flowpaths H and I are improved by local alluvial recharge addition in experiments M and N, respectively. Each indicates a reasonable alluvial input and carries a small chloride mass balance error, and is produced with a far smaller uncertainty limit. Glass dissolution and reprecipitation of silica, both predicted by inverse model experiments H and I, are suggested again by inverse mixing experiments M and N, but at a less excessive scale.

The intent of Phase I mixing models, as well as the discrete models along the shallow intermediate springs zone, is to enable a better understanding of the geochemistry, of how modeling can be used to explore connectivity, and validity of assumptions relating to

mixing. While yielding limited, yet reasonable, estimates of local recharge, this section provides intelligible and encouraging results as far as confidence in the overall modeling approach, applicability of the data, and responsiveness of discrete models to mixing inquiries. Across the preferred inverse models, the scale of reactions in Puye sediments is acceptably consistent (Table 9), and supports the mixing scenarios indicated by minimal model residuals and chloride mass balance errors.

4.2 Hydrologic model concepts supported by this work

The inverse mixing results support a conceptual model with up to 25% of intermediate groundwater from local recharge sources at TA-16. On the south and east margins of intermediate water, input from local recharge sources appears to be more diluted, at 13% to 20%. To the north of the canyon, a larger amount of local recharge (~50%) apparently reaches the lower zone of intermediate groundwater, though the location of the recharge source is unclear. Other models suggest that about 5%, and no more than 8%, of water in the top of the regional aquifer originating at or near the surface in TA-16. Five percent input transported from a contaminated vadose zone could bring RDX in small amounts, mixing with older mountain block recharge and diluting surface water enough to not detect tritium. A very small amount of local recharge explains how RDX could continue to increase at R-18, to the northeast of TA-16, even if the source is in surface sediments or near-surface surge beds.

Another regional well, R-68, has recently been developed to the northeast of CdV-9-1(i), and it has detected RDX at around 9 µg/L. Reliable water chemistry is not yet available to use in this study. The screen is closer to the water table than the R-18 screen, perhaps

explaining the higher concentration. It would appear that one or more saturated pathways to deeper intermediate groundwater enhance downward mobility north of the canyon. This idea is supported by the modeling presented here for water in the CdV-9-1(i) zone, and the regional aquifer at R-18, as well as other observations, such as are presented in Appendix B, a related study on mountain front recharge. As CdV-9-1(i) is located more than 1,000 ft to the east of the 260 Outfall, any discontinuity in that area, such as a fault, is a potential pathway for further introduction of recently dissolved RDX. Whatever diffuse reservoir of such solid phase HE materials that exists in Cañon de Valle and adjacent mesa structures is not understood or necessarily accessible. It may be inert in dry conditions and activated by transient saturation during snowmelt events.

On the south side of the canyon, at R-63, the level of RDX has remained constant rather than risen over time; this area could also receive small amounts of local recharge, but there remains the possibility that water introduced to the regional aquifer there by the open R-25 borehole continues to have an influence. The lens of deep intermediate water to the south of Cañon de Valle seems to be emplaced mostly, if not quite entirely, by the lateral flow of mountain front recharge rather than by downward percolation from the upper zone. A small influence of local recharge at the top of the upper intermediate zone seems unlikely to translate to noticeable influence in the lower zone. Assuming there is communication between the two, with 15% local recharge in the upper zone and 15% lower zone water coming from the upper zone, the lower zone would consist of 2.25% local recharge at a maximum. This would assume mixing in the upper intermediate zone, so it seems to be a highly unlikely scenario.

4.3 Related and future work

Appendix A is an updated assessment of the overall inventory of RDX believed to be present in groundwater zones below TA-16, based on available aqueous chemistry data, as well as in surface sediments. Appendix B is a record of a springtime snowmelt recharge event that was recorded by transducers in CdV wells, as part of a Mountain Front Recharge (MFR) study of upper Cañon de Valle. This is especially relevant and interesting with respect to mixing model results for well CdV-9-1(i).

More information, such as stable isotope data, may be useful to this inquiry; PHREEQC does allow for stable isotopes to be tracked in inverse modeling as mass balance constraints, though it is unclear if actually integrating it into models is worthwhile. Unfortunately, there is no tritium data from the window in time when CdV-16-4(i)p S2 was active, nor has there been yet from CdV-9-1(i). Large data gaps, as there are here, cause uncertainty to be high. More monitoring well development, and associated analytical chemistry, is helpful and could alter the overall picture of the hydrology as well as contamination; however, it would not be much of an improvement in terms of uncertainty. Considering the expense of monitoring wells, integration of different data types and carefully considered use of averages and proxies seems like an efficient way to use the data that already exists. Integration of new analytical data from regional wells under development may show similar mixing scenarios, though it could reveal something different. The hope is that extension of this modeling study with new data can provide low-cost benefits to future planning.

5.0 Conclusions

From evaluation of the models described above, a reasonable determination would be that lateral, eastward flowing mountain block groundwater dominates the saturated intermediate zones that are the focus of this inquiry. While surface saturation does certainly find a way into the upper intermediate zone, it enters a stratified and poorly-mixed compartment. Where there is communication between zones, it would appear that there is negligible downward transmissivity through saturated bodies. The RDX in intermediate zones is evidence that process water has migrated downward, though what is at lower depths may be decades old and has been introduced at a time when high explosives processing was at its peak, with the outfall matching or even exceeding the natural state of recharge. It is also possible that some RDX at lower depths was introduced by drilling. The geochemical analysis in this study seems to agree with assumptions based on tritium – that surface water below the fault, and near-surface groundwater at TA-16 influences the upper intermediate zone somewhat, but downward penetration of the zone by water that accesses HE solids, or high aqueous concentrations of RDX, happens slowly in most places. Recharge may occur suddenly and irregularly, as a result of snowmelt events, but overall, mountain block groundwater seems to dominate input to the perched zones, and dilution and dispersion probably are factors as the water moves downgradient. Local recharge as low as five percent does not eliminate the threat of further contamination of regional groundwater, though it suggests that continuous dilution by dominant mountain block recharge may keep concentrations low.

Future hydrochemical studies in this and similar volcanic rock terrains would do well to focus on controlling geochemical processes identified here, particularly dissolution of

glass and plagioclase silicate materials. Iron-bearing silicates could also be useful, though iron would need to be better constrained by observations related to sorption and complexation. Characterization of secondary minerals is important, and saturation indices should always be used to guide model assumptions. Chemical approximation of the dissolving phases is a useful strategy for building model inputs specifically for the host rock formations.

The intent of this research is to put existing aqueous chemistry data, collected mainly for regulatory purposes, to use as a means to better understand the complex hydrology associated with remediating contamination at Technical Area 16. Equilibrium chemistry serves as tool to guide localized experiments in inverse mass balance modeling. The existing conceptual model, based on extensive geological observations as well as mineral and chemical data, is useful for evaluating the results of experiments. The mixing function, coupled with inverse modeling, helps to improve upon some of the assumptions made for the initial flowpath models and characterize relationships between zones of saturation. Though it is a quantitative endeavor, ultimately the information returns to a qualitative conceptual model. The inverse mixing model process is applied in an attempt to expose the origin of recharge groundwater in a systematic way under realistic chemical constraints. More than to build faith in any specific estimates, the intended purpose of this study was to see the data through a new lens, which might have been revelatory in some way. The overall approach, which appears to have been successful here, is that integration of more and varied data types, and agreement between assumptions, constraints, and a conceptual model should yield reliable gross estimates of local recharge input, which are useful for planning future remediation activities.

6.0 References

Aishlin, P. and J. P. McNamara, 2011. Bedrock infiltration and mountain block recharge accounting using chloride mass balance. Hydrological Processes 25: 1934-1948.

Ajami, H., Troch, P. A., Maddock, T. 3rd, Meixner, T., and C. Eastoe, 2011. Quantifying mountain block recharge by means of catchment-scale storage-discharge relationships. Water Resources Research 47, W04504, doi:10.1029/2010WR009598.

Ashley, R. P., and J. W. Lloyd, 1978. An example of the use of factor analysis and cluster analysis in groundwater chemistry interpretation. Journal of Hydrology 39:355-364.

Bense, V. F., Gleeson, T., Loveless, S.E., Bour, O., and J. Scibek, 2013. Fault zone hydrogeology. Earth-Science Reviews 127: 171-192.

Birdsell, K. H., Newman, B. D., Broxton, D. E., and B. A. Robinson, 2005. Conceptual models of vadose zone flow and transport beneath the Pajarito Plateau, Los Alamos, New Mexico. Vadose Zone Journal 4:620-636.

Blasch, K. W., and J. R. Bryson, 2007. Distinguishing sources of ground water recharge by using δ^2H and $\delta^{18}O$. GROUND WATER 45 3:294-308.

Broxton, D., Woldegabriel, G., Peters, L., Budahn, J., and G. Luedemann, 2007. Pliocene volcanic rocks of the Tschicoma Formation, east-central Jemez volcanic field: chemistry, petrography and age constraints. New Mexico Geological Society Guidebook, 58th Field Conference, Geology of the Jemez Mountains Region II, p. 284-295.

Bowser, C. J., and B. F. Jones, 2002. Mineralogic controls on the composition of natural waters dominated by silicate hydrolysis. American Journal of Science 302 7:582-662.

Dalton, M. G., and S. B. Upchurch, 1978. Interpretation of hydrochemical facies by factor analysis. GROUND WATER 16 4:228-233.

Drever, J. I. (1982). *The geochemistry of natural waters.* Upper Saddle River, NJ: Prentice Hall.

Eby, G. N. (2004). *Principles of Environmental Geochemistry.* Belmont, CA: Brooks/Cole

Eggleton, R. A., and M. Aspandiar, 2007. Environmental Mineralogy: Honors Shortcourse, 18-22 June 2007. *CRC LEME Open File Report 206*. 159 pp.

Eriksson, E. (1985). *Principles and applications of hydrochemistry.* London: Chapman and Hall.

Freeze, R. A., and J. A. Cherry, 1979. *Groundwater.* Upper Saddle River, NJ: Prentice Hall.

Glynn, P. D., and L. N. Plummer, 2005. Geochemistry and the understanding of ground-water systems. Hydrogeology Journal 13:263-287.

Güler, C., Thyne, G. D., McCray, J. E., and A. K. Turner, 2002. Evaluation of graphical and multivariate statistical methods for classification of water chemistry data. Hydrogeology Journal 10:455-474.

Heilweil, V. M., Sweetkind, D. S., and S. J. Gerner, 2014. Innovative environmental tracer techniques for evaluating sources of spring discharge from a carbonate aquifer bisected by a river. Groundwater 52 1:71-83.

Hereford, A. G., Keating, E. H., Guthrie, G. D. Jr., and C. Zhu, 2007. Reactions and reaction rates in the regional aquifer beneath the Pajarito Plateau, north-central New Mexico, USA. Environmental Geology 52:965-977.

Katz, B. G., Coplen, T. B., Bullen, T. D., and J. H. Davis, 1997. Use of chemical and isotopic tracers to characterize the interactions between ground water and surface water in mantled karst. GROUND WATER 35 6:1014-1028.

Kleinfelder, Inc., 2005. "Final Well R-26 Completion Report" Los Alamos National Laboratory, Los Alamos, New Mexico, January 25, 2005. Project No. 37151 (KA Project No. 37151, 2005)

Kwicklis, E., Witkowski, M., Birdsell, K., Newman, B., and D. Walther, 2005. Development of an infiltration map for the Los Alamos area, New Mexico. Vadose Zone Journal 4:672-693.

LANL (Los Alamos National Laboratory), March 2002. "Characterization Well R-25 Completion Report" Los Alamos National Laboratory document LA-13909-MS, Los Alamos, New Mexico. (LANL ER2001-0697)

LANL (Los Alamos National Laboratory), March 2002. "Well CdV-R-37-2 Completion Report" Los Alamos National Laboratory document LA-14023-MS, Los Alamos, New Mexico. (LANL ER2002-0557)

LANL (Los Alamos National Laboratory), September 2003. "Phase III RFI Report for Solid Waste Management Unit 16-021(c)-99," Los Alamos National Laboratory document LA-UR-03-5248, Los Alamos, New Mexico. (LANL 2003, 77965)

LANL (Los Alamos National Laboratory), December 2005. "Hydrogeologic Studies of the Pajarito Plateau: A Synthesis of Hydrogeologic Workplan Activities (1998-2004)" Los Alamos National Laboratory document LA-14263-MS, Los Alamos, New Mexico. (LANL ER 2005-0679)

LANL (Los Alamos National Laboratory), January 2011. “Completion Report for Intermediate Well CdV-16-4ip” Los Alamos National Laboratory document LA-UR-11-0187, Los Alamos, New Mexico. (LANL EP2010-0538)

LANL (Los Alamos National Laboratory), September 2011. “Investigation report for Water Canyon/Cañon de Valle” Los Alamos National Laboratory document LA-UR-11-5478, Los Alamos, New Mexico. (LANL EP-2011-0227)

LANL (Los Alamos National Laboratory), June 2015. “Completion Report for Intermediate Aquifer Well CdV-9-1(i)” Los Alamos National Laboratory document LA-UR-15-23954, Los Alamos, New Mexico. (LANL EP2015-0094)

LANL (Los Alamos National Laboratory), November 2016. “Geology of Technical Area 16 and Vicinity, Los Alamos National Laboratory” Los Alamos National Laboratory document LA-UR-16-28402, Los Alamos, New Mexico. (LANL EP-2016-0113)

Manning, A. H., 2010. Mountain-block recharge, present and past, in the eastern Española Basin, New Mexico, USA. Hydrogeology Journal. DOI 10.1007/s10040-010-0696-8.

Marshall, R. R., 1961. Devitrification of natural glass. Geological Society of America Bulletin v. 72, pp.1493-1520.

Mazor, E. (2004). *Chemical and isotopic groundwater hydrology.* New York: Marcel Dekker, Inc.

Newman, B. D., Hickmott, D. D., and P. Gram, 2007. Flow and high explosives transport in a semiarid mesa in New Mexico, USA. Vadose Zone Journal 6:744-785.

Newman, B. D., Campbell, A. R., Norman, D. I., and D. B. Ringelberg, 1997. A model for microbially induced precipitation of vadose-zone calcites in fractures at Los Alamos, New Mexico, USA. Geochimica et Cosmochimica Acta, 61 9:1783-1792.

Parkhurst, D.L., and C. A. J. Appelo, 2013, Description of input and examples for PHREEQC version 3—A computer program for speciation, batch-reaction, one-dimensional transport, and inverse geochemical calculations: U.S. Geological Survey Techniques and Methods, book 6, chap. A43, 497 p., available only at http://pubs.usgs.gov/tm/06/a43/.

Pinault, J.-L., Plagnes, V., Aquilina, L., and M. Bakalowicz, 2001. Inverse modeling of the hydrological behavior of hydrosystems: Characterization of karst system functioning. Water Resources Research 37 8:2191-2204.

Reid, K. D., Reneau, S. L., Newman, B. D., and D. D. Hickmott, 2005. Barium and high explosives in a semiarid alluvial system, Cañon de Valle, New Mexico. Vadose Zone Journal 4:744-759.

Rogers, D. B., Stoker, A. K., McLin, S. G., and B. M. Gallaher, 1996. Recharge to the Pajarito Plateau regional aquifer system. New Mexico Geological Society Guidebook, 47th Field Conference, Jemez Mountains Region.

Samuels, K. E., Broxton, D. E., Vaniman, D. T., Woldegabriel, G., Wolff, J. A., Hickmott, D. D., Kluk, E. C., and M. M. Fittipaldo, 2007. Distribution of dacite lavas beneath the Pajarito Plateau, Jemez Mountains, New Mexico. New Mexico Geological Society Guidebook, 58th Field Conference, Geology of the Jemez Mountains Region II, pp. 121-132.

Sanford, W., 2002. Recharge and groundwater models: an overview. Hydrogeology Journal 10:110-120.

Stumm, W. and Morgan, J. J. (1996). *Aquatic chemistry: Chemical equilibria and rates in natural waters.* New York: Wiley & sons.

Tromp-van Meerveld, H. J., Peters, N. E., and J.J. McDonell, 2006. Effect of bedrock permeability on subsurface stormflow and the water balance of a trenched hillslope at the Panola Mountain Research Watershed, Georgia, USA. Hydrologic Processes 21:750-769.

van Tonder, G. J., and F. D. I. Hodgson, 1986. Interpretation of hydrogeochemical facies by multivariate statistical methods. Water SA 12 1:1-6.

Velbel, M. A., and W. W. Barker, 2008. Pyroxene weathering to smectite: Conventional and cryo-field emission scanning electron microscopy, Koua Bocca ultramafic complex, Ivory Coast. Clays and Clay Minerals 56 1:112-127.

Wahi, A. K., Hogan, J. F., Ekwurzel, B., Baille, M. N., and C. J. Eastoe, 2008. Geochemical quantification of semiarid mountain recharge. GROUND WATER 46 3:414-425.

Warshaw, C. M., and R. L. Smith, 1988. Pyroxenes and fayalites in the Bandelier Tuff: Temperatures and comparison with other rhyolites. American Minerolagist 73: 1025-1037.

Wilson, J. L., and H. Guan, 2004. Mountain block hydrology and mountain front recharge. In Hogan, J. F., Phillips, F. M., and B. R. Scanlon (Eds.), *Groundwater recharge in a desert environment: The southwestern United States* (pp. 113-137). Washington, D. C.: American Geophysical Union.

7.0 Supplementary Materials – part a

Forward Model Results

Phase	Surface	Regional Tschicoma Formation			Regional Puye Formation	
	Spring 5.29	R-37-2 S4	R-37-2 S3	R-48	R-63	R-47
Albite	1	2.26	2.4	2.21	2.92	1.78
Anorthite	-4.8	-2.26	-2.14	-2.13	-1.45	-3.8
K-Feldspar	3.73	4.34	4.38	4.06	4.89	3.73
Sanidine	2.41	3.11	3.14	2.84	3.62	2.46
Enstatite	-5.67	-3.49	-2.89	-2.23	-3.94	-3.81
Ferrosilite	-3	-1.46	-3.15	-3.4	-3.42	-3.43
Diopside	-9.06	-4.89	-3.69	-2.42	-5.68	-5.43
Hedenbergite	-9.11	-5.43	-6.53	-6.15	-7.8	-7.67
Tremolite	-22.37	-8.21	-3.99	0.36	-10.73	-9.89
SiO2 (am)	-0.26	-0.2	-0.16	-0.26	-0.12	-0.13
Chalcedony	0.89	0.85	0.89	0.78	0.98	0.96
Cristobalite alpha	0.59	0.56	0.6	0.49	0.68	0.66
Cristobalite beta	0.09	0.1	0.14	0.04	0.21	0.19
Tridymite	0.99	0.93	0.97	0.86	1.06	1.05
Calcite	-2.27	-1.08	-0.76	-0.42	-1.29	-1.2
Hematite	10.29	14.69	11.77	12.1	10.32	10.48
Smectite	2.19	5.07	4.75	4.78	4.78	3.36
Kaolinite	6.69	6.6	6.17	5.39	8.13	5.62

Table 10a: Saturation indices for aggregated regional recharge waters. Spring 5.29 is used as a proxy for precipitation in upper Cañon de Valle and starting point for inverse models to the 5 regional well screens.

Phase	Puye Formation S Intermediate		Puye Formation N Intermediate		Cerro Toledo to Puye Intermediate	
	16-4(i)p S1	16-2(i)r	16-4(i)p S1	R-47(i)	R-26 S1	9-1(i)
Albite	2.95	2.62	2.95	2.92	1.49	3.14
Anorthite	-1.77	-2.77	-1.77	-2.00	-4.02	-1.47
K-Feldspar	4.96	4.05	4.96	4.41	3.85	4.91
Sanidine	3.68	2.77	3.68	3.14	2.6	3.64
Enstatite	-4.25	-4.39	-4.25	-4.54	-3.58	-4.00
Ferrosilite	-3.31	-3.53	-3.31	-3.06	-3.54	-2.88
Diopside	-6.25	-6.46	-6.25	-6.80	-5.12	-5.83
Hedenbergite	-7.96	-8.25	-7.96	-7.95	-7.67	-7.35
Tremolite	-12.69	-13.50	-12.69	-14.83	-8.75	-11.29
SiO2 (am)	-0.09	-0.07	-0.09	-0.12	-0.16	-0.21
Chalcedony	1.02	1.03	1.02	0.97	0.91	0.88
Cristobalite a	0.72	0.74	0.72	0.67	0.62	0.59
Cristobalite b	0.24	0.26	0.24	0.20	0.15	0.11
Tridymite	1.11	1.12	1.11	1.05	0.99	0.97
Calcite	-1.44	-1.45	-1.44	-1.47	-1.23	-1.16
Hematite	10.2	9.71	10.2	10.47	10.45	11.57
Smectite	4.60	3.75	4.60	4.20	3.25	4.96
Kaolinite	8.18	7.28	8.18	8.05	5.16	8.11

Table 10b: Saturation indices for aggregated waters across three possible intermediate zone flow pathways, all within or into the Puye Formation.

Phase	Cerro Toledo to Otowi Intermediate a		Cerro Toledo to Otowi Intermediate b	
	R-26 S1	16-1(i)	R-26 S1	R-25b
Albite	1.49	2.74	1.49	2.92
Anorthite	-4.02	-1.96	-4.02	-2
K-Feldspar	3.85	5.04	3.85	5.18
Sanidine	2.6	3.77	2.6	3.88
Enstatite	-3.58	-4.18	-3.58	-4.05
Ferrosilite	-3.54	-3.26	-3.54	-2.85
Diopside	-5.12	-6.3	-5.12	-5.86
Hedenbergite	-7.67	-8.01	-7.67	-7.33
Tremolite	-8.75	-12.72	-8.75	-11.21
SiO2 (am)	-0.16	-0.13	-0.16	-0.1
Chalcedony	0.91	0.96	0.91	1.02
Cristobalite a	0.62	0.67	0.62	0.72
Cristobalite b	0.15	0.2	0.15	0.23
Tridymite	0.99	1.05	0.99	1.11
Calcite	-1.23	-1.34	-1.23	-1.12
Hematite	10.45	10.19	10.45	11.42
Smectite	3.25	4.52	3.25	5.02
Kaolinite	5.16	7.98	5.16	7.97

Table 10c: Saturation indices across two possible intermediate zone flow pathways above the Puye Formation.

Phase	Tshirege Member a		Tshirege Member b		Tshirege Member c	
	R-26 PZ2	Burning Ground Spring	R-26 PZ2	SWSC Spring	16-26644	Martin Spring
Albite	1.69	2.63	1.69	1.80	1.25	2.68
Anorthite	-2.73	-2.12	-2.73	-4.01	-4.95	-2.82
K-Feldspar	4.16	4.99	4.16	4.16	3.57	4.70
Sanidine	2.89	3.69	2.89	2.86	2.29	3.40
Enstatite	-4.72	-4.22	-4.72	-5.00	-4.41	-4.67
Ferrosilite	-3.59	-2.55	-3.59	-2.62	-2.72	-2.50
Diopside	-7.14	-6.18	-7.14	-7.70	-6.61	-6.96
Hedenbergite	-8.65	-7.16	-8.65	-8.00	-7.57	-7.45
Tremolite	-16.2	-12.52	-16.2	-17.79	-13.98	-15.31
SiO2 (am)	-0.38	-0.23	-0.38	-0.22	-0.21	-0.15
Chalcedony	0.72	0.88	0.72	0.91	0.9	0.97
Cristobalite a	0.43	0.58	0.43	0.61	0.6	0.67
Cristobalite b	-0.05	0.1	-0.05	0.12	0.12	0.18
Tridymite	0.81	0.97	0.81	1.00	0.99	1.06
Calcite	-1.06	-1.09	-1.06	-1.49	-1.29	-1.03
Hematite	9.74	12.06	9.74	11.17	11.39	11.42
Smectite	3.13	4.68	3.13	3.16	2.74	4.13
Kaolinite	7.31	7.71	7.31	6.67	5.11	7.46

Table 10d: Saturation indices across three possible pathways through Tshirege Formation to springs

7.1 Supplementary Materials – part b

Inverse Model Results

A (Regional) Spring 5.29 to R-37-2 Screen 3 9.5% uncertainty

Series >	A1	A2	A3	A4	A5	A6
Kaolinite		-2.57E-04			-2.42E-04	
Smectite	-2.61E-04		-2.65E-04	-1.65E-04		-3.07E-03
Hematite	-9.41E-05	-1.21E-05	-9.47E-05	-6.35E-05	-1.21E-05	-9.74E-04
Chalcedony			-3.44E-04			-6.33E-03
Pyroxene	2.77E-04	1.84E-05				3.05E-03
Hornblende			1.12E-04	7.25E-05	7.36E-06	
Plagioclase	6.24E-05	3.60E-04	6.34E-05	3.73E-05	3.38E-04	7.95E-04
Dacite glass	7.85E-04		7.98E-04	4.65E-04		1.01E-02
Calcite	2.40E-04			8.70E-05		
O2(g)	5.62E-05	4.80E-06	5.67E-05	3.71E-05	4.78E-06	6.09E-04
CO2(g)		3.86E-04	3.86E-04	2.99E-04	3.86E-04	3.86E-04
CaX2	-1.66E-04	-4.79E-05	-1.66E-04	-1.67E-04	-5.51E-05	-1.34E-04
NaX	3.31E-04	9.58E-05	3.31E-04	3.34E-04	1.10E-04	2.69E-04

B (Regional) Spring 5.29 to R-37-2 Screen 4 9.5% uncertainty

Series >	B1	B2	B3	B4	B5	B6	B7	B8	B9	B10
Kaolinite				-1.90E-04		-3.46E-04	-2.33E-04		-3.46E-04	-7.11E-06
Smectite	-1.90E-04	-1.53E-02	-2.99E-03	-4.58E-05	-1.53E-02	-4.58E-05	-4.54E-05	-1.63E-04	-4.54E-05	-1.22E-04
Hematite	-4.53E-05	-4.75E-03	-9.23E-04		-4.78E-03			-3.66E-05		-2.39E-05
Chalcedony		-5.20E-02	-6.29E-03		-3.40E-02	-4.04E-04		-1.26E-04	-3.40E-04	
Pyroxene	1.96E-04		2.96E-03		1.51E-02		5.29E-05		5.29E-05	
Hornblende		6.03E-03		2.12E-05		2.13E-05		6.76E-05		5.15E-05
Plagioclase		3.95E-03	7.37E-04	2.53E-04	3.95E-03	4.86E-04	3.17E-04		4.86E-04	
Dacite glass	7.65E-04	5.10E-02	1.01E-02	2.51E-04	5.10E-02	2.51E-04	2.49E-04	6.42E-04	2.49E-04	5.06E-04
Calcite	2.60E-04	-1.31E-02			-9.83E-04	-1.53E-04	-5.33E-05	9.07E-05	-1.11E-04	1.19E-04
O2(g)	2.95E-05	2.98E-03	5.80E-04	1.02E-06	3.00E-03	1.02E-06	1.00E-06	2.40E-05	1.00E-06	1.60E-05
CO2(g)		1.35E-02	4.14E-04	4.14E-04	1.40E-03	5.67E-04	4.14E-04	3.23E-04	5.24E-04	2.95E-04
CaX2	-1.90E-04		-1.38E-04	-7.42E-05			1.07E-04	-1.69E-04		-1.66E-04
NaX	3.79E-04		2.75E-04	1.49E-04				3.38E-04		3.32E-04

C (Regional) Spring 5.29 to R-48 9.5% uncertainty

Series >	C1	C2	C3	C4	C5	C6	C7
Kaolinite				-1.89E-04	-1.81E-04	-2.72E-04	
Smectite	-3.44E-03	-1.20E-04	-1.95E-04	-3.66E-05	-3.66E-05	-3.66E-05	-2.96E-04
Hematite	-1.09E-03	-5.14E-05	-7.51E-05	-2.40E-05	-2.55E-05	-2.55E-05	-1.06E-04
Chalcedony	-7.32E-03					-1.79E-04	-6.04E-04
Pyroxene	3.42E-03		2.15E-04		5.83E-05	5.83E-05	
Hornblende		5.63E-05		2.23E-05			1.26E-04
Plagioclase	8.98E-04	3.13E-05	5.08E-05	2.91E-04	2.80E-04	4.16E-04	7.72E-05
Dacite glass	1.13E-02	2.79E-04	5.27E-04				8.65E-04
Calcite		1.53E-04	2.60E-04		9.11E-05		
O2(g)	6.84E-04	2.95E-05	4.43E-05	1.24E-05	1.32E-05	1.32E-05	6.39E-05
CO2(g)	3.52E-04	1.99E-04		3.52E-04	2.61E-04	3.52E-04	3.52E-04
CaX2	-1.64E-04	-2.01E-04	-2.01E-04	-9.40E-05	-1.13E-04	-6.82E-05	-1.99E-04
NaX	3.28E-04	4.03E-04	4.01E-04	1.88E-04	2.26E-04	1.37E-04	3.99E-04

D (Regional) Spring 5.29 to R-63 7% uncertainty

Series >	D1	D2	D3	D4	D5	D6
Kaolinite		-1.35E-04		-6.64E-05		
Smectite	-1.49E-04	-9.92E-05	-2.57E-04	-9.70E-05	-4.90E-04	-1.75E-03
Hematite	-6.75E-05	-5.08E-05	-1.10E-04	-4.88E-05	-1.95E-04	-6.64E-04
Chalcedony						-3.56E-03
Pyroxene		1.24E-04	2.89E-04		4.45E-04	1.85E-03
Hornblende	6.96E-05			4.82E-05		
Biotite					5.76E-05	
Plagioclase	7.89E-05	2.78E-04	1.08E-04	1.70E-04	3.29E-04	5.11E-04
Dacite glass	1.86E-04		5.49E-04		3.41E-04	5.50E-03
Calcite			1.44E-04			
O2(g)	3.85E-05	2.82E-05	6.39E-05	2.71E-05	1.16E-04	4.01E-04
CO2(g)	2.72E-04	2.72E-04		2.72E-04	2.72E-04	2.72E-04
CaX2	-8.52E-05		-8.77E-05	-6.27E-05	-2.46E-05	-5.60E-05
NaX	1.70E-04		1.76E-04	1.25E-04	4.92E-05	1.12E-04

E (Regional) Spring 5.29 to R-47 9% uncertainty

	E1	E2	E3	E4	E5	E6	E7
Kaolinite		-1.80E-04		-1.02E-04			
Smectite	-2.38E-04	-7.68E-05	-1.70E-04	-7.68E-05	-1.77E-04	-5.30E-04	-2.32E-03
Hematite	-1.01E-04	-4.11E-05	-7.39E-05	-4.02E-05	-7.64E-05	-2.16E-04	-8.75E-04
Chalcedony							-4.99E-03
Pyroxene	2.66E-04	9.80E-05				4.48E-04	2.45E-03
Hornblende			7.75E-05	3.88E-05	6.83E-05		
Biotite					2.00E-05	9.06E-05	
Plagioclase	9.24E-05	3.24E-04	7.43E-05	2.05E-04	1.29E-04	4.13E-04	6.49E-04
Dacite glass	5.37E-04		3.10E-04				7.48E-03
Calcite	1.67E-04						
O2(g)	5.87E-05	2.24E-05	4.25E-05	2.20E-05	4.40E-05	1.28E-04	5.29E-04
CO2(g)		3.06E-04	3.06E-04	3.06E-04	3.06E-04	3.06E-04	3.06E-04
CaX2	-1.20E-04	-2.79E-05	-1.21E-04	-6.88E-05	-1.02E-04	-3.11E-05	-8.39E-05
NaX	2.39E-04	5.58E-05	2.42E-04	1.38E-04	2.05E-04	6.22E-05	1.68E-04

F (Intermediate) CdV-16-4(i)p S1 to CdV-16-2(i)r 3.6% uncertainty

	F1	F2	F3	F4	F5
Kaolinite				-2.00E-05	
Smectite	-8.53E-05	-8.53E-05	-1.32E-04	-8.53E-05	-3.35E-04
Hematite	-1.53E-05	-1.55E-05	-3.27E-05	-1.55E-05	-1.08E-04
Chalcedony					-5.69E-04
Pyroxene	3.54E-05	6.06E-05	9.52E-05	6.06E-05	3.22E-04
Hornblende	1.00E-05				
Biotite			9.30E-06		
Plagioclase	6.96E-05	6.96E-05	1.07E-04	1.00E-04	1.36E-04
Dacite glass					8.33E-04
Calcite		2.00E-05			
O2(g)	1.10E-05	1.11E-05	2.15E-05	1.11E-05	6.75E-05
CO2(g)	2.98E-04	2.78E-04	2.98E-04	2.98E-04	2.98E-04
CaX2	-5.91E-05	-5.91E-05	-4.97E-05	-4.86E-05	-5.48E-05
NaX	1.18E-04	1.18E-04	9.94E-05	9.71E-05	1.10E-04

G (Intermediate) CdV-16-4(i)p to R-47i 3.5% uncertainty

	G1	G2	G3	G4	G5	G6	G7	G8
Kaolinite	-1.33E-04		-1.06E-04					
Smectite	-5.20E-05	-5.20E-05	-5.20E-05	-5.20E-05	-3.62E-04	-1.56E-04	-1.69E-04	-1.72E-03
Hematite	-7.65E-06	-7.65E-06	-7.33E-06	-7.33E-06	-1.22E-04	-4.51E-05	-4.96E-05	-6.27E-04
Chalcedony	-2.62E-04		-2.45E-04		-1.34E-04	-1.63E-04	-4.44E-04	-3.98E-03
Pyroxene	3.43E-05	3.43E-05			2.65E-04			1.78E-03
Hornblende			1.36E-05	1.36E-05		4.43E-05	6.21E-05	
Biotite					6.21E-05	2.08E-05		
Plagioclase	2.44E-04	3.99E-05	2.02E-04	3.99E-05	2.89E-04	1.23E-04	7.11E-05	4.86E-04
Dacite glass							3.90E-04	5.56E-03
Calcite		1.33E-04		1.06E-04				
O2(g)	5.92E-06	5.92E-06	5.76E-06	5.76E-06	7.56E-05	2.88E-05	3.16E-05	3.83E-04
CO2(g)	3.43E-04	2.10E-04	3.43E-04	2.37E-04	3.43E-04	3.43E-04	3.43E-04	3.43E-04
CaX2	-7.55E-05	-1.46E-04	-8.98E-05	-1.46E-04	-8.32E-05	-1.25E-04	-1.44E-04	-1.17E-04
NaX	1.51E-04	2.92E-04	1.80E-04	2.92E-04	1.66E-04	2.50E-04	2.88E-04	2.34E-04

H (Intermediate) R-26 S1 to CdV-16-1(i) 16% uncertainty

	H1	H2	H3	H4	H5	H6
Kaolinite	-1.13E-04	-1.52E-05				
Smectite				-4.26E-04	-1.61E-06	
Hematite	-1.27E-04	-1.01E-04	-1.01E-04	-6.03E-04	-1.03E-04	-1.01E-04
Chalcedony	-6.88E-04			-2.17E-03		
Pyroxene	1.70E-04	1.35E-04	1.35E-04	9.31E-04	1.38E-04	1.35E-04
Plagioclase	1.98E-04	2.88E-05		2.69E-04	4.16E-06	2.42E-06
Rhyolite glass			1.39E-05	1.13E-03		
Calcite		9.85E-05	1.31E-04		1.02E-04	1.30E-04
O2(g)	6.36E-05	5.07E-05	5.07E-05	3.18E-04	5.16E-05	5.07E-05
CO2(g)						
CaX2	5.15E-05		-4.95E-05	4.94E-05		-4.90E-05
NaX	-1.03E-04		9.90E-05			9.81E-05

I (Intermediate) R-26 S1 to R-25b 19% uncertainty

	I1	I2	I3	I4	I5
Kaolinite			-9.94E-05	-2.51E-04	-1.00E-04
Smectite	-1.19E-04	-8.38E-04			-3.02E-05
Hematite	-1.13E-04	-9.86E-04			
Chalcedony		-3.62E-03		-8.26E-04	
Pyroxene	1.87E-04	1.57E-03	1.45E-06	1.45E-06	1.05E-05
Plagioclase	1.36E-04	5.91E-04	1.79E-04	4.43E-04	2.13E-04
Rhyolite glass		1.88E-03			
Calcite					
O2(g)	6.15E-05	5.27E-04	4.69E-07	4.69E-07	1.68E-06
CO2(g)	5.41E-04	5.41E-04	5.41E-04	5.41E-04	5.41E-04
CaX2	-2.85E-05		-3.73E-05		
NaX	5.69E-05		7.47E-05		

J (Intermediate) R-26 PZ2 to Burning Ground Spring, 35% uncertainty

	J1	J2	J3	J4	J5	J6	J7	J8
Smectite	-7.82E-05	-7.01E-05	-5.60E-05	-1.69E-05	-3.58E-05		-3.58E-05	
Hematite	-2.50E-05	-3.86E-05				-1.96E-05		-3.72E-05
Chalcedony	-1.21E-04		-2.75E-05					
Pyroxene	6.02E-05	7.59E-05	2.03E-05	8.52E-06	1.42E-05	2.96E-05	1.42E-05	5.31E-05
Plagioclase	4.68E-05	9.24E-05	3.24E-05		2.02E-05		5.51E-05	
Rhyolite glass	3.13E-04		2.57E-04	1.99E-04	2.01E-04	9.32E-05		
O2(g)	1.67E-05	2.32E-05	3.34E-06	1.77E-06	2.53E-06	1.09E-05	2.53E-06	1.97E-05

L (Intermediate) 16-26644 to Martin Spring, 7% uncertainty

	L1	L2	L3	L4	L5	L6	L7	L8	L9	L10
Kaolinite	-3.91E-04	-3.97E-04			-6.25E-06		-1.92E-05			
Smectite	-1.19E-05		-1.67E-06		-1.19E-05			-1.74E-05	-1.44E-03	-1.63E-05
Chalcedony	-1.14E-03	-1.12E-03							-6.00E-03	
Plagioclase	7.05E-04	7.03E-04			3.65E-05	1.24E-05	4.58E-05	3.16E-05	9.58E-04	2.85E-05
Hematite	-2.70E-05	-1.27E-05	-1.46E-05	-1.27E-05	-2.70E-05	-1.27E-05	-1.27E-05	-3.40E-05	-1.64E-03	-3.19E-05
Pyroxene	4.28E-05	2.03E-05	2.33E-05	2.03E-05	4.28E-05	2.03E-05	2.03E-05	5.39E-05	2.62E-03	5.07E-05
O2(g)	1.41E-05	6.50E-06	7.51E-06	6.50E-06	1.41E-05	6.50E-06	6.50E-06	1.78E-05	8.75E-04	1.67E-05
CO2(g)	9.82E-04	9.82E-04	5.77E-04	5.77E-04	5.97E-04	5.84E-04	6.04E-04	5.94E-04	9.91E-04	5.92E-04
Calcite	9.07E-05	9.08E-05	4.95E-04	4.95E-04	4.75E-04	4.88E-04	4.69E-04	4.79E-04	8.14E-05	4.80E-04
CaX2			-2.99E-04	-2.99E-04	-2.84E-04	-2.94E-04	-2.79E-04	-2.87E-04		-2.88E-04
NaX			5.98E-04	5.98E-04	5.69E-04	5.87E-04	5.59E-04	5.74E-04		5.76E-04
Rhyolite glass			7.25E-05	6.27E-05					3.57E-03	1.10E-05

Phase I inverse mixing models (Cl^- mass balance errors in mg/L)

M Inverse mixing models for the Otowi Member at CdV-16-1(i)

model (Cl error) >	**M1 (0.12)**	**M2 (1.73)**	**M3 (1.5)**
R-26 S1	0.75	0.83	0.82
alluvial	0.25	0.17	0.18
16-1(i)	1	1	1
Smectite	-9.50E-05	-1.59E-05	-1.94E-05
Chalcedony	-5.16E-04	-3.03E-04	-3.19E-04
Plagioclase	5.10E-05		
Hematite	-2.26E-04	-1.51E-04	-1.56E-04
Rhyolite glass	1.53E-04	5.90E-06	2.09E-05
Pyroxene	3.24E-04	2.01E-04	2.10E-04
O2(g)	1.16E-04	7.53E-05	7.84E-05
CO2(g)	3.71E-04	3.31E-04	3.24E-04
Calcite		8.62E-05	8.69E-05

N Inverse mixing models for the Otowi Member at R-25b (Cl^- mass balance error in mg/L)

model (Cl error) >	N1 (1.9)	N2 (1.04)	N3 (1.04)	N4 (0.73)	N5 (3.92)	N6 (0.05)	N7 (0.73)	N8 (3.92)	N9 (0.73)
16-26644	0	0.11	0.11	0.01	0.27	0.05	0.01	0.27	0.01
alluvial	0.13	0	0	0	0	0	0	0	0
R-26 S1	0.87	0.89	0.89	0.99	0.73	0.95	0.99	0.73	0.99
R-25b	1	1	1	1	1	1	1	1	1
Kaolinite		-1.82E-04	-1.82E-04	-2.03E-04					
Smectite	-7.14E-05	-9.85E-05	-9.85E-05	-8.79E-05	-6.99E-05	-8.46E-04	-8.31E-04	-6.99E-05	-8.79E-05
Pyroxene	1.06E-04	2.18E-04	2.18E-04	2.16E-04	1.02E-04	1.57E-03	1.55E-03	1.02E-04	2.16E-04
Plagioclase	6.97E-05	4.27E-04	4.27E-04	4.55E-04	7.81E-05	5.97E-04	5.86E-04	7.81E-05	1.02E-04
Rhyolite glass						1.88E-03	1.86E-03		
Chalcedony		-9.60E-04	-9.60E-04	-1.05E-03		-3.61E-03	-3.58E-03		-4.53E-04
Hematite	-6.51E-05	-1.40E-04	-1.40E-04	-1.41E-04	-5.99E-05	-9.88E-04	-9.77E-04	-5.99E-05	-1.41E-04
O2(g)	3.54E-05	7.46E-05	7.46E-05	7.46E-05	3.31E-05	5.28E-04	5.22E-04	3.31E-05	7.46E-05
CO2(g)	4.74E-04	6.81E-04	6.81E-04	7.08E-04	4.55E-04	7.04E-04	7.12E-04	4.55E-04	5.05E-04
CaX2	-1.42E-04				-1.29E-04			-1.29E-04	-1.50E-04
NaX	2.83E-04				2.57E-04			2.57E-04	3.00E-04
Calcite	1.82E-04			1.44E-05	1.59E-04		9.63E-06	1.59E-04	2.18E-04

O Inverse mixing model results for the Puye Formation at CdV-16-2(i)r (Cl^- mass balance error in mg/L)

model (Cl error) >	O1 (0.91)	O2 (0.91)	O3 (0.91)	O4 (0.91)	O5 (1.39)	O6 (0.91)
16-4(i)p S1	1	1	1	1	0.85	1
16-1(i)	0	0	0	0	0.15	0
16-2(i)r	1	1	1	1	1	1
Kaolinite						-2.00E-05
Smectite	-3.35E-04	-8.53E-05	-8.53E-05	-1.32E-04	-1.12E-04	-8.53E-05
Pyroxene	3.22E-04	3.54E-05	6.06E-05	9.52E-05	7.50E-05	6.06E-05
Plagioclase	1.36E-04	6.96E-05	6.96E-05	1.07E-04	9.69E-05	1.00E-04
Hematite	-1.08E-04	-1.53E-05	-1.55E-05	-3.27E-05	-1.76E-05	-1.55E-05
Hornblende		1.00E-05				
Dacite glass	8.33E-04					
O2(g)	6.75E-05	1.10E-05	1.11E-05	2.15E-05	1.32E-05	1.11E-05
Chalcedony	-5.69E-04					
CO2(g)	2.98E-04	2.98E-04	2.78E-04	2.98E-04	2.51E-04	2.98E-04
CaX2	-5.48E-05	-5.91E-05	-5.91E-05	-4.97E-05	-4.78E-05	-4.86E-05
NaX	1.10E-04	1.18E-04	1.18E-04	9.94E-05	9.56E-05	9.71E-05
Calcite			2.00E-05			
Biotite				9.30E-06		

P Inverse mixing models for the Puye Formation at R-47i (Cl^- mass balance error in mg/L)

model (Cl error) >	**P1 (1.74)**	**P2 (3.86)**	**P3 (3.45)**	**P4 (3.19)**
16-4(i)p S1	0.51	0.81	0.83	0.85
16-1(i)	0.49	0.0	0.0	0.0
alluvial	0.0	0.19	0.17	0.15
R-47i	1	1	1	1
Kaolinite				-7.83E-05
Smectite	-1.30E-04	-1.29E-04	-1.03E-04	-1.00E-04
Pyroxene		9.00E-05		3.48E-05
Hornblende	2.08E-05		1.43E-05	
Plagioclase	1.19E-04	9.67E-05	7.56E-05	1.93E-04
Hematite		-2.57E-05		
O2(g)	5.23E-06	1.74E-05	3.59E-06	3.52E-06
CaX2	-1.11E-04	-6.85E-05	-7.90E-05	-7.00E-05
NaX	2.22E-04	1.37E-04	1.58E-04	1.40E-04

Phase II Mixing Models

Q: Inverse mixing models for upper intermediate groundwater at CdV-16-4(i)p S1 with (Cl^- mass balance error in mg/L)

model (Cl error) >	Q1 (2.14)	Q2 (2.14)	Q3 (2.94)	Q4 (1.59)	Q5 (2.28)	Q6 (7.26)	Q7 (0.79)	Q8 (4.16)	Q9 (1.83)
5.29 spring	0.141	0.136	0	0	0.802	0.492	0.870	0.661	0.789
R-26 S1	0.859	0.864	0.724	0.797	0	0	0	0	0
BG Spring	0	0	0.276	0.203	0	0.508	0	0.339	0.212
alluvial aq.	0	0	0	0	0.198	0	0.130	0	0
16-4ip S1	1	1	1	1	1	1	1	1	1
Smectite	-6.88E-05	-6.91E-05	-1.28E-04	-1.01E-04	-1.55E-04	-1.72E-04	-1.13E-04	-1.55E-04	-1.17E-04
Pyroxene	2.70E-05		4.92E-05		2.01E-04			1.68E-04	
Hornblende		1.08E-05		1.57E-05		2.56E-05	4.60E-05		4.42E-05
Dacite glass						2.43E-04			
Plagioclase	7.70E-05	7.44E-05	1.28E-04	1.04E-04	1.23E-04	1.08E-04	8.47E-05	1.36E-04	9.93E-05
Hematite					-8.53E-05		-4.42E-05	-6.33E-05	-3.87E-05
O2(g)	2.67E-06	2.61E-06	4.83E-06	3.82E-06	4.72E-05	5.76E-06	2.51E-05	3.67E-05	2.29E-05
CaX2						-2.91E-05			
NaX						5.82E-05			

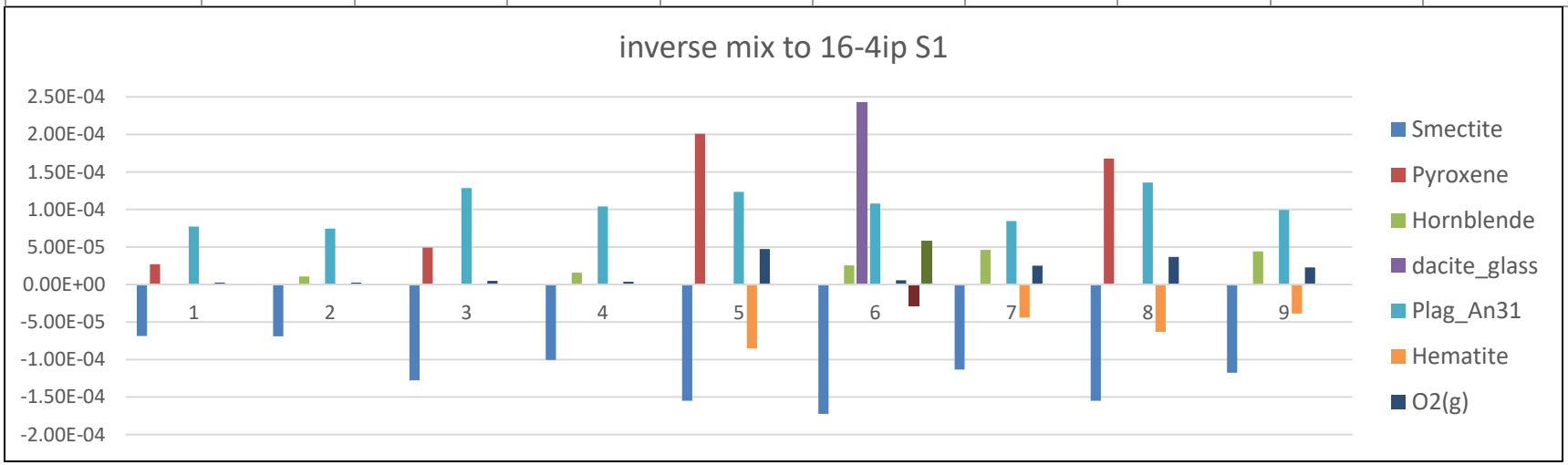

R: Inverse mixing models for intermediate groundwater at CdV-9-1(i) with (Cl^- mass balance error in mg/L)

model (Cl error) >	R1 (1.5)	R2 (5.34)	R3 (2.01)	R4 (5.54)	R5 (3.79)	R6 (1.19)	R7 (0.66)	R8 (1.43)
5.29 Spring	0.49	0.18	0.36	0	0	0.61	0	0
R-26-S1	0	0	0	0.17	0.27	0	0.53	0.62
BG Spring	0	0.82	0.64	0.83	0.73	0	0	0
alluvial aq.	0.51	0	0	0	0	0.39	0.47	0.38
CdV-9-1i	1	1	1	1	1	1	1	1
Kaolinite			-1.26E-04					
Smectite	-2.27E-04	-1.63E-04	-1.25E-04	-1.74E-04	-1.54E-04	-1.65E-04	-2.28E-04	-1.60E-04
Pyroxene	2.28E-04		4.60E-05	6.62E-05			2.06E-04	
Hornblende		2.45E-05			2.36E-05	6.74E-05		4.55E-05
Plagioclase	1.65E-04	1.40E-04	2.94E-04	1.55E-04	1.37E-04	1.09E-04	1.76E-04	1.21E-04
Hematite	-8.93E-05					-6.63E-05	-7.45E-05	-3.48E-05
O2(g)	5.18E-05	5.80E-06	4.25E-06	6.46E-06	5.75E-06	3.81E-05	4.52E-05	2.29E-05
CaX2	-9.13E-05	-1.78E-04	-1.43E-04	-1.37E-04	-1.57E-04	-1.85E-04	-7.70E-05	-1.27E-04
NaX	1.83E-04	3.57E-04	2.85E-04	2.75E-04	3.15E-04	3.69E-04	1.54E-04	2.54E-04

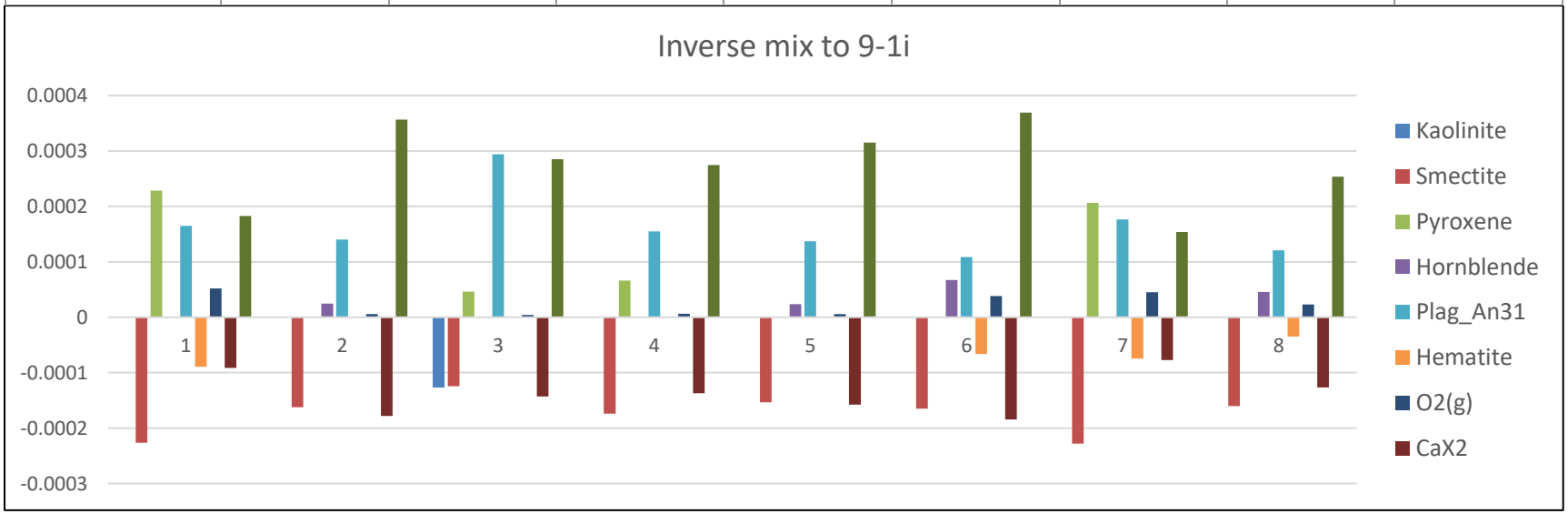

S: Inverse mixing models for lower intermediate groundwater at CdV-16-4(i)p S2 (Cl^- mass balance error in mg/L)

model (Cl error) >	S1 (0.73)	S2 (0.77)	S3 (0.48)	S4 (0.13)	S5 (0.23)	S6 (0.57)	S7 (0.58)	S8 (0.08)
5.29 Spring	0.73	0.34	0.95	0.96	0.98	0.99	0.93	0.97
R-26 S1	0.27	0.66	0	0	0	0	0	0
BG Spring	0	0	0	0	0	0.01	0.07	0.03
alluvial aq.	0	0	0.05	0.04	0.02	0	0	0
CdV-9-1(i)	0	0	0	0	0	0	0	0
CdV 16-4ipS2	1	1	1	1	1	1	1	1
Kaolinite			-1.47E-04			-1.73E-04		
Smectite	-1.26E-04	-1.59E-04	-1.20E-04	-1.18E-04	-4.76E-04	-1.04E-04	-1.18E-04	-4.64E-04
Pyroxene		1.82E-04	1.33E-04		3.98E-04	1.22E-04		3.89E-04
Hornblende	5.67E-05			5.77E-05			5.52E-05	
Biotite					7.32E-05			7.07E-05
Plagioclase	1.10E-04	1.52E-04	3.18E-04	9.27E-05	3.80E-04	3.46E-04	9.64E-05	3.72E-04
Hematite	-5.21E-05	-6.71E-05	-5.05E-05	-5.68E-05	-1.83E-04	-4.68E-05	-5.25E-05	-1.78E-04
O2(g)	3.10E-05	4.02E-05	2.95E-05	3.25E-05	1.10E-04	2.71E-05	3.05E-05	1.07E-04
CaX2	-7.84E-05			-8.93E-05			-9.08E-05	
NaX	1.57E-04			1.79E-04			1.82E-04	

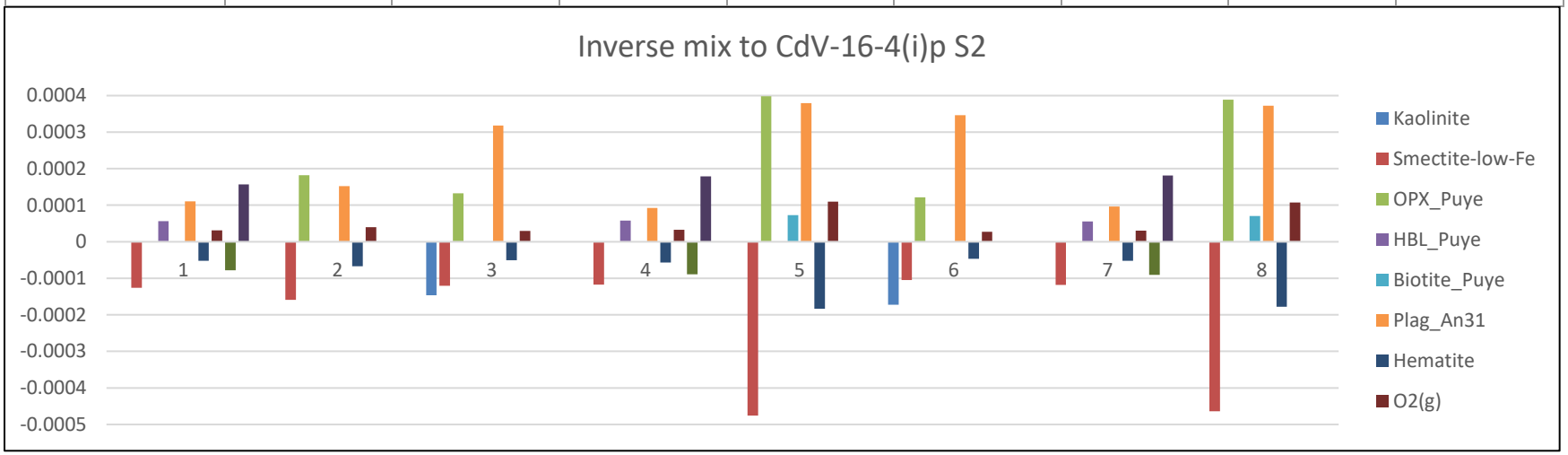

T: Inverse mixing models for regional groundwater at R-63 with (Cl^- mass balance error in mg/L)

model (Cl error) >	T1 (2.58)	T2 (1.53)	T3 (1.53)	T4 (1.14)	T5 (1.14)	T6 (1.14)	T7 (1.53)	T8 (3.61)
5.29 Spring	0.89	0.92	0.92	0.95	0.95	0.95	0.92	0.81
R-26 S1	0	0	0	0	0	0	0	0
BG Spring	0	0.08	0.08	0	0	0	0.08	0.19
alluvial aq	0.11	0	0	0.05	0.05	0.05	0	0
R-63	1	1	1	1	1	1	1	1
Kaolinite		-1.08E-04			-1.10E-04			
Smectite	-2.90E-04	-1.16E-04	-1.16E-04	-4.17E-04	-1.14E-04	-1.14E-04	-3.85E-04	-2.86E-04
Pyroxene	3.16E-04	1.25E-04		3.84E-04	1.25E-04		3.59E-04	3.04E-04
Hornblende			5.72E-05			5.89E-05		
Biotite				6.00E-05			5.21E-05	
Dacite glass	5.13E-04							4.84E-04
Plagioclase	1.42E-04	2.51E-04	8.68E-05	3.27E-04	2.49E-04	8.19E-05	3.07E-04	1.51E-04
Hematite	-1.19E-04	-4.75E-05	-5.74E-05	-1.79E-04	-4.90E-05	-6.08E-05	-1.65E-04	-1.12E-04
O2(g)	6.97E-05	2.72E-05	3.21E-05	1.05E-04	2.77E-05	3.37E-05	9.67E-05	6.61E-05
CaX2			-5.68E-05			-5.32E-05		
NaX			1.14E-04			1.07E-04		

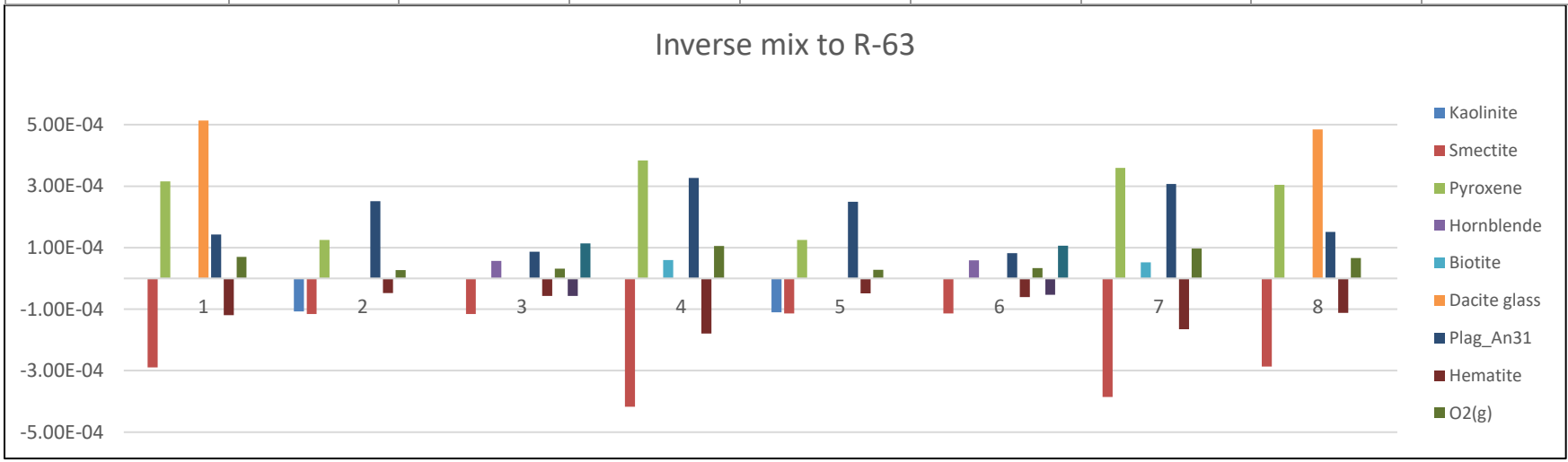

U: Inverse mixing models for regional groundwater at R-18 with (Cl^- mass balance error in mg/L)

model (Cl error) >	U1 (0.09)	U2 (1.26)	U3 (1.71)	U4 (1.26)	U5 (1.71)
5.29 Spring	0.81	0.95	0.91	0.95	0.91
R-26 S1	0.19	0	0	0	0
BG Spring	0	0	0.09	0	0.09
alluvial aq	0	0.05	0	0.05	0
R-18	1	1	1	1	1
Smectite	-1.98E-05	-4.45E-04	-1.06E-04	-1.08E-04	-4.28E-04
Pyroxene		3.87E-04			3.70E-04
Hornblende	2.94E-05		5.65E-05	5.85E-05	
Biotite		7.61E-05			7.23E-05
Calcite	9.83E-05				
Plagioclase		3.39E-04	7.83E-05	7.63E-05	3.30E-04
Hematite	-3.85E-05	-1.88E-04	-5.78E-05	-6.12E-05	-1.78E-04
O2(g)	1.94E-05	1.11E-04	3.23E-05	3.39E-05	1.05E-04
CaX2	-9.10E-05		-7.11E-05	-6.81E-05	
NaX	1.82E-04		1.42E-04	1.36E-04	

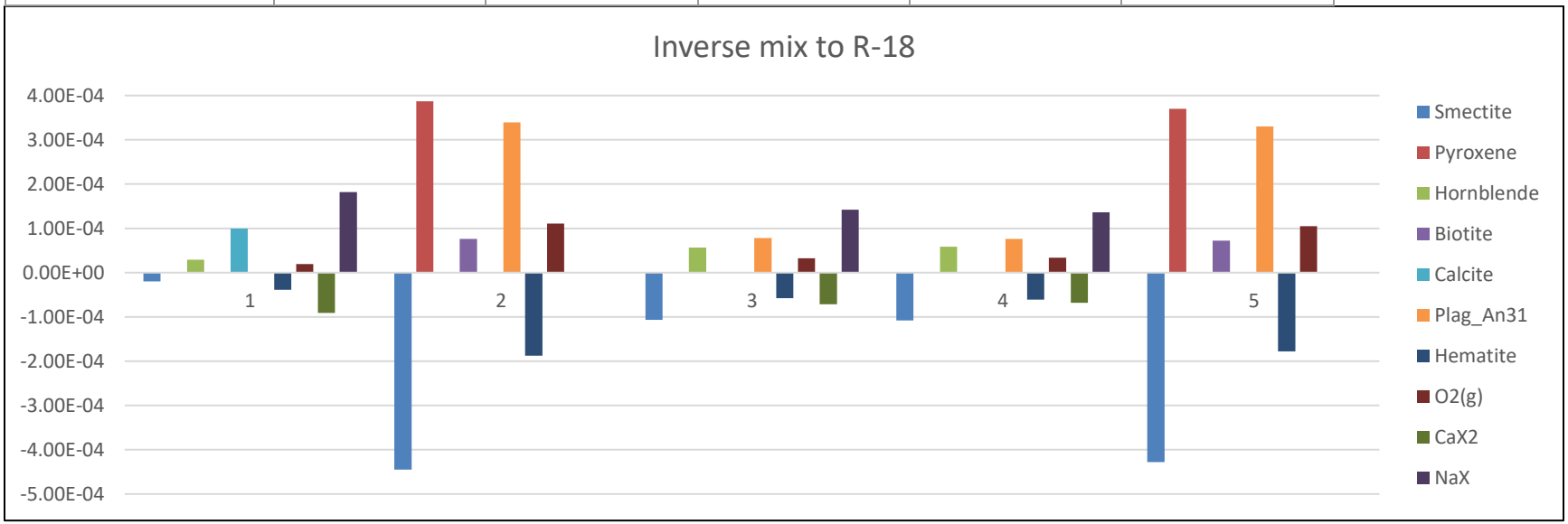

7.2 Supplementary Materials – part c

Reactions and calculations

Some reactions relied upon:

An_34 plagioclase dissolution:

$Na_{0.66}Ca_{0.34}Al_{1.34}Si_{2.66}O_8 + 5.36\ H^+ = 0.66\ Na^+ + 0.34\ Ca^{+2} + 1.34\ Al^{+3} + 2.66\ SiO_2 + 2.68\ H_2O$

Orthopyroxene dissolution:

$Mg_{0.91}Fe_{1.09}Si_2O_6 + 4\ H^+ = 2\ H_2O + 0.91\ Mg^{2+} + 1.09\ Fe^{2+} + 2\ SiO_2$

Hornblende dissolution:

$Ca_2Mg_{2.28}Fe_{2.72}Si_8O_{22}(OH)_2 + 14.0\ H^+ = 2.0\ Ca^{2+} + 2.28\ Mg^{2+} + 2.72\ Fe^{2+} + 8.0\ H_2O + 8.0\ SiO_2$

Dacite glass dissolution:

$K_{0.06}SiAl_{0.27}O_2(OH)_{0.87} + 0.87\ H^+ = 0.87\ H_2O + SiO_2 + 0.27\ Al^{3+} + 0.06\ K^+$

Calcite dissolution: $1.0\ CaCO_3 + 1.0\ H^+ = 1.0\ Ca^{2+} + 1.0\ HCO3^-$

CO_2 dissolution: $1.0\ CO_2 + 1.0\ H_2O = 1.0\ HCO_3^- + 1.0\ H^+$

Hematite precipitation: $2.0\ Fe^{3+} + 3.0\ H_2O = Fe_2O_3 + 6.0\ H^+$

Kaolinite precipitation: $2.0\ Al^{3+} + 2.0\ SiO_2 + 5.0\ H_2O = Al_2Si_2O_5(OH)_4 + 6.0\ H^+$

Smectite precipitation:

$0.02\ Ca^{2+} + 0.15\ Na^+ + 0.16\ Fe^{3+} + 0.2\ K^+ + 0.29\ Fe^{2+} + 0.9\ Mg^{2+} + 1.25\ Al^{3+} + 3.75\ SiO_2 + 4.5\ H_2O = Ca_{.02}Na_{.15}K_{.2}Fe^{2+}{}_{.29}Fe^{3+}{}_{16}Mg_{.9}Al_{1.25}Si_{3.75}H_2O\ 1 + 7.0\ H^+$

Plagioclase specification:

In the Cerro Grande dacite, Broxton et al (2007) put the range of plagioclase compositions at between An44 and An56. An-number is typically used to characterize plagioclase compositions, and is calculated as the molar ratio of {Ca : (Ca + Na)} (Bowser and Jones, 2002).

For models of regional recharge, the mean of molar Ca/Na ratios, 0.51, is used as a starting point. Coupled substitution is employed to arrive at a balanced dissolution equation for use in PHREEQC, beginning with the albite equation from llnl.dat, and albite and anorthite pure phase formulae. Silicon and aluminum subscripts are scaled to proportion between their albite and anorthite values. Finally, hydrogen and water coefficients are adjusted to satisfy charge and mass balance.

$NaAlSi_3O_8 + 4\ H^+ = 1\ Al^{3+} + 1\ Na^+ + 2\ H_2O + 3\ SiO_2$ (llnl.dat) $NaAlSi_3O_8 - CaAl_2Si_2O_8$

Ca = 0.51*Na Na + Ca = 1 Na + 0.51*Na = 1 1.51 Na =1 Na = 1/1.51 = 0.66 Ca = 0.34

Si: albite (0.66 x 3) + anorthite (0.34 x 2) = 1.98 + 0.68 = 2.66

Al: albite (0.66 x 1) + anorthite (0.34 x 2) = 0.66 + 0.68 = 1.34

An_34 plagioclase dissolution reaction (Plag_Tschi):

$Na_{0.66}Ca_{0.34}Al_{1.34}Si_{2.66}O_8 + 5.36\ H^+ = 0.66\ Na^+ + 0.34\ Ca^{+2} + 1.34\ Al^{+3} + 2.66\ SiO_2 + 2.68\ H_2O$

In the Puye Formation at R-25, the mean molar Ca/Na ratio is 0.45:

Ca = 0.45*Na Na + Ca = 1 Na + 0.45*Na = 1 1.45 Na =1 Na = 1/1.45 = 0.69 Ca = 0.31

Si: albite (0.69 x 3) + anorthite (0.31 x 2) = 2.07 + 0.62 = 2.69

Al: albite (0.69 x 1) + anorthite (0.31 x 2) = 0.69 + 0.62 = 1.31

An_31 plagioclase balanced dissolution reaction (Plag_Puye):

$Na_{0.69}Ca_{0.31}Al_{1.31}Si_{2.69}O_8 + 5.24\ H^+ = 0.69\ Na^+ + 0.31\ Ca^{+2} + 1.31\ Al^{+3} + 2.69\ SiO_2 + 2.62\ H_2O$

The mean ratio of molar Ca/Na in the Cerro Toledo Formation + Otowi Member at R-25 is 0.18:

Ca = 0.18 Na Na + Ca = 1 Na + 0.18 Na = 1 1.18 Na = 1 Na = 1/ 1.18 = 0.85 Ca = 0.15

Si: albite (0.85 x 3) + anorthite (0.15 x 2) = 2.55 + 0.3 = 2.85

Al: albite (0.85 x 1) + anorthite (0.15 x 2) = 0.85 + 0.3 = 1.15

An_15 plagioclase balanced dissolution reaction (Plag_CT-Otowi): this would be minor

$Na_{0.85}Ca_{0.15}Al_{1.15}Si_{2.85}O_8 + 4.6\ H^+ = 0.85\ Na^+ + 0.15\ Ca^{+2} + 1.15\ Al^{+3} + 2.85\ SiO_2 + 2.3\ H_2O$

Orthopyroxene specification:

In the Tschicoma Formation dacite, the mean molar ratio of iron to magnesium, is 1.19.

$MgSiO_3 + 2\ H^+ = H_2O + Mg^{2+} + SiO_2$ (llnl.dat) $MgSiO_3 - FeSiO_3$

$1.19\ Mg = Fe$ and $Fe + Mg = 1 \rightarrow Fe = 1 - Mg$

$1.19\ Mg = 1 - Mg \rightarrow 1.19\ Mg + Mg = 1 \rightarrow 2.19\ Mg = 1 \rightarrow Mg = 1/2.19$

$Mg = 0.457$ $Fe = 1 - 0.457$ $Fe = 0.543$

$(Mg_{0.457}Fe_{0.543})_2Si_2O_6 \rightarrow (Mg_{0.91}Fe_{1.09})Si_2O_6$

Orthopyroxene dissolution reaction (OPX_Tschi):

$Mg_{0.91}Fe_{1.09}Si_2O_6 + 4\ H^+ = 2\ H_2O + 0.91\ Mg^{2+} + 1.09\ Fe^{2+} + 2\ SiO_2$

The Fe/Mg ratio for the Puye Formation at R-25 is 1.3:

$1.3\ Mg = Fe$ $Fe + Mg = 1$ $Fe = 1 - Mg$ $1.3\ Mg = 1 - Mg$ $2.3\ Mg = 1$

$Mg = 1/2.3$ $Mg = 0.43$ $Fe = 1 - 0.43 = 0.57$

$(Mg_{0.43}Fe_{0.57})_2Si_2O_6 \rightarrow (Mg_{0.86}Fe_{1.14})Si_2O_6$

Orthopyroxene dissolution reaction (OPX_Puye):

$Mg_{0.86}Fe_{1.14}Si_2O_6 + 4\ H^+ = 2\ H_2O + 0.86\ Mg^{2+} + 1.14\ Fe^{2+} + 2\ SiO_2$

For the Cerro Toledo and Otowi, where molar $Fe/Mg = 3 \rightarrow$ $Mg = 0.25$; $Fe = 0.75$

$Mg_{0.5}Fe_{1.5}Si_2O_6 + 4\ H^+ = 2\ H_2O + 0.5\ Mg^{2+} + 1.5\ Fe^{2+} + 2\ SiO_2$ (OPX_CT-Otowi)

Hornblende specification:

$Ca_2(Fe, Mg)_5Si_8O_{22}(OH)_2$ general formula for hornblende

In the dacite whole rock, molar Fe/Mg is 1.19 Fe + Mg = 5 1.19 Mg = Fe

Fe = 5 – Mg 1.19 Mg = 5 – Mg → 1.19 Mg + Mg = 5 → 2.19 Mg = 5 → Mg = 5/2.19

Mg = 2.28 Fe = 5 – 2.28 = 2.72

Hornblende dissolution reaction (Hbl_Tschi):

$Ca_2Mg_{2.28}Fe_{2.72}Si_8O_{22}(OH)_2 + 14.0\ H^+ = 2.0\ Ca^{2+} + 2.28\ Mg^{2+} + 2.72\ Fe^{2+} + 8.0\ H_2O + 8.0\ SiO_2$

For the Puye Formation:

Fe = 5 – Mg 1.3 Mg = 5 – Mg → 1.3 Mg + Mg = 5 → 2.3 Mg = 5 → Mg = 5/2.3

Mg = 2.17 Fe = 5 – 2.17 = 2.83

Hornblende dissolution reaction (Hbl_Puye):

$Ca_2Mg_{2.17}Fe_{2.83}Si_8O_{22}(OH)_2 + 14.0\ H^+ = 2.0\ Ca^{2+} + 2.17\ Mg^{2+} + 2.83\ Fe^{2+} + 8.0\ H_2O + 8.0\ SiO_2$

Biotite specification:

Annite $KFe_3AlSi_3O_{10}(OH)_2 + 10.0\ H^+ = 1.0\ Al^{3+} + 1.0\ K^+ + 3.0\ Fe^{2+} + 3.0\ SiO_2 + 6.0\ H_2O$ (llnl.dat)

Molar Fe/Mg in Puye = 1.31 Fe = 1.31 Mg Fe + Mg = 3 1.31Mg + Mg = 3

2.31Mg = 3 Mg = 3/2.31 Mg = 1.30 Fe = 3 – 1.3 Fe = 1.7

Biotite dissolution reaction (Biotite_Puye):

$KFe_{1.7}Mg_{1.3}AlSi_3O_{10}(OH)_2 + 10.0\ H^+ = 1.0\ Al^{3+} + 1.0\ K^+ + 1.7\ Fe^{2+} + 1.3\ Mg^{2+} + 3.0\ SiO_2 + 6.0\ H_2O$

Silica dissolution from hydrated volcanic glass - notes

From the mean of 9 dacite samples in the Cerro Grande and Pajarito Mt. dacites, the average molar Al/Si ratio is 0.27. A specific formula starts with the following dissolution reaction for hydrated dacite glass and adapts it for aqueous silica as used in the llnl.dat database:

$SiAl_{0.27}O_2(OH)_{0.81} + 0.81\ H^+ + 1.19\ H_2O = H_4SiO_4 + 0.27Al^{3+}$ (Wolff-Boenisch et al., 2004)

$H_4SiO_4 = SiO_2 + 2H_2O$

$SiAl_{0.27}O_2(OH)_{0.81} + 0.81\ H^+ = 0.81\ H_2O + SiO_2 + 0.27\ Al^{3+}$

Tschicoma and Puye Formations:

$K_{0.06}SiAl_{0.27}O_2(OH)_{0.87} + 0.87\ H^+ = 0.87\ H_2O + SiO_2 + 0.27\ Al^{3+} + 0.06\ K^+$ (dacite glass with K)

In the Otowi Member of the Bandelier Tuff the molar ratio of Al to Si is closer to 0.2. There is more potassium (between 3 and 4 wt%) and though feldspars compositions are predominantly K-Feldspar, volcanic glass appears to contain K as well. In the corehole SHB_3, electron microprobe analyses from Cerro Toledo and Otowi glasses have potassium at 4 wt% or more (geo report citation). Water in these zones is supersaturated with respect to K-Feldspar and sanidine, suggesting that K contribution to the fluid derives from a more soluble phase. For this reason, potassium is again linked to glass, according to the K/Si molar ratio of 0.08:

$SiAl_{0.2}O_2(OH)_{0.61} + 0.61\ H^+ + 1.39\ H_2O = H_4SiO_4 + 0.2\ Al^{3+}$ log k = - 0.55
(Wolff-Boenisch et al., 2004)

$H_4SiO_4 = SiO_2 + 2\ H_2O$

$K_{0.08}SiAl_{0.2}O_2(OH)_{0.68} + 0.68\ H^+ = 0.2\ Al^{3+} + SiO_2 + 0.68\ H_2O + 0.08\ K^+$ (rhyolite glass w/ K)

LA-UR-17-20375
January 2017
EP2016-0114

2016 Update of the TA-16 RDX Inventory Report

Prepared by the Associate Directorate for Environmental Management

CONTENTS

Figures

Tables

Appendixes

1.0 INTRODUCTION

Wastewater from the machining of high explosives (HE) was produced at Technical Area 16 (TA-16) at Los Alamos National Laboratory (LANL or the Laboratory) over several decades, much of which was discharged at the surface through Consolidated Unit 16-021(c)-99, the 260 Outfall. Although other types of HE, including HMX (octahydro-1,3,5,7-tetranitro-1,3,5,7-tetrazocine); TNT (2,4,6-trinitrotoluene); and TATB (triaminotrinitrobenzene), were released at the Outfall, the primary component was RDX (hexahydro-1,3,5-trinitro-1,3,5-triazine). This report focuses on RDX, although the term HE is used when the discussion refers to bulk HE (i.e., multiple HE types). RDX is characterized as toxic, potentially carcinogenic, and environmentally stable in the absence of light. It is also known to be mobile in the subsurface (EPA 2014, 601836, p. 2). A 2005 inventory study estimated the quantity and distribution of RDX in soil, the vadose zone above perched-intermediate groundwater, perched-intermediate groundwater, and the regional aquifer at TA-16 based upon limited data available (LANL 2006, 093798). This report is intended to update those estimates with more extensive and recent data.

TA-16 is located near the western edge of the Pajarito Plateau on a mesa where alluvial fan deposits overlie a thick mostly unsaturated interval of Bandelier Tuff (Figure 1). To the west are the Pajarito fault and the Jemez Mountains. Below the HE outfall, a settling pond area leads to a steep lower channel that drains into the adjacent Cañon de Valle. Relatively persistent shallow saturation in and beneath these source areas, especially during the period of outfall operation, allowed percolation and downward transport of RDX through the vadose zone to groundwater, as detailed in various site conceptual models (LANL 2003, 077965; Birdsell et al. 2005, 092048; Newman et al. 2007, 095632). Note that for this report, the vadose zone refers to the primarily unsaturated region between the mesa top and the top of perched-intermediate groundwater at TA-16, or the primarily unsaturated region below the bottom of the Cañon de Valle alluvial aquifer and the top of perched-intermediate groundwater below the canyon. Transient or thin intervals of saturation (especially in the region beneath Cañon de Valle) could be present within the vadose zone or may have been present when the outfall was in operation.

Because discharges at building 260 were from HE machining operations, dissolved and particulate (solid phase) HE was likely released from the Outfall. From the outfall pond, subsurface flow and transport pathways include matrix- and fracture-flow within units of the Bandelier Tuff as well as surge beds within the tuff that can promote lateral transport. Because the outfall drained into a wet reach of Cañon de Valle, that portion of the canyon is an important area for recharge and downward transport of HE (LANL 2003, 077965, p. 5-3). Hydrostratigraphic surfaces within the thick Puye sequence likely also play an important role in controlling RDX transport in the deeper parts of the system. A conceptual model of RDX source areas and generalized transport pathways in the vadose zone, springs, surface waters, and groundwater in the vicinity of TA-16 is shown in Figure1.

The 2005 inventory study estimated RDX contamination in 7 discrete components of the TA-16 hydrologic system (LANL 2006, 093798; Table 1). For comparison, the same components are evaluated here. Although that study was based on a limited body of data from a smaller network of monitoring wells than are now in place, it concluded that significant RDX mass may persist in perched-intermediate and regional groundwater: up to 8109 kg and 6053 kg, respectively. These would be the most contaminated of the 7 hydrologic components evaluated. However, both the concentrations of RDX and estimated footprint of contaminated groundwater in the perched-intermediate system and regional aquifer were largely unknown. The estimates were based on 12 samples from 2 wells within the perched-intermediate system, and on data from only 1 well (R-25) for the regional aquifer. Relatively large masses of RDX were also estimated in unsaturated zones of tuff beneath the pond area and the alluvial aquifer in Cañon de Valle.

This update to the 2005 report first describes a "simple geometry" approach for estimating the RDX inventories in the seven TA-16 hydrological components. An alternative "geostatistical" approach was also used to estimate inventories for the alluvial, perched-intermediate, and regional zones, and this approach and the results are discussed herein.

2.0 Methods

The inventory estimate in this report utilizes groundwater analytical data and hydrogeological observations to estimate the volumetric extent of RDX contamination and the total mass of RDX in the vicinity of the TA-16 260 Outfall and Cañon de Valle. The concentrations in each part of the system are compiled and partitioned, in most cases, using a quartile approach. The first quartile is taken to represent the lower bound of concentration for a given unit, while the third quartile represents the upper bound for that unit. This approach is considered the best way to account for the skewed distributions of concentrations, as seen in histogram plots. In cases where data are scarce or near detection limits, maximum- or average- concentrations are selected as more useful for making conservative estimates.

The volume of a saturated interval is estimated using simple geometry. For perched-intermediate groundwater, the bulk volume of a saturated interval is estimated from well-specific driller's logs, geophysics data, and water-levels from completed wells. Correlations of saturated intervals between wells and bounds provided by wells with no perched-intermediate saturation are used to provide both an approximate areal extent and thickness of saturation. The area multiplied by an assumed "average" thickness provides a bulk volume for the unit. The estimated volume is then multiplied by an estimated saturated porosity of the formation to estimate the volume of contaminated groundwater. For regional groundwater, a similar calculation is made, although the volume constraint is the approximate extent of contamination rather than the zone of saturation.

Although this inventory reevaluation utilizes recent data from more monitoring locations than were available previously, there is still considerable uncertainty in the updated estimates. The primary sources of uncertainty are the areal extent and volume of contaminated zones and aquifer porosity and variability. Error may also be associated with the heterogeneity of

groundwater characteristics and fracture flow-type preferential pathways and RDX degradation over time.

Although the focus of this study is groundwater contamination, the near-surface mass of RDX was also estimated based on data presented in the July 2002 "Interim Measure Report for Potential Release Site 16-021(c)-99" (LANL 2002, 073706). Discharges from the 260 Outfall were greatest in the 1950s; they later decreased, continuing at low levels for more than 30 yr (Gard and Newman 2005, 093651, p. 19). The 260 Outfall was decommissioned in 1996 as remediation programs commenced. Near the surface, efforts have been made to restrict downward migration of RDX, including source removals in 2000 and 2001 (LANL 2002, 073706, p. 31) and 2009 (LANL 2010, 108868, p. 8) from the pond area, placement of crushed tuff and bentonite layers in excavated areas, and grouting of a highly porous surge bed zone beneath the settling pond (LANL 2010, 108868, pp. 11–12).

3.0 Hydrologic Component Inventories, Including Basis and Assumptions

This section describes the data and assumptions that were used to estimate inventories for each of the seven TA-16 components, and the rationale for the update from the 2005 inventory estimates. The 2005 RDX inventory values and the updated values are compared in Table 2.

3.1 260 Outfall Former Settling Pond Area

During 2000–2001 interim measure activities, soil exceeding 100 mg HE/kg soil was targeted for removal from the settling pond area. At that time, more than 990 m^3 of contaminated soil was removed (LANL 2003, 077965), some of the material with HE concentrations of 2 wt% (20,000 ppm) or more. During the interim measure, an estimated 8500 kg of HE (RDX and other HE types) was removed (LANL 2002, 073706, p. 72) or 90% of the total HE that existed in the 260 Outfall source area (soil and shallow tuff) before the interim measure was implemented. The remaining mass of RDX was estimated at 650 kg, based on post-removal analytical data and estimates of volume and bulk density in each of three strata below the outfall, identified based on geology and preexcavation contaminant levels. The three strata are designated in the interim measures report as follows:

- Stratum A – Surface material from the excavated drainage channel between the outfall and the edge of the cliff, including the upper drainage and settling pond.
- Stratum B – Surface material from the drainage channel between the base of the cliff and the drainage channel's confluence with Cañon de Valle, including the lower drainage.
- Stratum C – Subsurface material from the center of the drainage channel between the outfall and the cliff (LANL 2002, 073706, p.49).

The remaining 650 kg estimate included HE present in a surge bed below the settling pond area (LANL 2002, 073706, p. 72). Surge beds are thin, relatively high porosity, discontinuous structures within the tuff. In boreholes below the settling pond area, RDX is present at concentrations up to 4500 mg/kg (4500 ppm) in a surge bed at about 5 m below the ground surface (LANL 1998, 059891, p. 2-66).

Since the 260 Outfall was decommissioned in 1996, infiltration through the contaminant source area in the vicinity of the outfall has been significantly reduced and is limited to infiltration from precipitation and snowmelt. As a result, mobilization of RDX has likely been reduced in recent years, and it is reasonable to assume that much of the 650 kg remains in the vadose zone near the outfall.

Although the 2005 inventory places the entire 650 kg of HE in the pond area (for the inventory calculations it was assumed the HE was RDX), according to the interim measure report (LANL 2002, 073706), this value represents the entire HE inventory in the vicinity of Consolidated Unit 16-021(c)-99, which includes the upper and lower sections of the drainage channel as well as the surge bed.

In 2009, cleanup activities associated with the corrective measures implementation (CMI) plan followed the site-specific screening action level of 36.9 mg/kg for RDX (LANL 2010, 108868, p. 8). A field analysis method was used to guide soil removal, and subsequent laboratory analysis was used to validate the results. Three locations within the settling pond area were excavated, yielding approximately 30 m^3 of soil (LANL 2010, 108868, p. 7).

During the previous interim measures activities, soil with concentrations exceeding 100 mg/kg had been targeted for removal; therefore, the calculation here assumes that the 30 m^3 of soil removed had an average RDX concentration of 100 mg/kg. Assuming a conservative density value of 1900 kg/m^3, the CMI would have removed less than 6 kg of RDX from the 260 Outfall settling pond area. Subtracted from the 650-kg value from in the interim measure report, 644 kg of RDX would remain in the pond area. This amount would be distributed in a large amount of soil at concentrations below 36.9 mg/kg; at this concentration, 644 kg of RDX would occupy about 9200 m^3 of soil in and around the drainage channel (Table 2).

However, a large part of this inventory is believed to be present in the underlying surge bed, which was grouted to immobilize HE associated with unsaturated tuff (LANL 2010, 108868; LANL 2002, 073706, p. 12). Although the degree of HE immobilization within the surge bed cannot be quantified, it is believed that considerable HE was immobilized through the grouting effort, in which more than 6000 gal. of low-viscosity grout was injected into 16 injection boreholes. Because the effects of grouting on RDX inventory could not be quantified, the mass of HE immobilized through grouting was not included in this inventory reevaluation.

3.2 Vadose Zone Directly under 260 Outfall Area

The 2002 interim measure report presents core data from borehole 16-6370, drilled to a depth of 25 m below the settling pond area (LANL 2002, 073706, p. 35). In samples collected at 1.5-m intervals, the highest RDX concentration is 1.48 mg/kg. It is worth noting that far greater concentrations occur sporadically in localized near-surface zones (e.g., see section 1.0). Their distribution, consistent with the site conceptual model (Figure 1), is understood to be along preferential fracture-flow pathways and in surge beds where lateral transport of shallow groundwater occurs (LANL 2002, 073706, p. 13). Of 46 samples collected from Bandelier Tuff

in this area, 3 are above 1000 mg/kg, with the highest, 4500 mg/kg, in a surge bed beneath the pond area (LANL 1998, 059891, p. 2-66). All but 12 of the samples are below 15 mg/kg, and the median is 1.74 mg/kg. This value is used to calculate the minimum RDX mass in the 260 Outfall vadose zone. Although it underrepresents some locally contaminated areas in the upper section of the tuff, the RDX profile of borehole 16-6370 supports the assumption that nearly 200 m of underlying tuff has contamination levels well below the median. Below 20 m, RDX drops to below 0.1 mg/kg (LANL 2002, 073706, p. 40). Surge bed–associated RDX is accounted for in the 260 Outfall component (in 2006, 650 kg of RDX); as in the 2005 inventory, some double counting is possible between these components. However, a few high concentrations do not result in elevated median concentrations.

Somewhat larger and more variable RDX concentrations are detected in samples collected along the length of the upper and lower drainage channel, as presented in Table 2.2-1 of the Phase III RFI report (LANL 2003, 077965, p. 2-4). The highest of these numbers are from surface samples collected in the center of the drainage channel and are considered potentially representative of concentrations in underlying tuff. The median concentration among them, 3 mg/kg, is used to constrain the higher end of RDX mass in the 260 Outfall vadose zone. The distribution of solid-phase RDX results from various sources is shown in Figure 2 (LANL 1998, 059891; LANL 2002, 073706; LANL 2003, 077965).

To estimate the RDX present in the vadose zone, concentrations are multiplied by the estimated mass of the overburden (see Figure 1 for a conceptual view of the extent of overburden). The area is considered as the size of the former settling pond (approximately 15 m × 6 m), together with the drainage channel (approximately 192 m × 5 m). The depth to the first screen in a saturated zone [CdV-16-4ip] is 250 m; this depth is used to complete the vadose zone volume. A bulk density of 1.19 g/cm^3, or 1190 kg/m^3, representative of the Otowi Member of the Bandelier Tuff (Rogers and Gallaher 1995, 097569), is used to conservatively estimate the contaminated mass at 3.13×10^8 kg.

The range of RDX mass was estimated to be between 545 kg and 940 kg (Table 2). The vadose zone is understood to be highly heterogeneous and dominated by fracture flow, and thus the uncertainty of the estimate is great.

3.3 Mesa Vadose Zone Encountered by Saturated Zones Feeding SWSC and Burning Ground Springs

In the 2005 inventory, maximum and minimum RDX concentrations in springs sample water were multiplied by maximum and minimum flow rates, yielding figures for maximum and minimum yearly releases. A 100-yr release period was assumed. In the 2005 study, the calculated minimum mass of RDX (3 kg) would be discharged in 100 yr (minimum), while in 100 maximum flow years a total of 482 kg would be discharged from the springs. For this report, the aim has been to balance such extremes of flow with more typical conditions. Histograms in Figure 3 show the variability of RDX concentrations from samples collected from the two Cañon de Valle springs.

To make the mass estimations, flow data from SWSC and Burning Ground Springs were compiled for Water Years 1997 through 2010 (Water Years begin on October 1 and end on September 30). The median value for each was used to project a volume of discharge over a span of 100 yr; as in the 2005 study, it was assumed that RDX would be depleted from the springs in that time. The ranges of mass discharge are estimated by multiplying the 100-yr average discharge volumes by the first and third quartiles for each spring. The minimum mass discharge is defined by the value of the first quartile, and the maximum is defined by the value of the third quartile. The 33- to 56-kg range presented in Table 2 are sums for the two springs and represent a small percentage of the total RDX inventory at TA-16. The lower end of this range is similar to the mass calculated from average annual Burning Ground and SWSC Springs flow and concentration data for the last 11 yr (LANL 2016, 601837).

3.4 Alluvial Sediments in the Bottom of Cañon de Valle

The 2005 inventory cites a value of 5 kg RDX in alluvial sediments of Cañon de Valle from Reid et al. (2005, 093660, p. 753). This estimate is based on a geomorphic assessment of canyon-bottom sediments. The 2011 Water Canyon/Cañon de Valle investigation report (LANL 2011, 207069, p. 45) approximates the mass of RDX in alluvium as 11 kg, 66% (7.3 kg) of which is located in Cañon de Valle, and 24% (2.6 kg) of which is located in Water Canyon below the confluence with Cañon de Valle. Together, the RDX present in these two reaches are taken as the maximum value (10 kg), while the 5-kg value provided in Reid et al. (2005, 093660) is considered the minimum value (Table 2).

3.5 Vadose Zone beneath Cañon de Valle and above the Perched-Intermediate Groundwater Zone

The vadose zone beneath Cañon de Valle and above the perched-intermediate groundwater zone is composed primarily of unsaturated-tuff. Thin saturated areas are also likely present, and these may be transient depending on surface flow variations over time within in the canyon bottom. Few RDX concentration data are available in this zone, which makes mass estimation difficult. However, estimates can be derived using RDX concentrations and estimated leakage rates in the alluvial aquifer. In other words, even though direct information about how much RDX is in the vadose zone beneath Cañon de Valle is not available, the inputs to the vadose zone can be estimated. In these estimates, the area of contribution below the canyon bottom is described by

the length of the Cañon de Valle groundwater system (7750 ft, LANL 2003, 077965) and the typical width of the alluvial sediment package in the flowing reach. Leakage to the underlying tuff was estimated as part of a water balance study at 2.6 gal/ft*day (LANL 2003, 077965, p. 5-9–5-11). When combined, the leakage rate, area, and alluvial groundwater RDX concentration give a mass flux of RDX to the vadose zone. To calculate mass estimates, a time interval needs to be assumed: in this case, the 100-yr period used in the RDX mass estimation for springs above was used. Because the springs are a substantial contributor of RDX to Cañon de Valle, using the same time frame provides consistency.

As with other estimates in this report, the quartile approach is used to constrain the RDX concentrations. The third quartile concentration value from alluvial wells, 23.1 µg/L, is used as a maximum, and the first quartile value, 2.7 µg/L, is used as a minimum. Using the estimated mass flux and a 100-yr time frame, a maximum of 64 kg, or a minimum of 8 kg, would move from the alluvial aquifer of Cañon de Valle into the vadose zone above perched-intermediate groundwater (Table 2). Differences in these estimates and the 2005 estimates arise mainly because of a more extensive alluvial aquifer concentration time series and because of differences between the quartile approach and the very conservative, maximum alluvial aquifer concentration that was assumed in 2005. These new estimates suggest that this zone has an inventory comparable to the inventory of the springs. However, because of the lack of actual concentration data in the vadose zone below Cañon de Valle, estimates of inventory are highly uncertain.

3.6 Perched-Intermediate Groundwater

3.6.1 Perched-Intermediate Zone RDX Concentrations

RDX concentrations in monitoring wells CdV-16-4ip, R-25b, CdV-9-1(i), CdV-16-1(i), and CdV-16-2(i)r were used to estimate inventories in perched-intermediate groundwater. The perched-intermediate zone consists of two regions: a thicker and more extensive upper zone, and a thin, less extensive deeper zone. Cross-sections of the perched-intermediate zone including well screen locations are shown in Figures 4, 5, and 6. Inventories for upper- and lower-perched-intermediate groundwater were calculated separately.

Variations in RDX concentrations in upper perched-intermediate groundwater are shown in the histogram in Figure 7. A summary of 92 samples from upper-intermediate well screens is provided in Table 3. Because of the significant range of contaminant concentrations in upper perched-intermediate groundwater, the quartile method was used to constrain a likely range of concentrations. High and low concentrations for the upper intermediate zone were determined by the third- and first-quartile values, respectively. The median of the upper perched-intermediate data is 49.3 µg/L. The first quartile is 26.1 µg/L, and the third quartile is 81.9 µg/L. To calculate the maximum and minimum masses of RDX in the intermediate zone, the third and first quartile concentrations were multiplied by the estimated maximum and minimum volumes for pore water in the zone (perched-intermediate volumes are discussed in section 3.6.2).

Deep perched-intermediate groundwater occurs between 1000 ft and 1200 ft bgs and data are quite limited. Available results from CdV-16-4ip screen 2 show RDX ranging from 19.9 µg/L to 22.2 µg/L (the first sample showing RDX at 167 µg/L is considered an outlier showing vertical flow from drilling and was excluded from this analysis). Based on these data, 20 µg/L was assumed as a representative concentration for the deeper perched groundwater zone.

R-25 screen 4 is also completed within this deeper perched-intermediate zone. Although data from
R-25 screen 4 were not used to estimate the RDX inventory for this reevaluation, the RDX concentrations from this screen range from 12.4 µg/L to 26.7 µg/L, supporting the use of 20 µg/L for mass calculations for this zone.

3.6.2 Perched-Intermediate Zone Volumes

The volumes of groundwater present in the perched-intermediate zones are approximated from maps and cross-sections related to this study, created with information gained during well drilling and development. These calculations are subject to a high degree of uncertainty. Thus, a key sensitivity of inventory estimation is the volume of RDX contamination. The inventory will scale with volume, so errors in the volume estimates will affect the calculated mass. The volumes assumed are considered to be conservative best estimates. If additional wells are drilled, the volumes and inventories can be recalculated if it appears the new data might substantially affect the current estimate.

The areas of upper perched-intermediate groundwater and RDX contamination are shown in blue and green, respectively, in Figure 8. The estimated area of contamination is 350,012 m^2. The areal extent of contaminated deep perched-intermediate groundwater is poorly constrained. Using an area bounded to the west by building 16-260 and the 260 Outfall and available well data (Figure 9), the estimated area of the contaminated part of the deeper perched groundwater is 513,940 m^2. This area is larger than that estimated for the contaminated part of the upper perched-intermediate zone, which suggests the deeper perched contaminated area may be overestimated. However, given the lack of constraints regarding the lower perched-intermediate zone, the 513,940 m^2 area was used because it is conservative.

Although the saturated perched-intermediate zones are lens-shaped, their volumes are estimated by assuming uniform thicknesses. At its thickest, the upper zone is estimated to be 134 m thick in the vicinity of CdV-9-1(i). For the calculation, a 76.2-m thickness was used. The thickness was multiplied by the area discussed above to obtain a volume. In cross-section, the contact between the Otowi Member and the Puye Formation occurs approximately halfway through the saturated upper zone; this places 38.1 m in each formation. The bulk volumes are therefore equal, although the volumes of groundwater differ according to porosity.

Statistical analyses of porosity for each formation are taken from a spreadsheet based on Schlumberger, Inc., geophysical logs. The data were derived from well R-26, where a mud-drilled borehole provided nearly ideal logging conditions, and include combined magnetic

resonance, density porosity, thermal and epithermal neutron logs (Kleinfelder 2005, 087846). The spreadsheet, entitled "Summary of Borehole Porosity Measurements by Geologic Unit for Well R-26," is included as Appendix A.

The porosity values within 1 standard deviation of the median are multiplied by the bulk volumes to calculate a range of volumes of pore water. The Otowi Member of the Bandelier Tuff is significantly more porous, between 40% and 46%, while the Puye Formation has porosity of between 18% and 33%. The pore water estimated in the Otowi Member is between 5.4 and 6.1 billion liters; in the Puye Formation, it is between 2.5 and 4.4 billion liters. The total of the two lower volume estimates is 7.9 billion liters and the total of the two upper volume estimates is 10.5 billion liters.

For the deep perched-intermediate zone, a thickness of 7.6 m was assumed based on well data. Although it is perhaps 18 m thick in some places, it also would taper to thin edges. The 7.6-m thickness, multiplied by the area discussed above and the upper and lower values of Puye porosities provide a range of pore water volumes from 0.72 to 1.28 billion liters for the deep perched-intermediate zone.

3.6.3 Perched-Intermediate Groundwater Results

To estimate minimum RDX mass in the upper zone, the smaller volume, 7.9 billion liters, is multiplied by the first quartile intermediate RDX concentration, 26 µg/L. The larger volume, 10.5 billion liters, is multiplied by the third quartile concentration, 82 µg/L, to give the maximum mass in the upper zone. The range in the upper perched zone is between 205 kg and 862 kg. For the lower perched zone, the assumed concentration of 20 µg/L is multiplied by the high- and low-volume estimates to yield a range of 14 kg to 26 kg. To obtain a range of RDX mass for the entire perched system, the sums of the high-mass estimates and the sums of the low-mass estimates for both zones are calculated. The resulting range for the entire perched-intermediate groundwater region is 219 kg to 887 kg (Table 2). The minimum is based on 40% porosity in the Otowi Member and 18% porosity in the Puye Formation, with an RDX concentration of 26 µg/L in the upper zone and 20 µg/L in the lower zone. The maximum is based on respective porosities of 46% and 33%, and RDX concentrations of 82 µg/L in the upper zone and 20 µg/L in the lower zone.

3.7 Regional Groundwater

Data gathered since the 2005 inventory study allow for a markedly different interpretation, both of the overall mass as well as the distribution of RDX that could be expected in the regional aquifer below the 260 Outfall. The following contrasts in data availability between the study presented here and the 2005 study are worth noting.

The 2005 inventory relied on early data from R-25, which then was the only well showing RDX in regional groundwater. However, early analytical data from R-25 are considered unreliable (LANL 2011, 207069) because they reflect the influence of commingled contaminated perched-intermediate groundwater with regional groundwater. For this reason, analytical data from R-25

were not used to calculate the revised RDX inventory estimates. The 2005 study was based on preliminary data and assumed that RDX could be present as far as 400 m below the regional water table surface. However, the early RDX concentrations detected in deeper regional screens of R-25 likely reflected cross-flow from contaminated perched-intermediate groundwater, which occurred during drilling and before development.

Recent analytical data from R-25 show low concentrations of RDX in the upper two regional screens (screens 5 and 6), and RDX is not detected in deeper screens. The top of screen 6 is 27.7 m below the water table), and this may represent the lowermost extent of RDX contamination in the regional aquifer.

In recent years, RDX has been persistently detected in two newer regional wells: R-63 and R-18. RDX contamination has not been detected in other nearby wells in the regional aquifer (R-47, R-48, and R-58) which helps constrain the areal extent of contamination. The 2005 inventory study assumed the extent of RDX contamination in the regional aquifer equal in size to the known extent of the upper perched-intermediate groundwater zone. Here, a smaller footprint of contamination in the regional aquifer is assumed based on the recent updated conceptual model, persistent contamination in R-63 and R-18, and the absence of contamination in wells R-47, R-48, and R-58.

3.7.1 Regional Zone Volume

For the 2005 inventory, a large, somewhat arbitrary, contaminated volume was assumed below the regional water table. The principal reason for this assumption was the data from R-25 showing RDX in groundwater at the deeper screens. The idea then was to assume a depth within the aquifer at which no RDX could reasonably be present and then calculate a conservative estimate of the potential volume of contamination. The inventory presented a maximum of 6053 kg and a minimum of 135 kg RDX, while acknowledging that the actual mass of RDX in the regional zone may in fact be less than 135 kg. For the 2016 inventory, the matter of contaminated volume is addressed differently, and lower inventories are in fact the case.

In this study, a far shallower depth of the regional aquifer is considered to be contaminated, based on the more recent sampling data from R-25. Low concentrations of RDX, just above the detection limits, persist in screens 5 and 6. Screens 7 and 8 show no detectible RDX since 2007, and the depth of contamination in the aquifer is assumed to be 46 m below the water table.

The area of contamination for the updated RDX inventory assessment is defined differently based on data from newer wells, which constrain the extent of contamination. Well R-18, to the northeast of the 260 Outfall, shows increasing concentrations of RDX, while R-47, south and slightly east of R-18, shows none. The RDX plume in the upper part of the regional aquifer is conceptualized as a triangle spreading out to the east of the 260 Building. One vertex is located to the north of R-18, with another to the south of Fish Ladder Canyon in the direction of new well R-58. Because RDX has not been detected at well R-48, it constrains the contaminated area on the southwest. The only other well where RDX was detected, R-63, is within the triangle to

the east. The area, bounded by an orange polygon in Figure 8, is 1.214×10^6 m^2. The bulk volume is calculated as 37 million cubic meters. As with the intermediate-perched zone, the porosity of the Puye Formation is within the range of 18% to 33% (Kleinfelder 2005, 087846). The pore volume of this zone as defined above is estimated to range between 10.3 and 18.3 billion liters.

3.7.2 Regional Zone RDX Concentration

In the 2005 inventory study, regional groundwater was estimated using RDX concentrations from screens 5 and 8 of well R-25, zones that are now thought to have been contaminated by intermediate groundwater during time the borehole was left undeveloped (LANL 2011, 207069). Well R-25 data are not used for RDX mass calculation in this report, although the decline in RDX concentration over the past several years at each of the lower (regional) screens of that well is worth noting. These data are presented in Figure 10; the most recent samples in R-25 had concentrations below 1 µg/L. Also, RDX has not been detected in screens 7 and 8 of R-25 since 2007. This information is presented to justify the omission of R-25 data from this inventory and to suggest those data skewed the results of the 2005 inventory. Similarly, two samples from well R-63 with RDX concentrations of 15 µg/L and 15.9 µg/L are excluded because they appear to contain water from well development (Figure 11). Two days after the 15.9-µg/L sample was collected, the concentration had dropped to below 1 µg/L and has remained below 3 µg/L since that time.

For the current inventory study, maximum and minimum concentrations were multiplied by an estimated volume to capture a range of values for RDX mass. Regional aquifer mass estimates are sensitive to the assumed volume (just as perched-intermediate zone estimates are) and if future data suggest that the contaminated volume is substantially different than assumed here, mass will need to be recalculated. The concentrations used were from the regional aquifer wells with RDX detections, R-18 and R-63, minus the two data points discussed above (Table 4). For the maximum, the highest measured concentration among them, 3.73 µg/L, is used. The increasing RDX trend in R-18 (Figure 12) suggests the highest value recorded, rather than the third quartile value, should be used to calculate the estimate. The minimum concentration is estimated conservatively as the median of all detected samples, calculated as 1.21 µg/L. This is a somewhat arbitrary number derived from a set of data that excludes all "nondetected" samples. An additional uncertainty in the mass estimate for the regional aquifer is related to the fact that R-18 is screened approximately 21 m below the top of the regional aquifer, and it is not known whether RDX concentrations are higher near the water table.

3.7.3 Regional Groundwater Results

The minimum mass is calculated with the minimum pore water volume, 10.3 billion liters, and the median concentration of all regional samples detecting RDX, 1.21 µg/L. The pore water volume maximum, 18.3 billion liters, is multiplied by the maximum RDX concentration from regional groundwater sampling, 3.73 µg/L. The regional zone is estimated by this method to contain between 13 kg and 68 kg RDX. Additional monitoring wells are planned for installation

north of Cañon de Valle in 2017 (LANL 2016, 601779). Data from these wells should help reduce the uncertainty in the RDX mass estimates for the regional aquifer.

4.0 Summary of Results

The most significant differences between this study and the 2005 estimate are in the RDX mass estimates for regional and intermediate groundwater, respectively (Table 2). In 2016, the regional groundwater zone was estimated to contain between 13 kg and 68 kg, compared with between 135 kg and 6053 kg in 2005, representing a decrease in the estimate of between 94% and 99%. The intermediate groundwater zone was estimated to contain between 219 kg and 887 kg, compared with 476 kg and 8109 kg in 2005, representing a 54% to 89% decrease in the estimate. The saturated zones feeding SWSC and Burning Ground Springs are estimated to contain between 33 kg and 56 kg, compared with between 3 kg and 482 kg in 2005.

During the CMI in 2009, it was estimated that 5 kg of RDX was removed by excavation, leaving 644 kg in soils within the Consolidated Unit 16-021(c)-99 area that includes the former pond, outfall area, drainage channel, and surge bed below the pond. Compared with 650 kg estimated in 2005, this represents a decrease of 0.9%. However, grouting of the underlying surge beds has likely immobilized a substantial fraction of this inventory, but it was not accounted for in these estimates because of uncertainties related to the spatial distribution of the immobilized RDX within the subsurface from the introduced grout. A more recent geomorphology study of alluvial sediments estimated slightly more RDX in Cañon de Valle sediments (LANL 2011, 207069), suggesting some redistribution of contaminants occurred as a result of post-fire runoff. The range is between 5 kg and 10 kg compared with 5 kg in 2005. A different approach to assessment of vadose zone RDX contamination resulted in a smaller maximum value and a larger minimum compared with the 2005 inventory. The range is between 545 kg and 940 kg compared with 234 kg and 4311 kg (2005), representing either a 133% increase or a 78% decrease from 2005. In the vadose zone beneath the Cañon de Valle alluvial aquifer, values between 8 kg and 64 kg were estimated, compared with 17 kg and 3724 kg in 2005, representing a 53% to 98% decrease.

Overall, the values range between 1464 kg and 2644 kg of RDX estimated to be in all components of the hydrologic system at TA-16. In 2005, the values were 1520 kg and 23,334 kg, respectively. On the low end, the decrease from 2005 figures is 3.5%, and on the high end the decrease is 88.6%.

The 2009–2010 CMI was conducted to remediate HE and other contaminants detected at the 260 Outfall, including a concrete trough, a former settling pond, and the outfall drainage channel. Remediation activities conducted during the 2009–2010 CMI are discussed in the “Summary Report for the Corrective Measures Implementation at Consolidated Unit 16-021(c)-99” (LANL 2010, 108868) and in the “Addendum to the Summary Report for the Corrective Measures Implementation at Consolidated Unit 16-021(c)-99” (LANL 2010, 110508). These activities have reduced contaminant levels in near-surface soils and stabilized contaminants in the underlying surge beds near the 260 Outfall.

Currently, the primary areas of concern are contamination within intermediate and, to a lesser extent, regional groundwater, and beneath the Cañon de Valle alluvium. Recent data from monitoring wells have improved the understanding of RDX concentrations in perched-intermediate and regional zones, although uncertainty associated with estimating volumes of contaminated groundwater is still significant. Information from future samples and new wells will help to evaluate the current inventory estimates, and the calculations may need to be revised if future results indicate substantially different conditions.

5.0 Alternative Inventory Approach

Results comparable to those described above were produced using a geostatistical approach (Table 5), as detailed in the report "TA-16 Groundwater RDX Evaluation," prepared by Weston, Inc. (Weston 2016, 601835) and was included in a recently prepared Laboratory report, "Geology Report for Technical Area 16 and Vicinity." An existing geologic framework model was used with EarthVision software (Dynamic Graphics 2015) to model volumes of the contaminated saturated zones, and to spatially interpolate subsurface distribution of RDX in three dimensions. Mass estimates for RDX were produced by the integration of three-dimensional (3-D) models. The geostatistical method focuses on aqueous phase RDX distribution within regional, perched-intermediate, and alluvial groundwater; it corresponds to three of the seven hydrologic compartments considered in the simple geometry method, excluding those related to HE contaminants in the vadose zone.

With the geostatistical approach, the centroid of the plume is placed at the location of the highest sample concentration, and decreasing concentrations of RDX are interpolated outwardly across the other sample locations. Although the resulting volume of perched-intermediate water considered is nearly 47 billion liters, which far exceeds the 8 to 10 billion liters calculated for the simple geometry approach, much of it has very low concentrations of RDX. For example volumes represented in blue-green to blue have concentrations below 26 µg/L (Figure 13, left panels), which was the quartile value used to estimate the minimum RDX in the simple geometry study.

The mass of RDX estimated for perched-intermediate zones (UPZ + LPZ) is between 650 kg and 1581 kg, which corresponds to simple geometry minimum and maximum values of 219 kg and 887 kg.

Similarly, the volume of regional aquifer material is greater than the volume considered in the simple geometry approach. While the Weston study integrates RDX concentrations across approximately 85 billion liters, the simple geometry study uses a range of regional aquifer water volumes between 10.3 and 18.3 billion liters. However, the concentrations are interpolated outward to 0.04 µg/L, resulting in smaller mass of RDX (1.8 kg to 8.5 kg) than calculated by the simple geometry approach (10 kg to 42 kg).

In the simple geometry study, 5 kg to 10 kg RDX was estimated in the alluvium in Cañon de Valle, based on a geomorphic assessment of surface sediments (Reid et al. 2005, 093660; LANL

2011, 207069). By contrast, the geostatistical approach employs shallow well samples interpolated across the extent of alluvial saturation, where concentrations range from 2.5 µg/L to 17.6 µg/L. The geostatistical approach results in an estimation of only 0.16 kg RDX. However, in this method RDX outside of the alluvial aquifer, but in the canyon bottom sediments, is not accounted for.

In terms of total inventories for the regional, perched-intermediate, and alluvial groundwater zones, the geostatistical approach produced a range of between 651 kg and 1589 kg RDX, while the simple geometry approach produced a range of 234 kg to 939 kg. Most of the difference between the estimates is related to the perched-intermediate zone. Overall, the two new studies have substantial overlap, suggesting that they yield reasonable bounds on inventories (given the available data). Both approaches yield narrower ranges that contrast markedly with the 2005 estimates, where the corresponding aquifer compartments were thought to contain between 616 kg and 14,167 kg.

6.0 Conclusions

The 2016 RDX inventory reevaluation estimated a substantially lower mass of RDX in the environment at TA-16 than was originally estimated in 2005. The 2005 estimates were based on a smaller population of wells and a limited data set, and considerable additional characterization has been undertaken since 2005 to collect data to assess the extent of groundwater contamination, especially in perched-intermediate groundwater and in the regional aquifer. These activities included installing additional perched-intermediate monitoring wells R-25b, R-25c (dry), R 47i, R-63i, CdV-9-1(i), and CdV-16-4ip and regional monitoring wells R-18, R-48, and R-58. Data from these new wells were used to update the estimate of RDX mass in intermediate and regional groundwater at TA-16.

This inventory reevaluation estimated the range of RDX masses in seven environmental components at TA-16: (1) the 260 Outfall settling pond area, (2) the vadose zone beneath the outfall, (3) the zone feeding SWSC and Burning Ground Springs, (4) the alluvial sediments in Cañon de Valle, (5) the vadose zone beneath Cañon de Valle, (6) perched-intermediate groundwater, and (7) regional groundwater. Although the minimum total RDX estimates are only slightly lower than the 2005 estimates, the maximum total RDX values are significantly (88%) lower than the maximum values from 2005. For intermediate and regional groundwater, the revised estimates are between 54% to 99% lower than the 2005 estimates.

Another important area that the inventory study helps clarify is the relative distribution of RDX among the seven components. Perched-intermediate groundwater contained considerably more RDX than alluvial or regional groundwater, containing approximately 80% of all the RDX currently present in groundwater. For this reason, perched-intermediate groundwater would likely be a key target for corrective action compared with alluvial or regional groundwater.

Potential corrective actions might include protecting the regional aquifer by contaminant mass removal in the overlying perched-intermediate groundwater or by gradient manipulation in

perched-intermediate groundwater to inhibit downward transport to the regional aquifer. Such action would also be protective of the regional aquifer by lowering the potential mass that might be transported to the regional aquifer in the future.

Significant RDX inventories also persist in the former outfall settling pond area and in the vadose zone beneath the outfall settling pond area. Given the fact that the outfall is no longer operational and no longer receives liquids and the outfall settling pond area is covered by a low-permeability cap, RDX migration from these components should be negligible or greatly reduced. In addition, grouting of the surge beds in the pond area (section 3.1) will have immobilized some RDX and will likely have altered the permeability of the area enough to potentially inhibit downward transport.

7.0 References

The following list includes all documents cited in this report. Parenthetical information following each reference provides the author(s), publication date, and ER ID or ESH ID. This information is also included in text citations. ER IDs were assigned by the Environmental Programs Directorate's Records Processing Facility (IDs through 599999), and ESH IDs are assigned by the Environment, Safety, and Health (ESH) Directorate (IDs 600000 and above). IDs are used to locate documents in the Laboratory's Electronic Document Management System and, where applicable, in the master reference set.

Copies of the master reference set are maintained at the New Mexico Environment Department Hazardous Waste Bureau and the ESH Directorate. The set was developed to ensure that the administrative authority has all material needed to review this document, and it is updated with every document submitted to the administrative authority. Documents previously submitted to the administrative authority are not included.

Birdsell, K.H., B.D. Newman, D.E. Broxton, and B.A. Robinson, 2005. "Conceptual Models of Vadose Zone Flow and Transport beneath the Pajarito Plateau, Los Alamos, New Mexico," *Vadose Zone Journal,* Vol. 4, pp. 620–636. (Birdsell et al. 2005, 092048)

EPA (U.S. Environmental Protection Agency), January 2014. "Technical Fact Sheet - Hexahydro-1,3,5-trinitro-1,3,5-triazine (RDX)," U.S. Environmental Protection Agency Region 6, Dallas, Texas. (EPA 2014, 601836)

Gard, M.O., and B.D. Newman, November 2005. "The High Explosives Source Term at TA-16," Los Alamos National Laboratory document LA-UR-05-9433, Los Alamos, New Mexico. (Gard and Newman 2005, 093651)

Kleinfelder, January 25, 2005. "Final Well R-26 Completion Report, Revision No. 1," report prepared for Los Alamos National Laboratory, Project No. 37151, Albuquerque, New Mexico. (Kleinfelder 2005, 087846)

LANL (Los Alamos National Laboratory), September 1998. "RFI Report for Potential Release Site 16-021(c)," Los Alamos National Laboratory document LA-UR-98-4101, Los Alamos, New Mexico. (LANL 1998, 059891)

LANL (Los Alamos National Laboratory), July 2002. “Interim Measure Report for Potential Release Site 16-021(c)-99,” Los Alamos National Laboratory document LA-UR-02-4229, Los Alamos, New Mexico. (LANL 2002, 073706)

LANL (Los Alamos National Laboratory), September 2003. “Phase III RFI Report for Solid Waste Management Unit 16-021(c)-99,” Los Alamos National Laboratory document LA-UR-03-5248, Los Alamos, New Mexico. (LANL 2003, 077965)

LANL (Los Alamos National Laboratory), August 2006. “Investigation Report for Intermediate and Regional Groundwater, Consolidated Unit 16-021(c)-99,” Los Alamos National Laboratory document LA-UR-06-5510, Los Alamos, New Mexico. (LANL 2006, 093798)

LANL (Los Alamos National Laboratory), March 2010. “Summary Report for the Corrective Measures Implementation at Consolidated Unit 16-021(c)-99,” Los Alamos National Laboratory document LA-UR-10-0947, Los Alamos, New Mexico. (LANL 2010, 108868)

LANL (Los Alamos National Laboratory), August 2010. “Addendum to the Summary Report for the Corrective Measures Implementation at Consolidated Unit 16-021(c)-99,” Los Alamos National Laboratory document LA-UR-10-5576, Los Alamos, New Mexico. (LANL 2010, 110508)

LANL (Los Alamos National Laboratory), September 2011. “Investigation Report for Water Canyon/ Cañon de Valle,” Los Alamos National Laboratory document LA-UR-11-5478, Los Alamos, New Mexico. (LANL 2011, 207069)

LANL (Los Alamos National Laboratory), July 2015. “Work Plan for a Tracer Test at Consolidated Unit 16-021(c)-99, Technical Area 16, Revision 1,” Los Alamos National Laboratory document LA-UR-15-24089, Los Alamos, New Mexico. (LANL 2015, 600535)

LANL (Los Alamos National Laboratory), September 2016. “Evaluation Report for Surface Corrective Measures Implementation Closure, Consolidated Unit 16-02l(c)-99,” Los Alamos National Laboratory document LA-UR-16-27153, Los Alamos, New Mexico. (LANL 2016, 601837)

LANL (Los Alamos National Laboratory), September 2016. “Groundwater Investigation Work Plan for Consolidated Unit 16-021(c)-99, Including Drilling Work Plans for Wells R-68 and R-69,” Los Alamos National Laboratory document LA-UR-16-26493, Los Alamos, New Mexico. (LANL 2016, 601779)

Newman, B.D., D.D. Hickmott, and P. Gram, 2007. “Flow and High Explosives Transport in a Semiarid Mesa in New Mexico, USA,” unpublished manuscript. (Newman et al. 2007, 095632)

Reid, K.D., S.L. Reneau, B.D. Newman, and D.D. Hickmott, August 2005. “Barium and High Explosives in a Semiarid Alluvial System, Cañon de Valle, New Mexico,” *Vadose Zone Journal,* Vol. 4, pp. 744–759. (Reid et al. 2005, 093660)

Rogers, D.B., and B.M. Gallaher, September 1995. “The Unsaturated Hydraulic Characteristics of the Bandelier Tuff,” Los Alamos National Laboratory report LA-12968-MS, Los Alamos, New Mexico. (Rogers and Gallaher 1995, 097569)

Weston (Roy F. Weston, Inc.), February 2016. “TA-16 Groundwater RDX Evaluation, Los Alamos National Laboratory, Los Alamos, New Mexico,” Los Alamos, New Mexico. (Weston 2016, 601835)

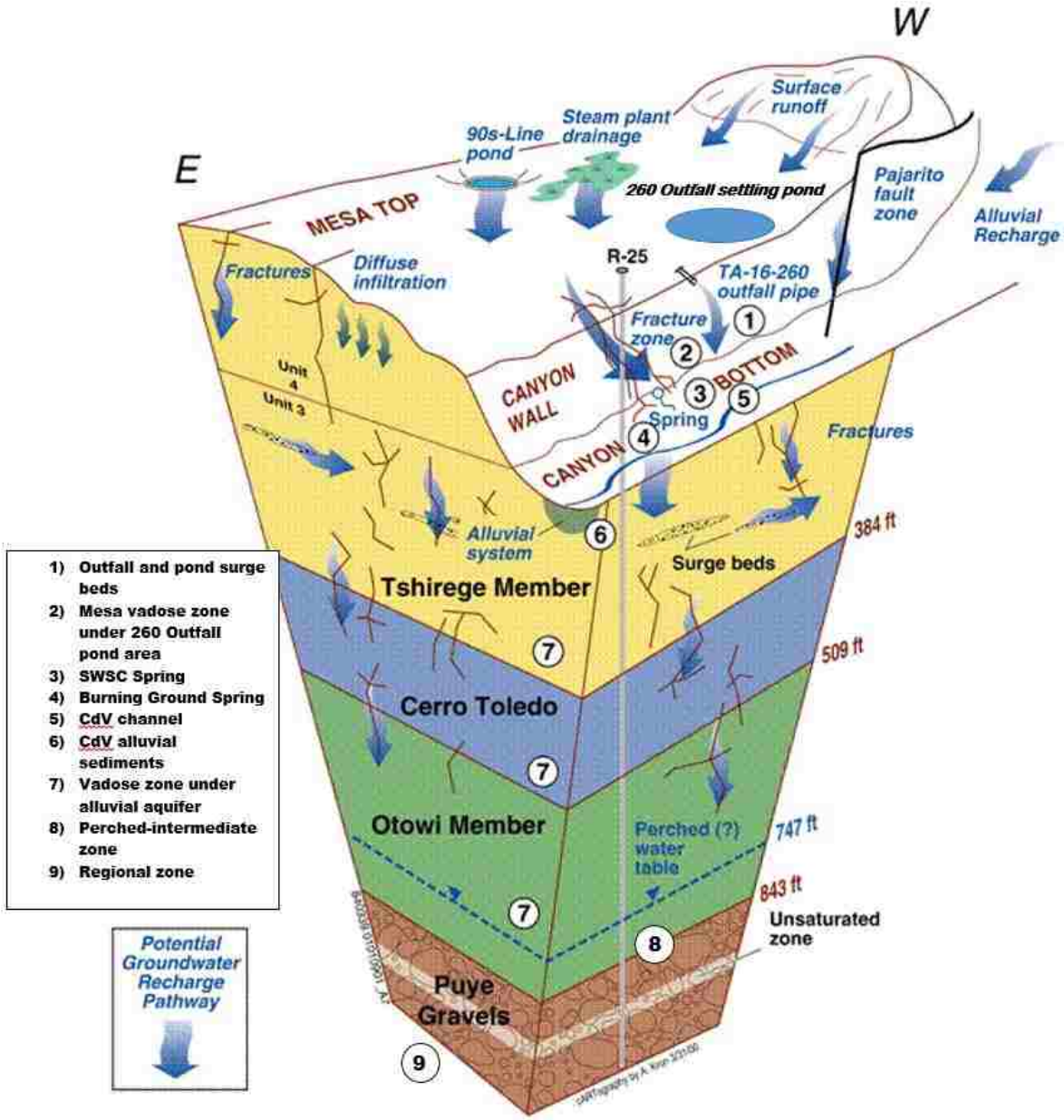

Figure 1 Conceptual model of RDX source areas and transport pathways through the subsurface at TA-16

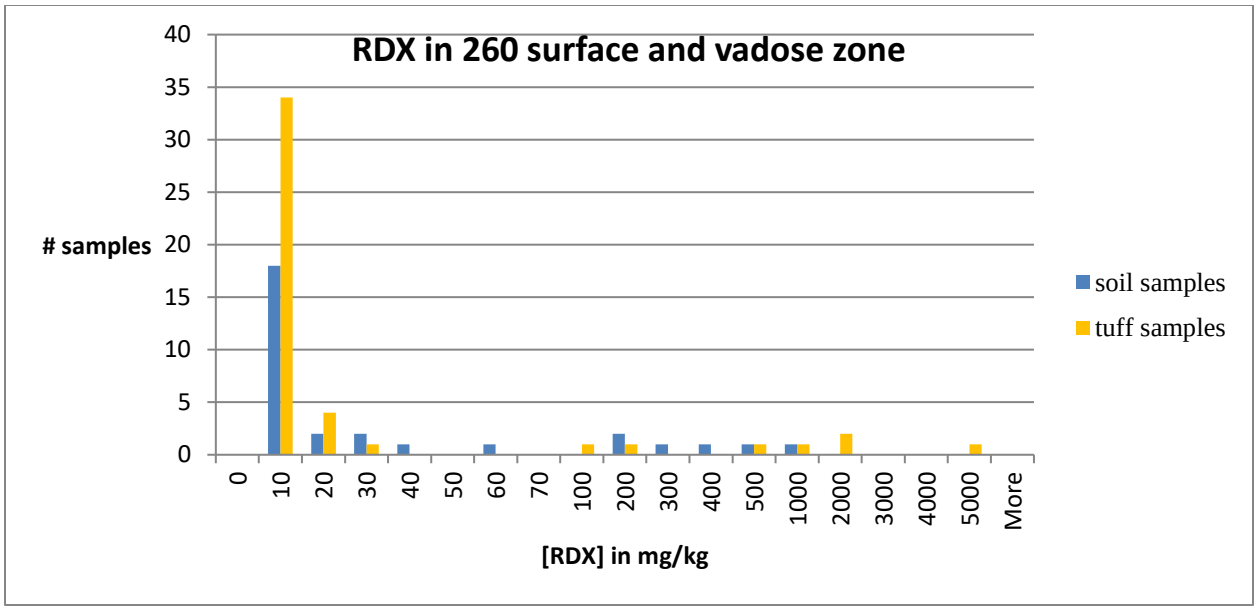

Note: Median concentration for soil is 3 mg/kg and for tuff is 1.74 mg/kg. Minimum concentration for soil is 2 mg/kg and for tuff is 0.475 mg/kg. Maximum concentration for soil is 15.5 mg/kg and for tuff is 13 mg/kg.

Figure 2 Histogram showing RDX concentrations in solid phase samples

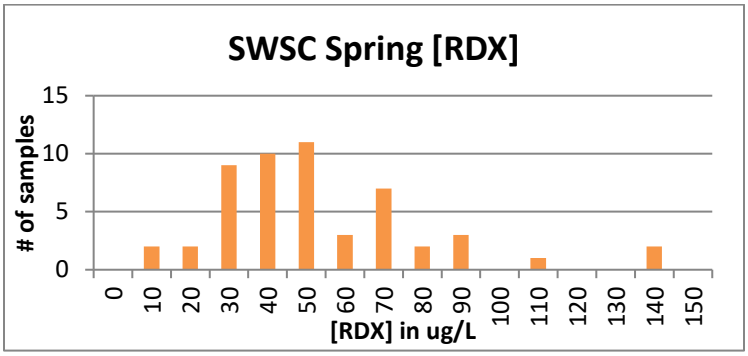

Note: Median concentration for SWSC Spring is 44 µg/L. Minimum is 31 µg/L. Maximum is 61 µg/L.

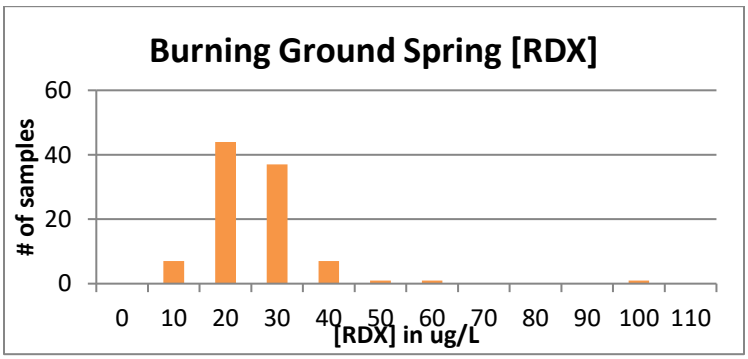

Note: Median concentration for Burning Ground Spring is 20 µg/L. Minimum is 16 µg/L. Maximum is 24 µg/L.

Figure 3 Histograms showing RDX concentrations in spring discharges

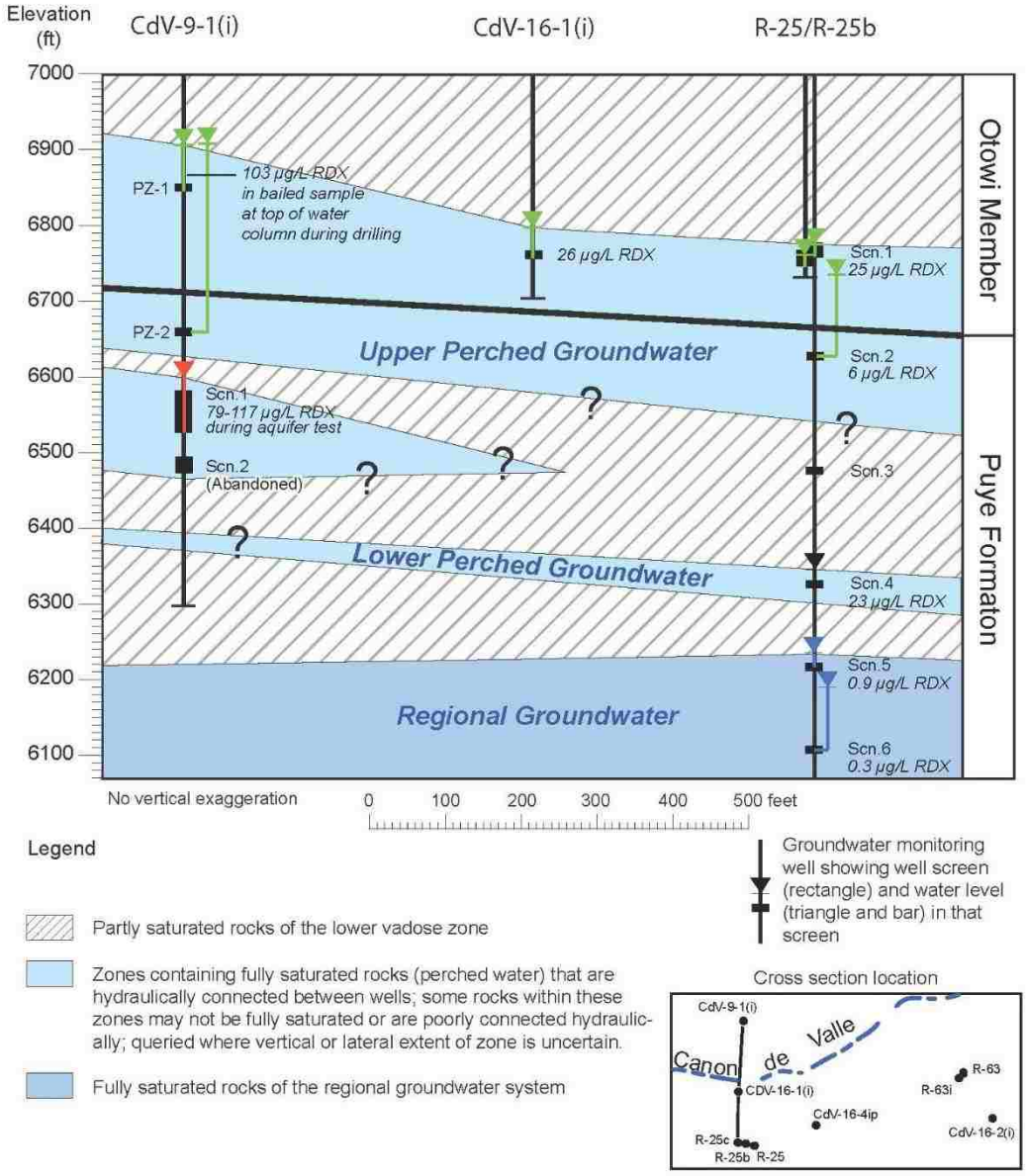

Figure 4 **North-south geologic cross-section for the lower part of the vadose zone showing geologic contacts and groundwater occurrences in wells CdV-9-1(i), CdV-16-1(i), R-25b, and R-25**

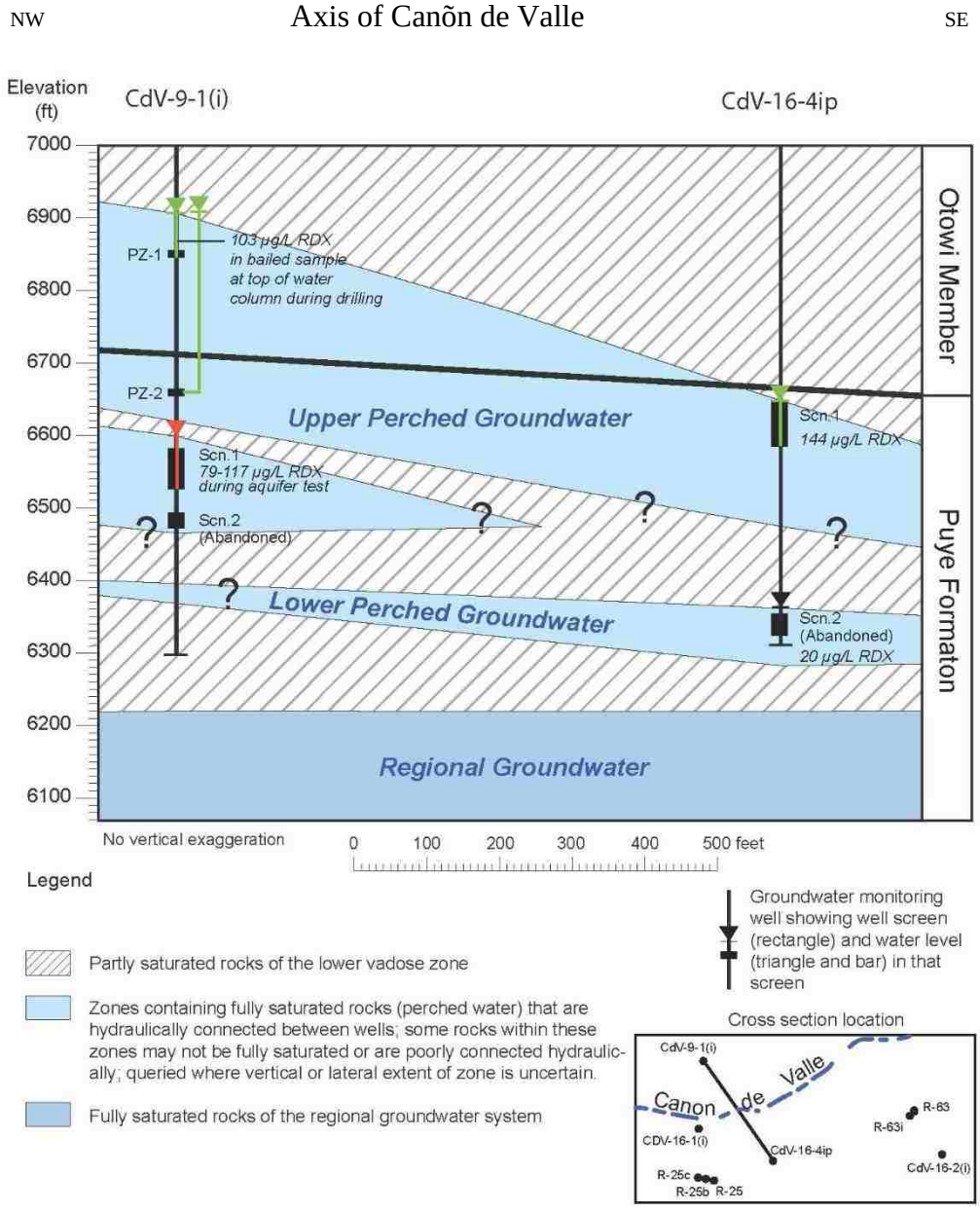

Figure 5 **Northwest-southeast geologic cross-section for the lower part of the vadose zone showing geologic contacts and groundwater occurrences in wells CdV-9-1(i) and CdV-16-4ip**

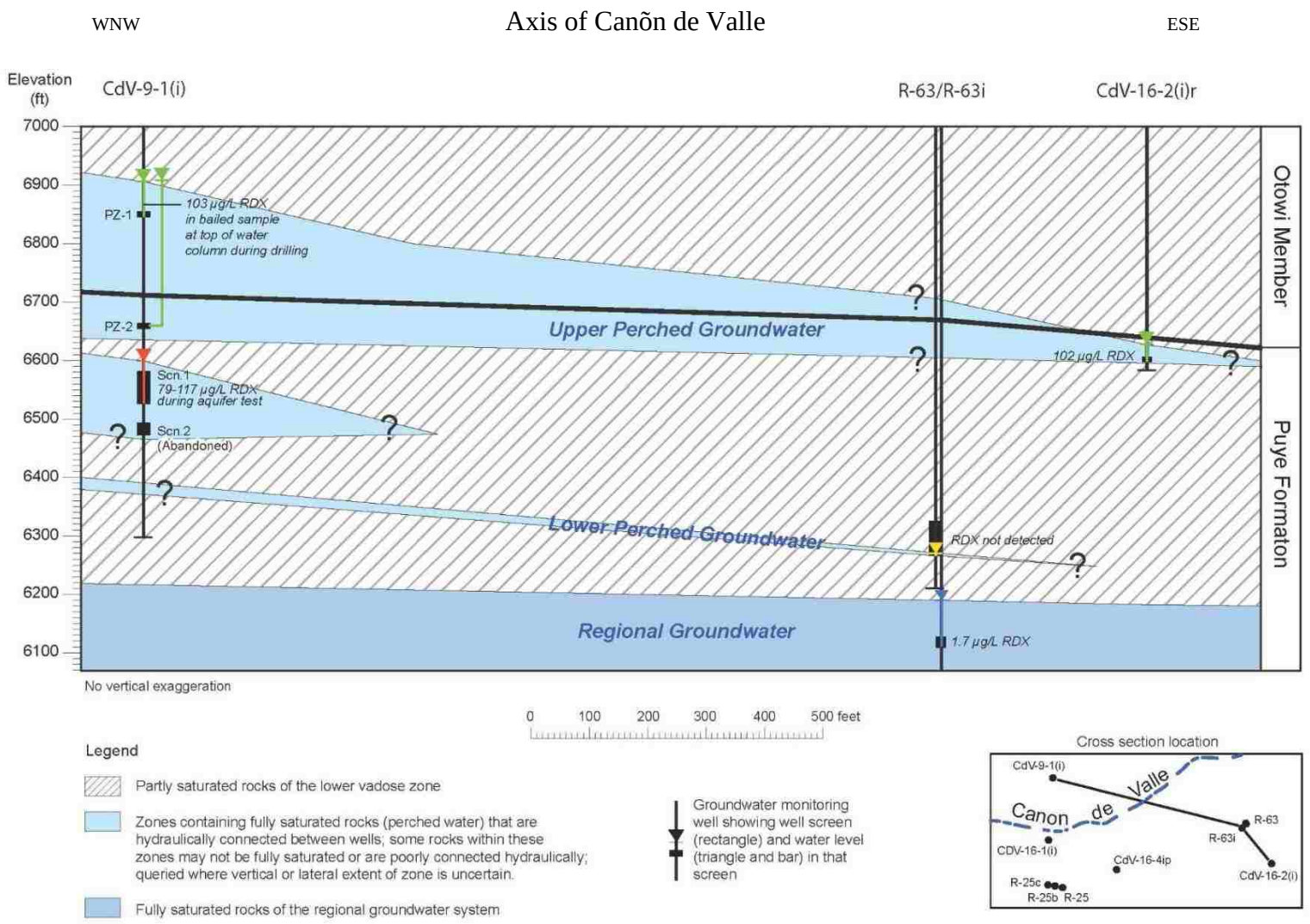

Figure 6 **West-northwest to east-southeast geologic cross-section for the lower part of the vadose zone showing contacts and groundwater occurrences in wells CdV-9-1(i), R-63i, R-63, and CdV-16-2(i)r**

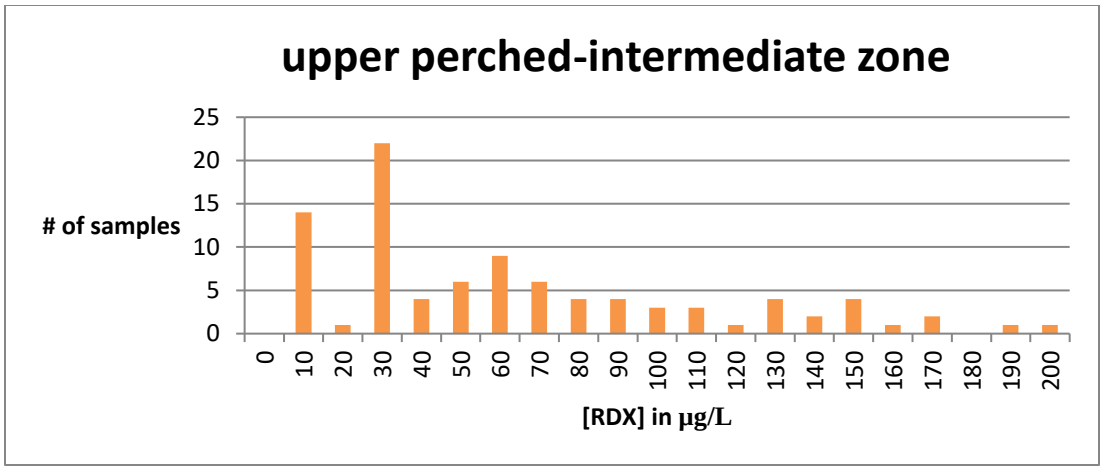

Note: Median concentration for perched-intermediate groundwater is 49.3 µg/L. Minimum concentration is 26.1 µg/L. Maximum concentration is 81.9 µg/L.

Figure 7 Histogram showing RDX concentrations in perched-intermediate groundwater

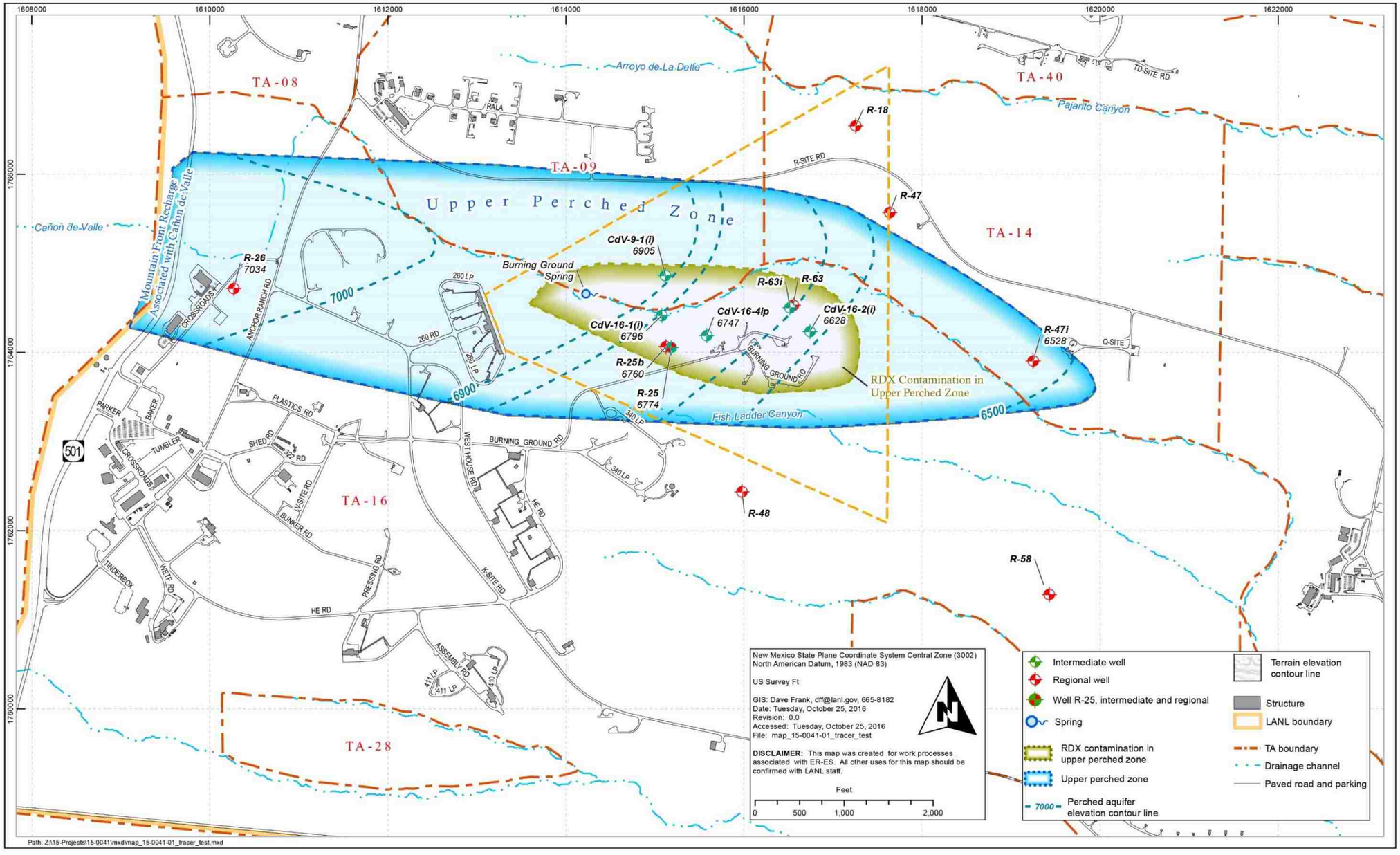

Figure 8 Contaminated groundwater areas within TA-16. The orange dashed line represents the assumed regional aquifer contaminated area. The green inner zone is the extent of RDX contamination in upper perched zone (LANL 2015, 600535).

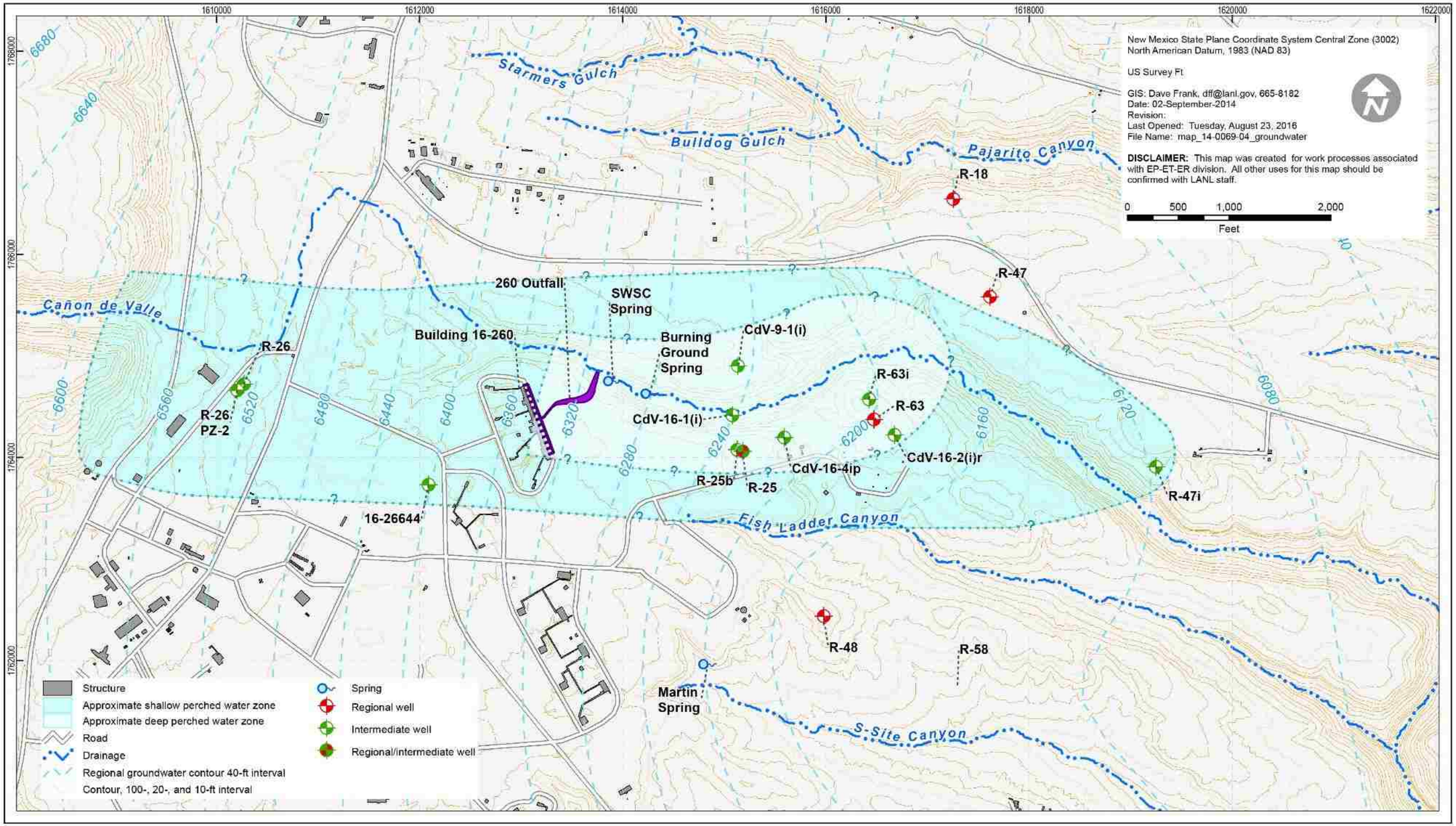

Figure 9 Approximate extent of perched-intermediate zones at TA-16

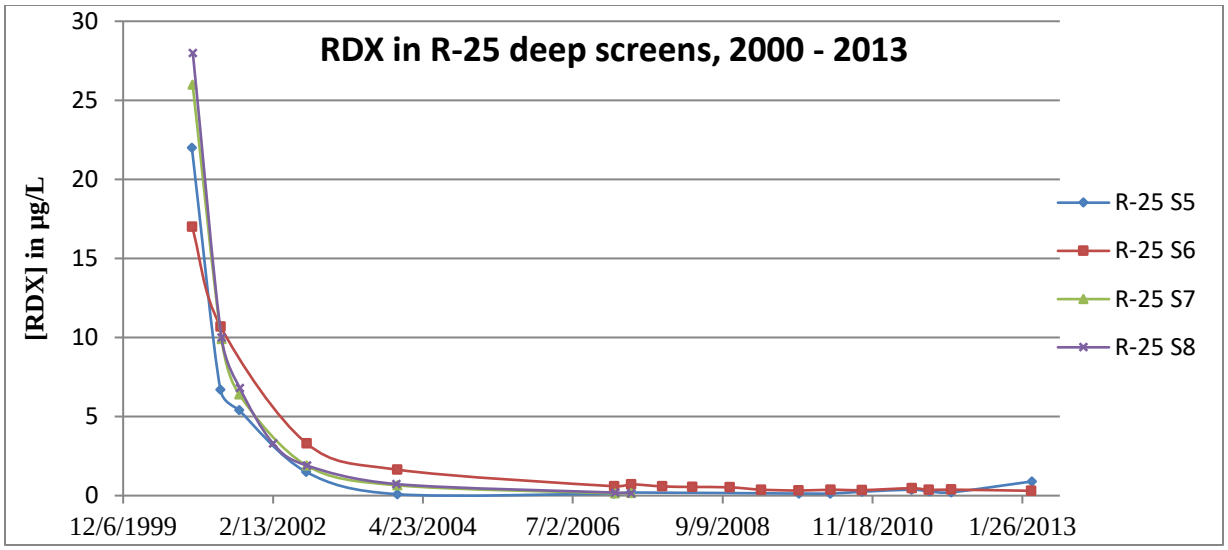

Figure 10 RDX concentrations in well R-25 screens in regional groundwater

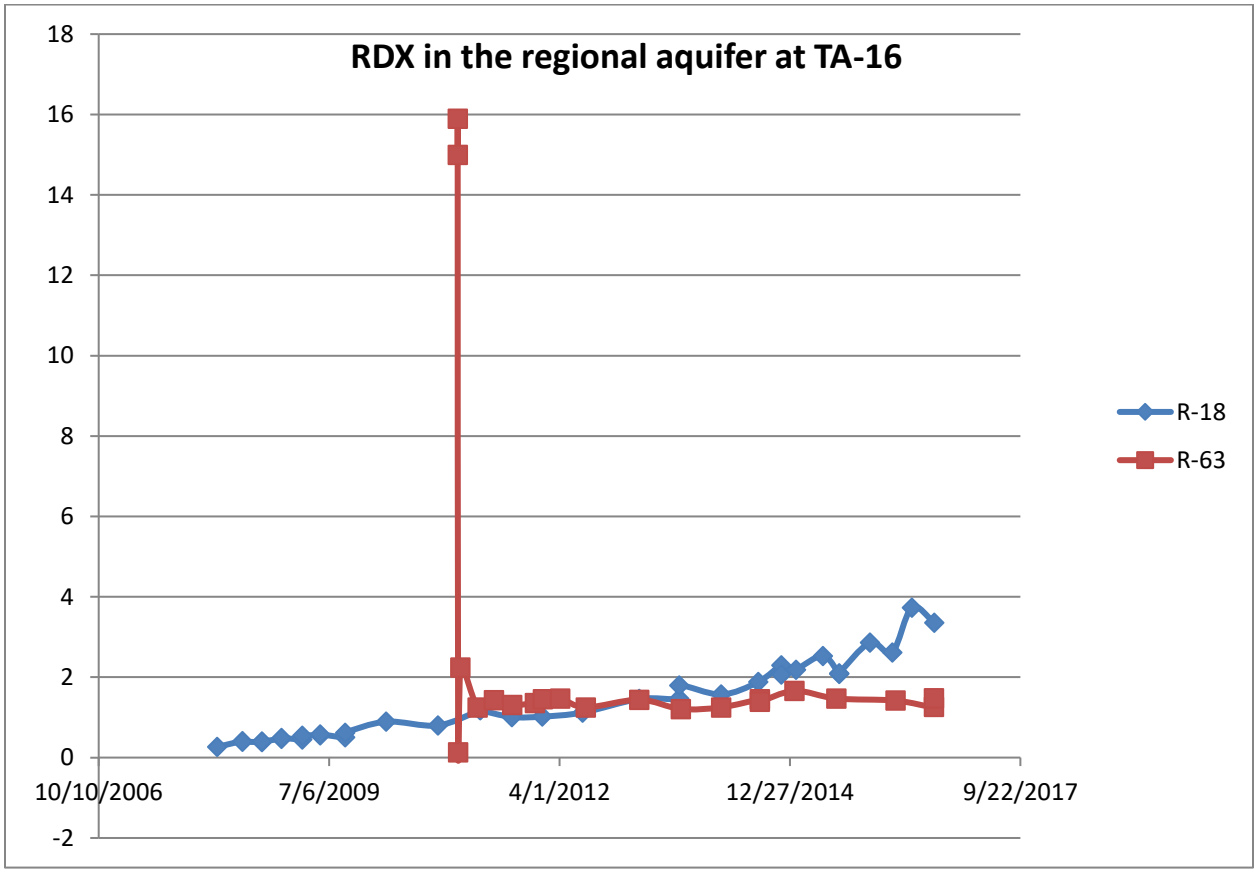

Figure 11 Regional well RDX concentrations over time

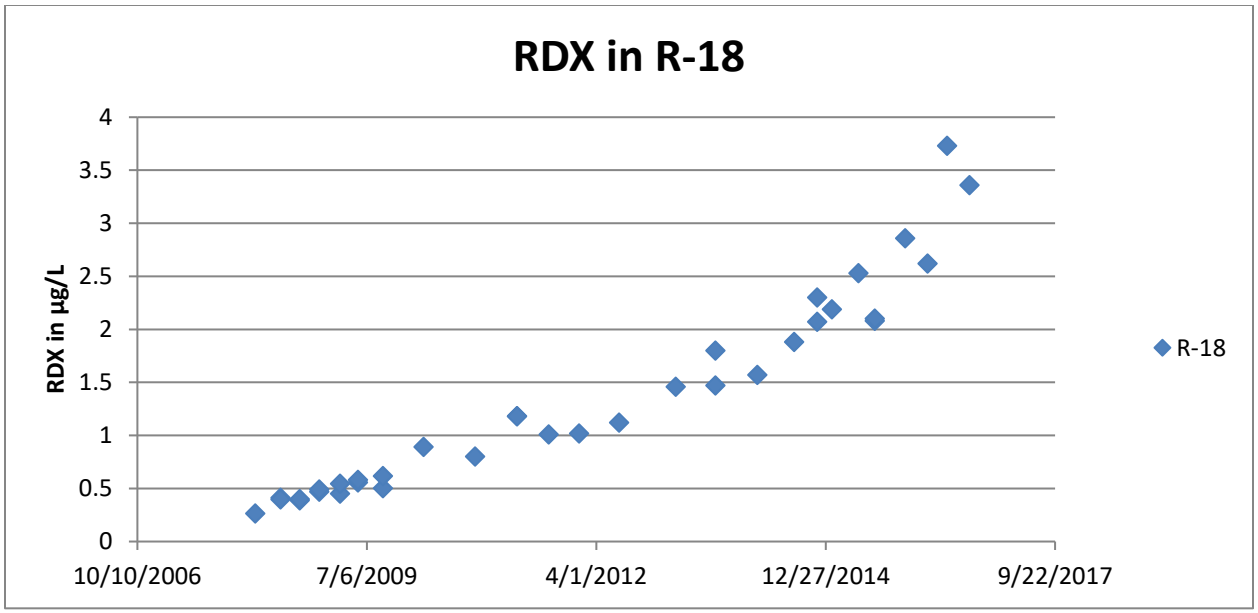

Figure 12 RDX concentrations in R-18

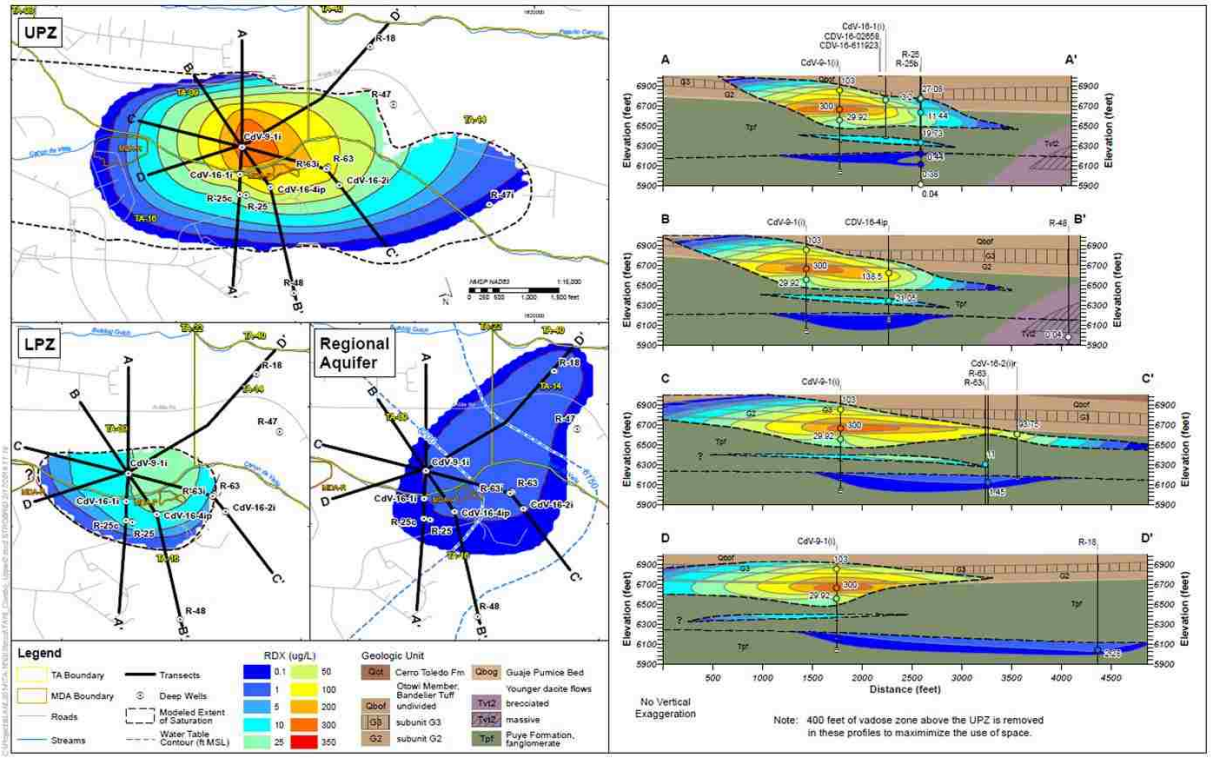

Figure 13 Example of 3-D RDX interpolation (from Weston, Inc., 2016, 601836)

Table 1
Estimated Ranges of Total RDX Inventories in Hydrologic Components, 2005

Location	Maximum Mass of RDX (kg)	Minimum Mass of RDX (kg)
260 Outfall former settling pond area, after interim measure	650	650
Vadose zone directly under 260 Outfall former settling pond area	4311	234
SWSC and Burning Ground Springs	482	3
Cañon de Valle alluvial sediments	5	5
Vadose zone under Cañon de Valle alluvial aquifer	3724	17
Intermediate to regional groundwater (228–345 m)	8109	476
Regional groundwater (392–592 m)	6053	135
Total	**23,334**	**1520**

Source: LANL 2006, 093798.

Table 2
RDX Inventory Summary for 2005 and 2016

Location	2005 Maximum (kg)	2005 Minimum (kg)	2016 Maximum (kg)	2016 Minimum (kg)	Maximum % Change	Minimum % Change
260 Outfall former settling pond area, after interim measure	650	650	644	644	−0.9%	−0.9%
Vadose zone directly under 260 Outfall former settling pond area	4311	234	940	545	−78.2%	132.9%
SWSC and Burning Ground Springs	482	3	56	33	88.4%	1000.0%
Cañon de Valle alluvial sediments	5	5	10	5	100.0%	0.0%
Vadose zone under Cañon de Valle alluvial aquifer	3724	17	64	8	−98.3%	−52.9%
Intermediate to regional groundwater (228–345 m)	8109	476	887	219	−89.1%	−54.0%
Regional groundwater (392–438 m)	6053	135	68	13	−98.9%	−90.4%
Total	**23,334**	**1520**	**2669**	**1467**	**−88.6%**	**−3.5%**

Table 3
Summary of Upper Perched-Intermediate Groundwater Well Samples

Well Screen	Number of Samples	Years Sampled	Screen depth (ft)	Most Recent RDX Detection (µg/L)
CdV-16-4ip S1	16	2010–2015	815.6–879.2	144
CdV-16-2(i)r	34	2006–2015	850–859.7	102
CdV-16-1(i)	26	2005–2014	624–634	25.5
R-25b	15	2009–2015	750–770.8	3.12
CdV-9-1(i)	1	2015	937.4–992.4	103

Notes: The median from this data set is 49.3 µg/L. The first quartile value is 26.1 µg/L, and the third quartile value is 81.9 µg/L. To calculate the maximum and minimum masses of RDX in the intermediate zone, the quartile concentrations were multiplied by the estimated maximum and minimum volumes for pore water in the zone.

Table 4
Summary of Regional Groundwater Well Samples

Well Screen	Number of Samples	Years Sampled	Screen Depth (ft)	Most Recent RDX Detection (µg/L)
R-18	46	2008–2016	1358–1381	3.36
R-63	19	2011–2016	1325–1345.3	1.66

Notes: The maximum concentration seen in R-18, 3.8 µg/L, was used to estimate maximum RDX mass in the regional zone. The median of all 54 samples, 1.21 µg/L, was used to estimate the minimum RDX mass in the regional zone.

Table 5
Comparison of 2016 Simple Geometry and Geostatistically Based Inventories

Location	Simple Geometry Minimum (kg)	Simple Geometry Maximum (kg)	Geostatistical Minimum (kg)	Geostatistical Maximum (kg)
260 Outfall former settling pond area, after interim measure	644	644	na*	na
Vadose zone under 260 Outfall former settling pond area	545	940	na	na
SWSC and Burning Ground Springs	33	56	na	na
Cañon de Valle alluvial sediments	5	10	0.16	0.16
Vadose zone under Cañon de Valle alluvial aquifer	8	64	na	na
Perched-intermediate groundwater (228–345 m)	219	887	650	1581
Regional groundwater (392–438 m)	13	68	1.8	8.5

Total	1467	2669	na	na

*na = Not available.

8.1 Spring snowmelt groundwater recharge event in Cañon de Valle

Peak channel flows in upper Cañon de Valle, associated with easternmost terminus points in the Pajarito fault zone, have been coincident with water level rise and temperature changes in certain well screens at TA-16.

The most dramatic response was in the main screen of CdV-9-1(i), where the potentiometric surface rose by about 80 feet over the course of a month, indicating a direct connection between focused recharge in the fault and intermediate zone saturation in the Puye formation. A slight temperature rise, of 0.1 degree C, followed the water level jump. A shallower well, 16-26644, recorded a water level rise of about 8 feet, beginning about 6 days before the rise at CdV-9-1(i). In that well, the rise coincided with a drop in temperature by a similar amount. Initial water temperature in 16-26644 was 11.95 C, warmer than in the deeper well by 0.6 C. After the recharge pulse, both water temperatures had moved in the direction of 11.6 C; the shallower well remained warmer and recovered its initial temperature as the level dropped. In CdV-9-1(i), the July water level remains slightly above its initial March level, and though the temperature has dropped it remains warmer.

The main screen of CdV-9-1(i) lies in a zone of saturation below the broader upper perched intermediate zone, where two piezometers are located. It is worth noting that the recharge pulse placed the potentiometric surface of water in the main screen above the lower of the two piezometers, suggesting perhaps that water around the main screen is confined to a degree. The two piezometers, which show a water level more than 220 feet higher, recorded a rise of 10 to 12 feet, coincident with the water level rise at 16-26644.

This water peaked, dropped three feet in two weeks, and has subsequently remained stable for about two months. Water temperature in the upper zone has remained consistent and did not respond to the recharge pulse as it did at CdV-9-1(i) and 16-26644, suggesting that existing formation water rose in the piezometers rather than recharge directly.

In CdV-16-1(i), water level rose by about 3.5 feet, beginning concurrently with the rise at CdV-9-1(i) piezometers, but peaking 9 days later. This well screen resides in fractured, poorly-welded tuff of the Otowi Member, which receives incoming groundwater primarily by fracture flow. The water level has dropped from its peak by little more than a foot over more than two months remaining two feet above its pre-recharge level. Like the piezometers in CdV-9-1(i), temperature has remained consistent throughout.

In wells CdV-16-2ir, CdV-16-4ip and R-63i, neither water levels nor temperatures have responded to the wetting event in a clear or obvious way.

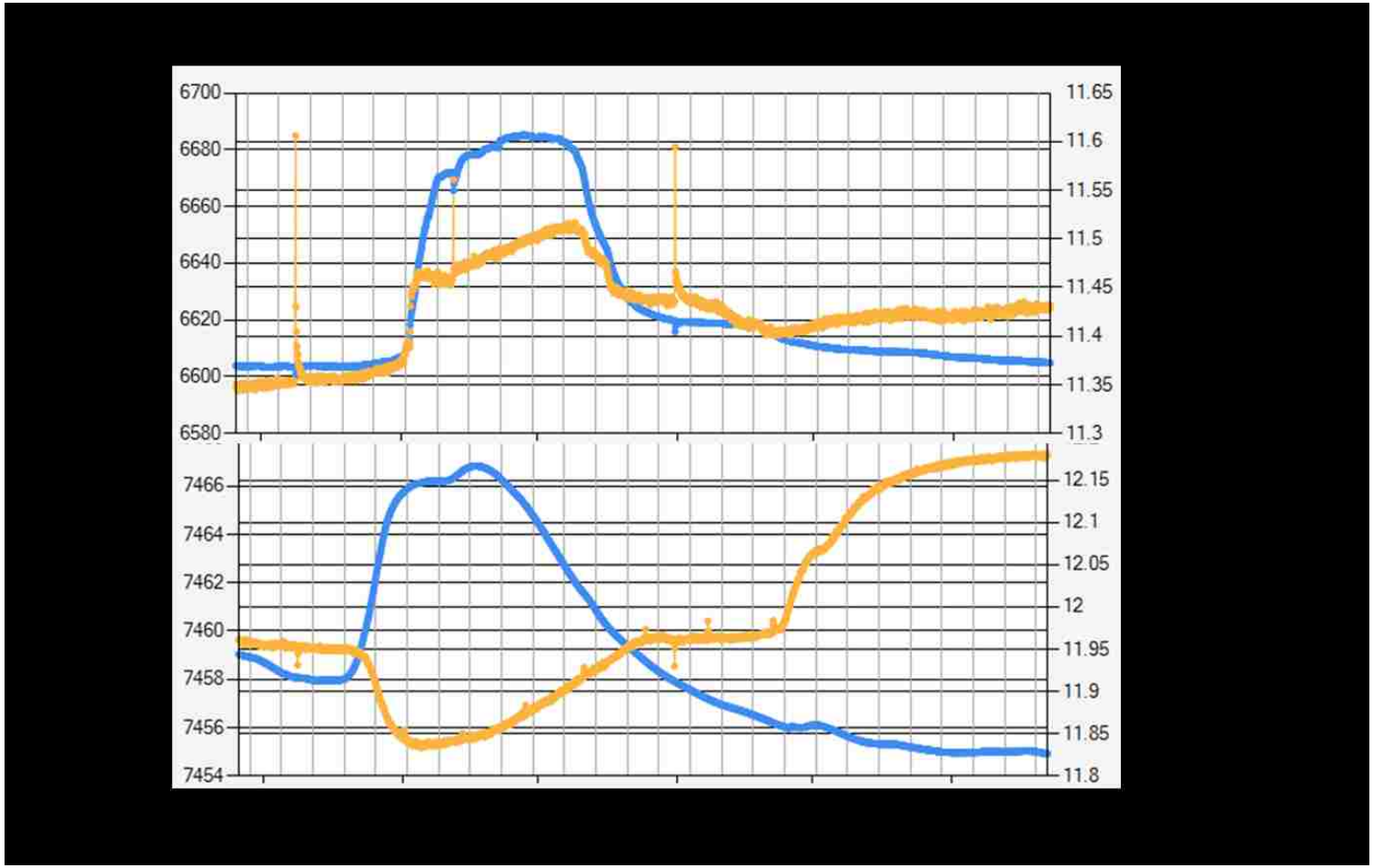
6700
6680
6660
6640
6620
6600
6580
11.65
11.6
11.55
11.5
11.45
11.4
11.35
11.3
7466
7464
7462
7460
7458
7456
7454
12.15
12.1
12.05
12
11.95
11.9
11.85
11.8